Contribution of surface flux and ocean heat transport convergence to the interannual variability of the Labrador Sea

by

© *Gaurav Madan*

A thesis submitted to the School of Graduate Studies

in partial fulfilment of the requirements for the degree of

Master of Science

Department of Physics and Physical Oceanography

Memorial University of Newfoundland

May 2020

St. John's Newfoundland

Abstract

The heat content and convergence of the heat flux transport (CHFT) in the ocean region 65^{o}W-40^{o}W, 45^{o}N-65^{o}N is studied based on in-situ observations of ocean temperature and the reanalaysis of surface flux for the period from 1993 to 2018. This region includes the Labrador Sea, the area of North Atlantic Current and Newfoundland Basin. The CHFT is computed from the equations of the tendency of heat contents for the surface (0-150 m depth), intermediate (150-2000 m depth), and deep (below 2000 m) layers and the whole ocean column. The highest interannual variability of CHFT is observed in the regions of the Newfoundland Basin and North Atlantic Current. The CHFT in the first region is influenced by the influx of sea-ice from the Northern Labrador Sea. The interannual variability of the CHFT in the second region represents the year-to-year change in the contribution of the ocean transport to the heat budget by the extension of Gulf Stream in the Subpolar North Atlantic. The CHFT in the central, eastern, northwestern, and northeastern sub-regions of the Labrador Sea were found to be highly correlated ($r>0.7$). There is a very weak correlation between the CHFT in these regions and the CHFT in the Newfoundland Basin and North Atlantic Current.

Acknowledgements

I am grateful to Dr. Entcho Demirov, my supervisor, for his patience and time, and the invaluable guidance over my two years at the Memorial University of Newfoundland. I appreciate his thoughtful approach through both the good times and difficult. This thesis certainly would not have been possible without his boundless encouragement and efforts, even during a pandemic.

I am grateful to Dr. Iakov Afanassiev, who was a part of my thesis committee, for his valuable feedback and pushing me to meet the deadlines.

Support by Christopher Stevenson through the course of this work was fantastic for all two years, particularly in times of workstation crises. I am thankful for his kind computing and system administration support, along with casual astronomical conversations.

I would also acknowledge and express my gratitude towards the Ocean Frontiers Institute for funding this project.

Finally, I would like to thank my family for their continued faith and support throughout this process.

Contents

List of Tables

List of Figures

Chapter 1

Introduction

The global ocean covers 71% of the Earth's surface and contains 97% of all the water (Costello et al., 2010). It supports 90% of the biosphere. The ocean surface fresh-water flux accounts for 85% of surface evaporation and 77% of precipitation. The sea-water has high heat capacity and plays an essential role in the planetary heat budget. Our understanding of the role of the ocean in establishing the Earth's energy and fresh water budgets has considerably improved in recent years due to the development of technologies for in-situ and remote ocean observations. In particular, it was established that the ocean meridional heat transport in the Northern Hemisphere is between 1500 and 2000 TW ($1TW = 10^{12}W$) (Johns et al. 2011). An essential part of it occurs in the Atlantic Ocean (Trenberth et al., 2001).

The Atlantic Meridional Overturning Circulation (AMOC) plays a critical role in transporting heat across latitudes. The AMOC brings the warm subtropical North Atlantic waters poleward. The cold and dense waters formed in the subarctic are transported by AMOC equatorward in the intermediate and deep layers. The AMOC

variability on time scales from interannual to centennial affects the ocean heat content and has an essential impact on the global and regional climate dynamics (Bryden et al., 2005).

One of the physical factors which drive the variability of AMOC is deep convection which occurs in several ocean regions, including the Nordic Seas, Irminger Sea and the Labrador Sea (Dickson et al., 1996; Marshall et al., 2001; Marsh et al., 2005; Cunningham and Marsh, 2010). The deep convection is driven by surface cooling when the ocean releases heat to the atmosphere, and the surface waters become denser and sink due to the convective instability (Kuhlbrodt et al. 2007). In the Labrador Sea, the deep convection reaches depths of up to 2000 m and forms the Labrador Sea Water (LSW), which feeds the lower limb of the AMOC (Marshall et al., 1998; Lazier et al., 2002; Rhein et al., 2002).

1.1 The major water masses of the North Atlantic

Based on their potential density, water masses of the North Atlantic are divided into the surface, intermediate, deep and bottom waters. The surface layer is dominated by Central Atlantic Water (CAW). The CAW is subdivided into the East North Atlantic Central Water (ENACW), West North Atlantic Central Water (WNACW). These water masses have a potential density of less than 27 kg/m^3.

The ENACW occupies the surface 500 m layer east of the Mid-Atlantic Ridge. The temperature range in the ENACW is 8.0-18.0 ^oC, and salinity varies between 35.0 to 36.7 psu. ENACW forms during the winter season and is subducted west of Iberian Peninsula. A major part of this water moves along the southern branch

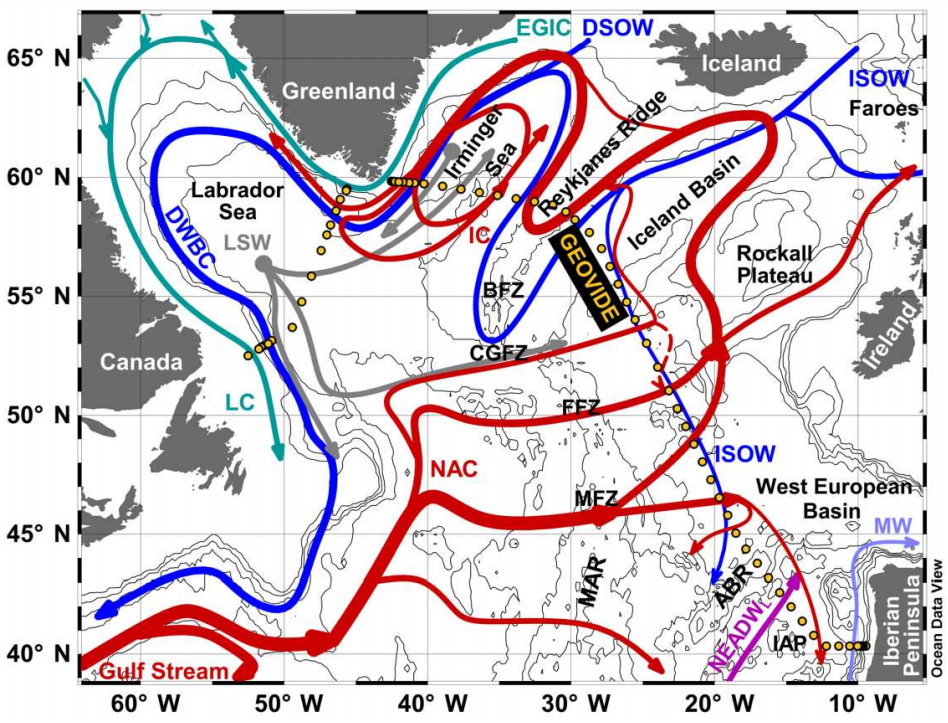

Figure 1.1: Map of the North Atlantic Subpolar Gyre from *García – Ibáñez et al.*, 2018. Continents are shaded dark grey, and ocean depth is shown in contours. Red arrows indicate warm and saline surface currents, while deep currents are shown in blue arrows. Green indicates cold and fresh surface currents. Deep convection sites are marked as grey dots, and the spread of new deep water is presented in grey arrows. LSW = Labrador Sea Water formation site; DSOW = Denmark Strait Overflow Water region; ISOW/I = Iceland Scotland Overflow Water region. NAC = North Atlantic Current; EGIC = East Greenland Irminger Current; IC = Irminger Current; LC = Labrador Current; MW = Mediterranean Water; NEADW = North East Atlantic Deep Water; CGFZ = Charlie-Gibbs Fracture Zone; BFZ = Bight Fracture Zone; MAR = Mid-Atlantic Ridge; IAP = Iberian Abyssal Plain.

of the North Atlantic Current and then southward off the coast of northwest Africa. The WNACW forms at the south flank of the Gulf Stream. It spreads in between latitudes of $\sim$10 ^oN and 40 ^oN with temperature and salinity range of 7.0-20.0 ^oC and 35.0-36.7 psu, respectively.

The water masses in the intermediate layer of the Atlantic Ocean are characterized by a potential density between 27-27.7 kg/m^3. They include Antarctic Intermediate Water (AAIW) in the south, Subarctic Intermediate Water (SAIW) and dense Mediterranean Overflow Water (MOW) in the north. The cold AAIW (temperature 2.6-11.0 ^oC and salinity 33.8-34.8 psu) originates from the surface (upper 200 m) in the region north of the Antarctic Circumpolar Current (ACC). The SAIW is a low temperature and salinity water mass ((3.0-9.0 ^oC, 34.0-35.3 psu) located north of 40 ^oN, mostly in the Western North Atlantic. MOW enters the North Atlantic at intermediate depths through the Strait of Gibraltar. It spreads to the east of the Mid-Atlantic Ridge and has relatively high temperature and salinity (T=2.6-11.0 ^oC, S=35.0-36.2 psu). AAIW spreads northward after leaving the formation area, across the equator and further north until $\sim$40 ^oN, where it meets MOW and SAIW.

The North Atlantic Deep Water (NADW) occupies the deep layer of the North Atlantic and has a potential density between 27.7 and 27.88 kg/m^3. Formed in the high latitudes of North Atlantic, cold NADW (T=1.5-4.0 ^oC, S=34.8-35.0 psu) is subdivided into upper and lower portions based on their different potential densities and origins. Upper NADW (uNADW) forms from the LSW, whereas lower NADW (lNADW) forms from Iceland-Scotland Overflow Water (ISOW) and Denmark Strait Overflow Water (DSOW).

The bottom layer of the North Atlantic is occupied by the Antarctic Bottom Water

(AABW) with a potential density of greater than 27.88 kg/m^3. AABW is a mixed product of Weddell Sea Bottom (WSBW) and Circumpolar Deep Water (CDW) in the South Atlantic Ocean and has a relatively cold temperature of -0.9-1.7 ^oC and low salinity in the range of 34.6-34.7 *psu*.

1.2 The water masses and circulation of the Subpolar North Atlantic Ocean

The warm and salty subtropical North Atlantic waters enter the upper layer of the North Atlantic Subpolar Ocean along the multiple branches of the North Atlantic Current - NAC (Figure 1.1). The NAC flows into the eastern part of the subpolar gyre in the Bay of Biscay, the Rockall Trough, the Iceland Basin, and the Irminger Sea. A portion of the NAC flows then into the Norwegian Sea, while its remaining part recirculates in the subpolar gyre. The Western Boundary Current (WBC) exports dense and cold intermediate and deep waters equatorward. These two means of transport, the NAC and the WBC determine the upper and lower branches of the AMOC in the Subpolar North Atlantic (SPNA). The circulation of the SPNA is characterized by a largescale cyclonic system of boundary currents and interior recirculations (Figure 1.1).

The surface Atlantic waters which enter the SPNA along the NAC are gradually modified as they spread through the Subpolar Gyre. The surface cooling and vertical mixing in the SPNA transforms them into the Subpolar Mode Waters (SPMW). The SPMW is a near-surface thick layer of waters with nearly uniform properties

(temperature, salinity, density). It is a reservoir of heat that is slowly released back to the atmosphere in the Subpolar Gyre. In observations, the SPMW is identified by the minimum in the vertical distribution of isopycnic potential vorticity (IPV). For small Rossby numbers, $\zeta << f$, where ζ is the relative vorticity, and f is the planetary vorticity, the IPV is determined as

$$IPV = \frac{f}{\rho}\frac{\partial \rho}{\partial z}$$

In the absence of turbulent mixing, IPV is conserved along the isopycnal surfaces. The minimum IPV corresponds to high vertical homogeneity of the water mass and acts as a tracer for SPMW.

The SPMW is not a separate water mass. Still, it is an indicator for waters formed by surface cooling and contributes to other water masses like the Central Water, Irminger Water in the Labrador Sea, Atlantic Water in the Nordic Seas, etc. The SPMWs enter the SPNA along the Rockall Trough branch and the Iceland Basin branch (Central Iceland Basin branch and Subarctic Front) of the North Atlantic Current (NAC). In the Irminger Sea, where mixing can reach up to 800-1300 m, a remnant of the SPMW forms the Irminger Water (IW). The IW enters the Labrador Sea around the southern tip of Greenland.

The Irminger Current (IC) on the west flank of the Reykjanes Ridge is mainly recirculating the East Reykjanes Ridge Current (ERRC) that turns north after crossing the Ridge. The IC is also fed in part by a minor northern branch of the NAC. The surface transport in the west Irminger Sea is dominated by the East Greenland Current (EGC). It flows parallel to the offshore Irminger Current. The two currents are commonly referred to as the East Greenland/Irminger Current (EGIC). The EGIC

follows the bathymetry around Cape Farewell and becomes the West Greenland Current (WGC), in the Labrador Sea (Figure 1.1). In the Northern Labrador Sea, one branch of the WGC propagates north and enters Baffin Bay. The remaining part of the WGC joins the Labrador Current along the west coast of the Labrador Sea.

The densest and coldest water mass of the Subpolar North Atlantic is the Denmark Strait Overflow Water (DSOW), which flows between Greenland and Iceland through the Denmark Strait over the sill down into the deep ocean on the western side of the Ridge. Likewise, Iceland Scotland Overflow Water (ISOW) flows through the southern gap between Iceland and Scotland. This water mass mixes with other water masses forming the so-called North-East Atlantic Deep Water (NEADW). It ultimately merges with the DSOW to form the Deep Western Boundary Current, which transports these dense water masses in the Subpolar Gyre.

1.3 Circulation, mixing and water mass formation in the Labrador Sea

The Labrador Sea, which is the coldest and freshest region of the subpolar North Atlantic, serves as one of the final junction points for the upper modified surface Atlantic Waters. The presence of these waters creates significant horizontal and vertical temperature and salinity contrasts in the surface layer of the Labrador Sea. Two boundary currents dominate the advective transport in the upper layer of the Labrador Sea: Labrador and West Greenland Currents.

The WGC brings northward waters from the Irminger Sea, entering the Labrador

Sea along the southern tip of Greenland. The relatively shallow surface layer in the WGC transports cold and fresh modified waters of the Eastern Greenland Current and sea-ice. The waters of the WGC below the thermocline consist of warm and salty Irminger Water (IW). The subsurface part of the boundary WGC transporting the IW in the Labrador Sea is often referred to as the Irminger Current. The IW plays an essential role in the restratification of the ocean after the winter convection.

The Labrador Current is a cold, boundary current along the coasts of Labrador and Newfoundland. It has two branches: the inshore branch and the offshore branch. The inshore branch flows over the shelf of the west Labrador Sea. The offshore branch is a barotropic current over the shelf-slope. The Labrador current has a number of recirculations, especially evident at mid-depths.

The intermediate layer of the SPNA is filled with Labrador Sea Water (LSW), formed mainly in the Labrador Sea and in the Irminger Sea (see Figure 1.1). The Labrador Sea Water (LSW) is also often referred to as the Upper North Atlantic Deep Water (UNADW). The strong vertical density gradient in the thermocline inhibits the vertical exchange between the surface ocean layer and the abyss, insulating deep water from surface variations. The ocean dynamics in the central part of the basin facilitate intense and deep-reaching convection and mixing.

The events of deep convection are subdivided into three stages (Marshall and Schott 1999). The first stage is called preconditioning when the gyre-scale cyclonic circulation and an accompanying (upward) doming of isopycnals are intensified. This process brings the abyssal weakly stratified water closer to the surface. During late autumn and early winter, the thin layer of strongly stratified water is eroded by the increasingly large buoyancy loss to the atmosphere. This exposes the weakly stratified

water underneath to the cold atmosphere.

During the second stage called violent mixing, the large heat and buoyancy loss to the atmosphere drives deep convection in localized 'plumes' about 1 km in diameter. In these plumes, vertical velocities reach up to 10 cm/s (Marshall and Schott 1999). The vertical motion homogenizes water characteristics in the plumes. During and after the violent mixing, rapid lateral mixing with the surrounding water creates an area of dense water, known as a 'chimney' or a 'mixed patch' (Marshall and Schott 1999). A rim current develops around this chimney, between the dense water in the convected area and the stratified, lighter water surrounding which is in geostrophic balance with the lateral density gradient. This rim current then becomes baroclinically unstable and generates small eddies, called Convective Eddies (CE). The typical scale of the CE is the order of the internal Rossby radius of deformation. The mesoscale eddies forming on the rim current, their motion and decay induce horizontal mixing of the waters in the convection site and restratifies the ocean.

The boundary current acts as a major source of buoyancy for the replenishment of the dense water mass in the convected area (LabSeaGroup 1998; Lilly et al. 2003). The buoyant water is brought into the interior by lateral eddy-induced fluxes, while the dense convected water is exported out of the Labrador Sea in the boundary current. A major role in this lateral exchange is played by the Irminger Eddies, which form along the WGC in the northeastern part of the Labrador Sea. They have a typical radius of about 50 km and a lifetime between several months to years. Their vertical structure is determined by the presence of a cold and fresh surface layer and a core of warm and salty Irminger Waters between 50 and 1000 m depth. The Irmniger Rings motion has a predominantly negative zonal velocity component towards the

central part of the basin.

The depth of convection varies on interannual to decadal time scales (Lazier, 1980). The corresponding changes in the thickness, temperature and salinity of the LSW have large-scale consequences as the newly formed LSW spreads and affects the potential vorticity structure of the subtropical Atlantic gyre. The major driver of interannual to decadal variations in the LSW rate of formation is the long-term variability in the winter air-sea fluxes.

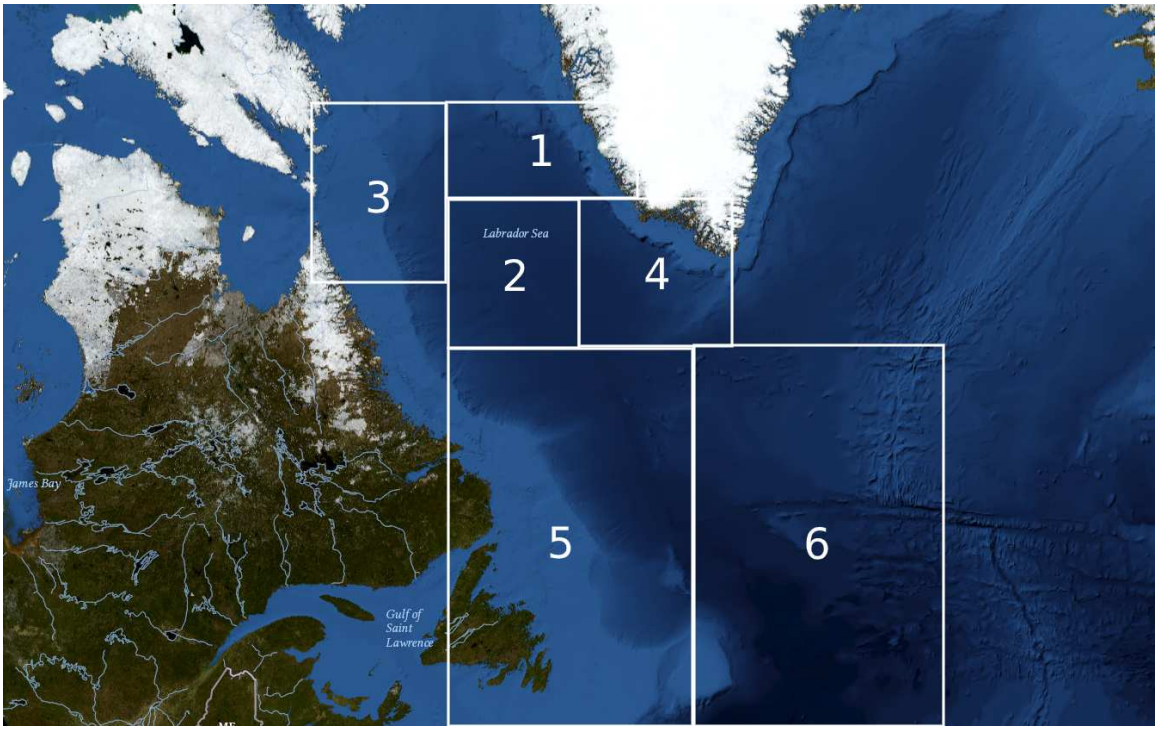

Figure 1.2: Map of the Subpolar North Atlantic Ocean showing the main bathymetric features and the geographical location of the studied subregions (1-6) (Bathymetry from USGS Global Baselayer).

The AMOC makes the climate of the Arctic and subarctic milder and brings

cold polar deep and intermediate waters equatorward. The currents of the Labrador Sea (see Figure 1.1) are an important component of the AMOC. The dynamics of these currents and their contribution to the AMOC are related in a complex way to processes like air-sea interaction, deep convection, mesoscale and sub-mesoscale eddies, LSW formation, and LSW spreading. In addition to this, sea-ice covers large areas of the Labrador Sea, affecting its heat budget. Many of these processes are the focus of intense studies and observations but are still not fully understood. The focus of this thesis is to understand the advective heat transport in an integral way. The heat budget is averaged over six regions in the Labrador Sea (see Figure 1.2).

Region 1 is over the Northeast Labrador Sea. This is the region where the Irminger Rings form and propagate towards the Central Labrador Sea, triggering an essential later eddy-induced heat transport. Region 2 in the Central Labrador Sea is the area of intense deep convection and deep water formation. Region 3 in the Northwest Labrador Sea is the area influenced by the inflow from the Hudson Channel and the Baffin Bay and where the Labrador Current forms. Region 4 in the East Labrador Sea, where the inflow from the Irminger Sea enters into the Labrador Sea. Region 5 in the South Labrador Sea is over the Newfoundland Basin, where the Deep Western Boundary Current exports the LSW out of the Labrador Sea. Region 6 is over the North Atlantic Current.

1.4 The ocean heat transport

The advection-diffusion equation for the ocean temperature (T) is:

$$\frac{\partial T}{\partial t} + \nabla_h \mathbf{u_h} T + \frac{\partial wT}{\partial z} = \nabla \cdot \nu_h \nabla T + \frac{\partial}{\partial z} \nu_v \frac{\partial T}{\partial z} \tag{1.1}$$

The second and third terms in the left define the horizontal and vertical advection correspondingly. The terms on the right are the horizontal turbulent diffusion with coefficients ν_h in horizontal and ν_v in vertical. The tendency of ocean heat content of the layer between depths of D_1 and D_2 is

$$\frac{\partial H}{\partial t} = -\rho_o c_p \left[\nabla \cdot \int_{D_1}^{D_2} (\mathbf{u_h} T - \nu_h \nabla T) dz \right] + \rho_o c_p \left[wT - \nu_v \frac{\partial T}{\partial z} \right]_{D_1}^{D_2} \tag{1.2}$$

where

$$H = \int_{D_1}^{D_2} \rho_o c_p T dz \tag{1.3}$$

is the heat content of the ocean layer. The equation of heat budget (equation 1.2) represents a balance between the tendency of heat content in the left-hand side and the convergence of ocean heat transport, both advective and turbulent, in the right-hand side. When the upper boundary of the layer is at the surface ($D_2 = 0$), one needs to account for the surface fluxes and the presence of sea-ice. The boundary condition at the surface is

$$\nu_v \frac{\partial T}{\partial z} = Q_{sw} - \Sigma_w$$

and $w = 0$ at $z = 0$ where Q_{sw} is the net atmospheric heat flux into the ocean, and Σ_w is the heat exchange with the surface sea-ice. Using the boundary condition we can write:

$$\frac{\partial H}{\partial t} - Q_{sw} + \Sigma_w = -\rho_o c_p \left[\nabla \cdot \int_{D_1}^{D_2} (\mathbf{u_h} T - \nu_h \nabla T) dz \right] - \rho_o c_p \left[wT - \nu_v \frac{\partial T}{\partial z} \right]_{D_1}^{D_2} \tag{1.4}$$

Therefore, the heat budget of the water column is a balance between the tendency of heat content and surface heat flux input and the convergence of ocean heat transport. The surface of the Labrador Sea is partly covered by sea-ice. The contribution of sea-ice to the ocean heat content is determined by latent heat Σ_w due to ice formation and melt. To account for this contribution, we consider the equation of the tendency of enthalpy of sea-ice at the ocean surface:

$$\frac{\partial H_i}{\partial t} - Q_{si} - \Sigma_w = -\rho c[\nabla \cdot \mathbf{u} H_i - q_i] \tag{1.5}$$

where

$$H_i = \int_{-h}^{0} \alpha \rho c T_i dz \tag{1.6}$$

is the ocean enthalpy, Q_{si} is the surface heat flux to the sea-ice, α is the percentage of area covered by sea-ice, ρ is the ice density, h is sea-ice thickness, and T_i is the ice temperature. Here q_i represent all transports of enthalpy, which are not advective.

The sum of the two equations (1.4 and 1.5) provides the equation for the total heat budget, including the contributions of both the ocean and sea-ice:

$$\frac{\partial H}{\partial t} - Q_s = -\rho_o c_p \left[\nabla \cdot \int_{D_1}^{D_2} (\mathbf{u_h} T - \nu_h \nabla T) dz\right] - \rho_o c_p \left[wT - \nu_v \frac{\partial T}{\partial z}\right]_{D_1}^{D_2} - \left[\rho c(\nabla \cdot \mathbf{u} H_i - q_i) - \frac{\partial H_i}{\partial t}\right] \tag{1.7}$$

where $Q_s = Q_{si} + Q_{sw}$ is the net surface heat flux into the ocean.

The right-hand side of the equation accounts for the contributions to the convergence of heat transport: (a) horizontal advective and diffusive heat flux in the ocean (first term); (b) vertical advective and diffusive heat flux at the bottom of the ocean

layer (second term); and (c) surface heat flux due to the lateral transport of sea-ice, ice formation and ice melt (third term). The second term vanishes when D_2 is the bottom depth. In the following, we will refer to the right-hand side as the convergence of heat transport.

The tendency of the sea-ice heat enthalpy is normally difficult to find from observations. The estimation of H_i requires observations for the ice concentration (α), the vertical profile of temperature in the ice T_i, and ice-thickness h. At the same time, the observations for ice-concentration suggest that the studied ocean region is ice-free for two to three months every year. The sea-ice enthalpy also varies seasonally and becomes zero (since $\alpha = 0$) in the summer. Therefore, the annual average of the tendency of sea-ice enthalpy calculated as an average between months of August of each year :

$$\left\langle \frac{\partial H_i}{\partial t} \right\rangle = \frac{1}{T_{year}} \int_{T_{year}} \frac{\partial H_i}{\partial t} dt = 0 \tag{1.8}$$

The focus of this study is on the interannual variability of the heat flux convergence. It is estimated based on ocean observations which are low-pass filtered, and the seasonal cycle is removed. To show the impact of low-pass filtering on the ice characteristics, here we use synthetic data of sea-ice concentration (α). α is one of the ice parameters in equation (1.6) which along with the ice-thickness (h_i) and ice temperature T_i determines the time variability of the enthalpy. The synthetic (α_s) monthly mean data of sea-ice concentration each year are simulated as:

$$\alpha_s(i) = \alpha(i)(1 + A(year) \times 0.25), \quad i = 1, 12 \tag{1.9}$$

where the $\alpha(i)$ is the observed climatological monthly mean sea-ice concentration

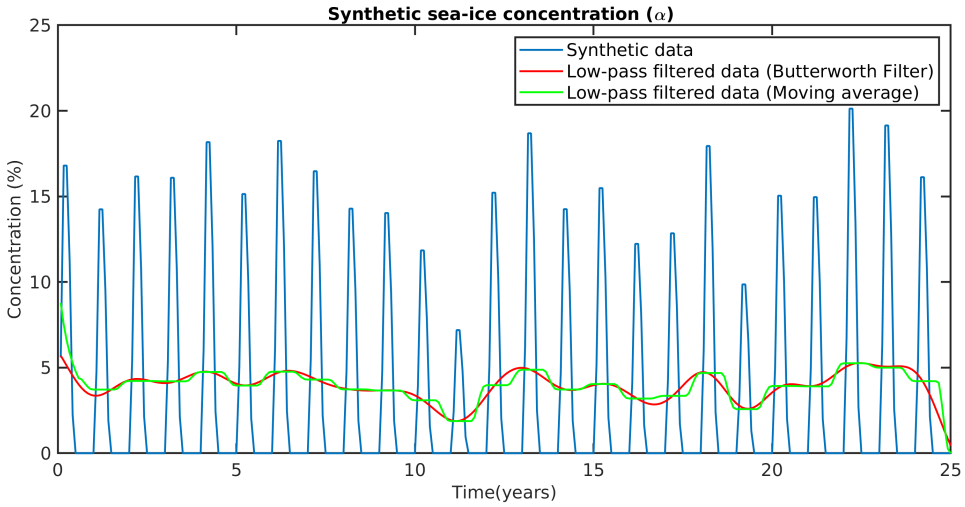

Figure 1.3: Time series for (a) Synthetic (blue), (b) Low-pass filtered (Butterworth) (red), and (c) Low-pass filtered (Moving Average) (green) sea-ice conentration data.

data for each of the regions, $0.25 \times A(year)$ determines the interannual changes in seasonal amplitude in sea-ice variations. Here A(t) is defined as a normally distributed random number with zero mean and standard deviation equal to one. The synthetic and filtered data of sea-ice concentration are shown on Figure 1.3

The time difference of the synthetic data

$$\Delta\alpha_s = \alpha_s(n+1) - \alpha_s(n) \tag{1.10}$$

have strong seasonal cycle with positive tendency of sea-ice concentration in the fall and early winter and negative in the spring. This seasonal cycle is removed from the filtered estimates of the the tendency of ice concentration (Figure 1.4).

The filtered sea-ice concentration time difference still changes at interannual time scales. These changes result from the variations in the amplitude of the seasonal cycle of sea-ice concentration. While equation (1.8) ensures the annual mean value

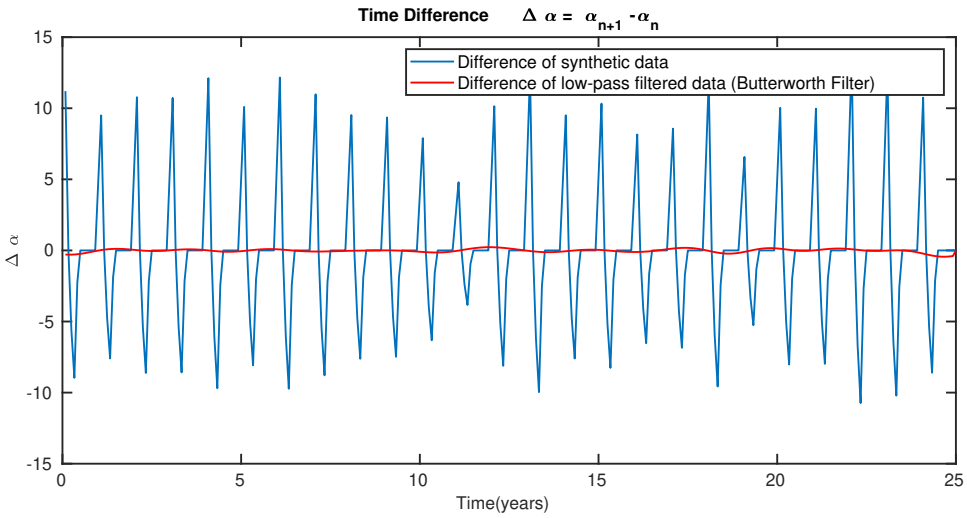

Figure 1.4: Time difference of the (a) Synthetic and (b) Low-pass filtered (Butterworth) data shown in blue and red, respectively.

of the $\partial H_i/\partial t$ to be zero if calculated between the summer months of two subsequent years, the contribution of this term will be not exactly equal to zero in the heat budget calculated by using low-pass filtered temperatures. We used 2500 randomly generated realizations of 25 years series of $\Delta\alpha_s$ computed by using (1.9) and (1.10). In region three the standard deviation of the filtered $\Delta\alpha_s = 0.92 \pm 0.16$. The unfiltered values of $\Delta\alpha_s = 14.8 \pm 0.7$. In region five the values of $\Delta\alpha_s$ estimated form filtered and unfiltered data are 0.15 ± 0.02 and 4.4 ± 0.2 correspondingly. The uncertainty is defined as two standard deviations.

The contribution of the tendency of ice enthalpy in the surface heat budget is reduced by the low-pass filtering by about 93-97%. Therefore in our analysis, we assume that the third term in the right-hand side of equation(1.7), the contribution of the tendency of ice enthalpy, is negligibly small and this term is dominated by the convergence of the horizontal transport of sea-ice. This result means that the impact

of the sea-ice to the ocean heat budget is through the ice-ocean heat exchange and export of heat by the ice exported from areas with freezing surface during the winter towards the ice-free areas. The final expression to the convergence of heat transport due to ocean and sea-ice advection and diffusion used in this study is:

$$-\rho_o c_p \left[\nabla \cdot \int_{D_1}^{D_2} (\mathbf{u_h} T - \nu_h \nabla T) dz\right] - \rho_o c_p \left[wT - \nu_v \frac{\partial T}{\partial z}\right]_{D_1}^{D_2} - \rho c [\nabla \cdot \mathbf{u} H_i - q_i] - \frac{\partial (H_i)}{\partial t} = \frac{\partial H}{\partial t} - Q_s \tag{1.11}$$

1.5 Objectives of the study

The general objective of the thesis is to understand the contribution of the ocean transport of heat to the interannual variability of the Labrador Sea.

The specific objectives are:

1. To assess the surface heat fluxes and variations in the ocean heat content for the period 1993-2018.

2. To assess the convergence of ocean transport of heat and its interannual variability.

3. To explore the physical causes of long-term variability in the heat content in the Labrador Sea.

Chapter 2

Data and Methods

This chapter describes the data and methodology used in this thesis to study changes in the heat budget of the subpolar North Atlantic region. Surface fluxes of heat and lateral transports drive the variations in the heat budget of the basin. These driving factors have strong seasonal variability causing intense surface cooling, sea-ice formation, and intensified wind-driven circulation in the winter, and restratification of deep convection area, ice melting, and spreading of the LSW in spring and summer. This study focuses on the interannual variability of the heat content and heat flux convergence and addresses the question about the possible long-term changes in the heat budget of the Labrador Sea and their links to the surface forcing and ocean dynamics in the region. All data sets used in the study are low-pass filtered with a frequency cutoff of $f_c = 1 year^{-1}$.

2.1 Region of the study

This study is focused on heat transport in the Northwestern Subpolar North Atlantic and especially the basin of the Labrador Sea and surrounding area. The study area is (see Section 1.5) further divided into six regions.

2.1.1 Northeast Labrador Sea

Northeastern Labrador Sea (subregion 1) is the area of Western Greenland Current (WGC) and the formation of Irminger rings. The WGC is a part of the cyclonic circulation of North Atlantic Oceans subpolar gyre and flows along the west coast of Greenland and northward in the eastern Labrador Sea. It is composed of two components —a cold and fresh stream on the shelf with a warmer and saltier Irminger Water offshore. Originated in the East Greenland/Irminger Current system, it transports as much as 15 Sv of sea water that is a mix of between 0.5 and 2.0 Sv of cold and fresh water on the shelf with the Irminger Water subducting under the low-salinity polar water. Some of this inflow recirculates back to the Irminger Sea, and about 11.7 Sv enters the Labrador Sea. The mean temperature in subregion 1 in Figure 2.1 shows strong seasonality in the surface layer temperatures. Frequent cold temperatures can be seen in the year 1994-1998 for most the year and warming between 2000 and 2015 when high temperatures penetrate deep as 500 m. The seasonal cycle is relatively small below 2000 m.

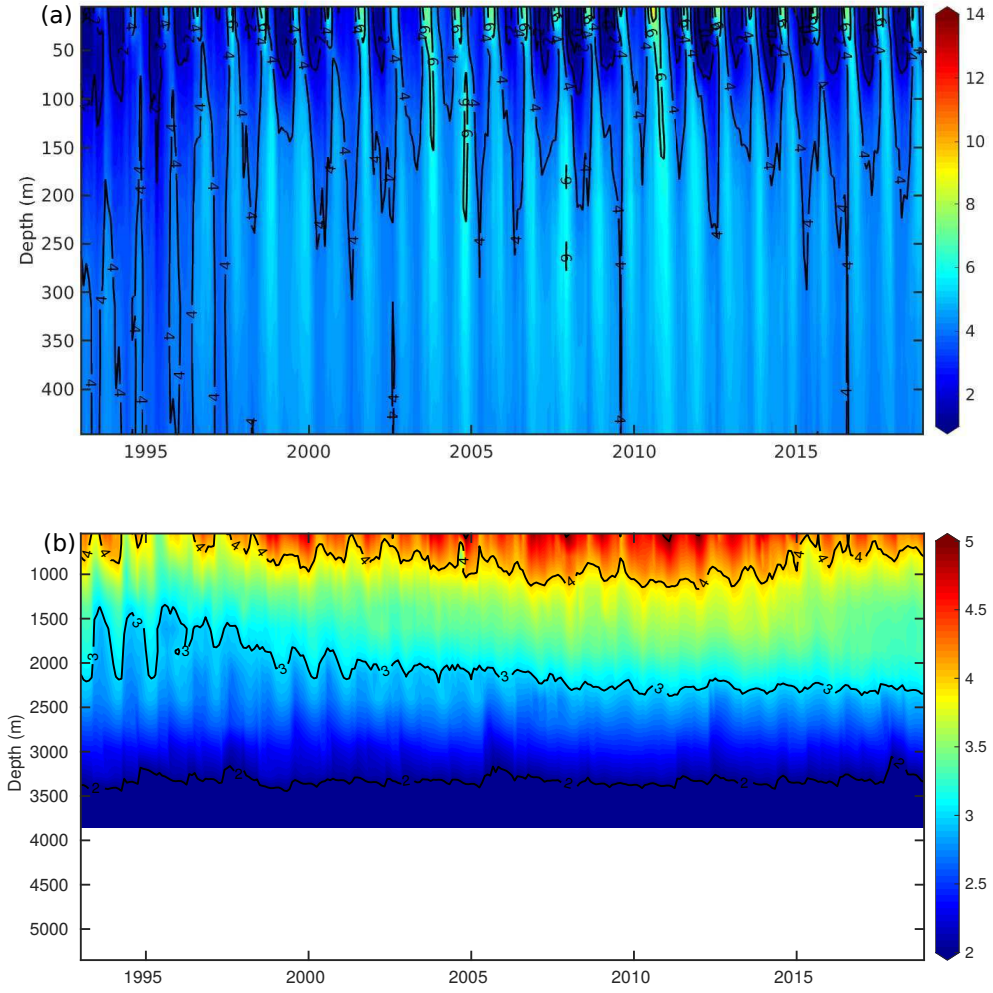

Figure 2.1: Time progression of Potential temperature (^oC) from (a) surface to 500 m and (b) 500 m to bottom in the Northeastern Labrador Sea for the period 1993-2018.

2.1.2 Central Labrador Sea

In the winter season, the waters in subregion two in the Central Labrador Sea (see Figure 1.2) are relatively cold, fresh, and well homogenized down to depths of about 500 m (Figure 2.2). The Upper North Atlantic Deep Water (uNADW), which is also called the Labrador Sea Water (LSW) is formed here by deep convection in the

late winter (February/March). The wintertime buoyancy loss increases the density of the surface water in the Central Labrador Sea sufficiently to overcome the density stratification in the upper 1000-2000 m. LSW is an important component of the AMOC.

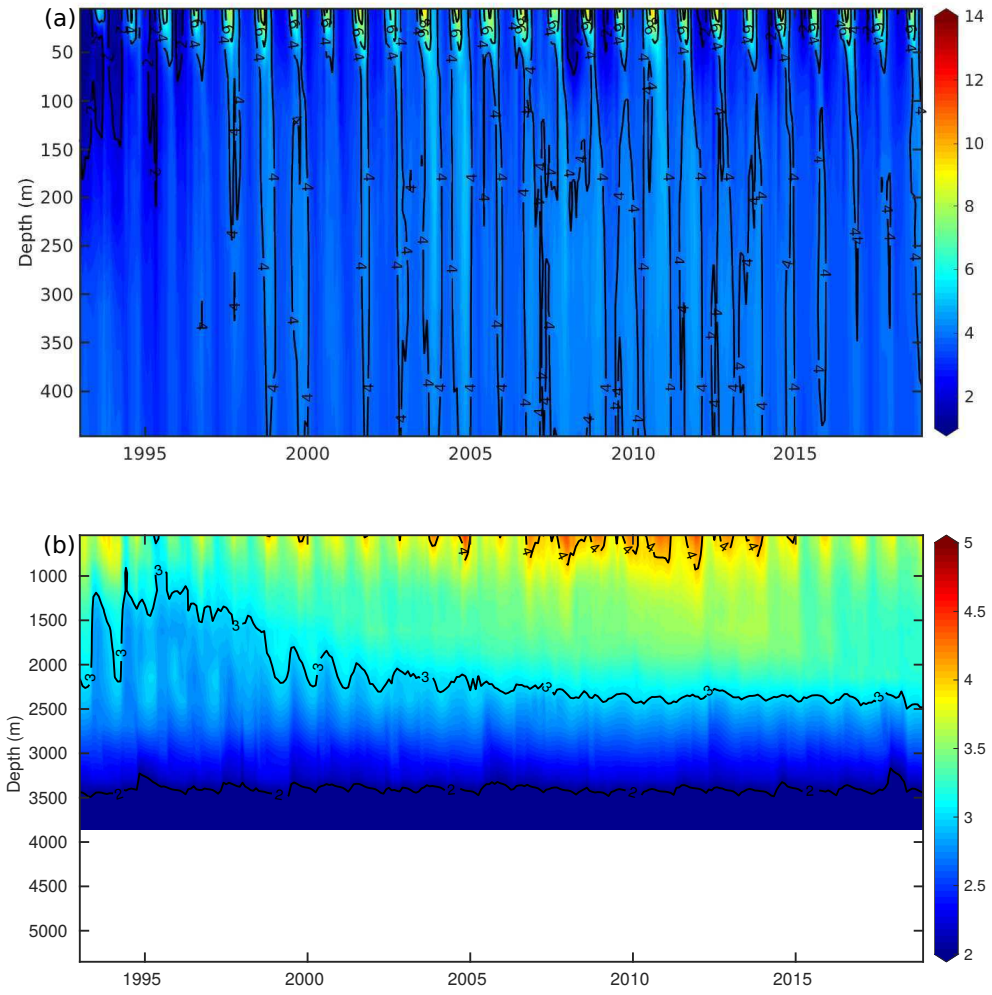

Figure 2.2: Time progression of Potential temperature (^oC) from (a) surface to 500 m and (b) 500 m to bottom in the Central Labrador Sea for the period 1993-2018.

The rate of formation of new LSW in subregion two (see Figure 2.2) was relatively low in the period 1995-1997. These were relatively warm years with weak deep convection. The cold LSW observed at depths 500-2000 m in 1995-1997 was an old water mass formed in the period from 1985 to 1994 (Yashayaev, 2007). The gradual increase of the temperature in this old LSW was caused by the relatively weak winter cooling in these years. The formation of new LSW intensified again since 2014, but this new LSW had temperature relatively higher than in 1995-1997.

2.1.3 Northwest Labrador Sea

The subregion three is an area influenced by water inflow from the Hudson Strait and the Davis Strait. The surface waters in this region are fresh and cold. The flow in the Hudson Strait is bidirectional along the two coasts, i.e., into the Hudson Bay along the Baffin Island and out of the bay along with the Northern Quebec (LeBlond1981;Drinkwater 1988). The outflow combines with that from the Davis Strait and with the retroflexion of the West Greenland Current (subregion one) to eventually form the Labrador Current (Mertz et al., 1993; Loderet al., 1998).

In Figure 2.3, the seasonal cycle is visible in the surface layer with extremely cold temperature in winter (low as -3 ^oC) through the spring and mild temperatures in the summer going only high 4-5 ^oC. While the surface temperature warms in the summer, the intermediate layer between 50 m and 100 m remains cold during most of the period of study. A warming trend in the first ten years of the 2000s similar to the one in subregion two is seen at depths between 500 m and 2000 m.

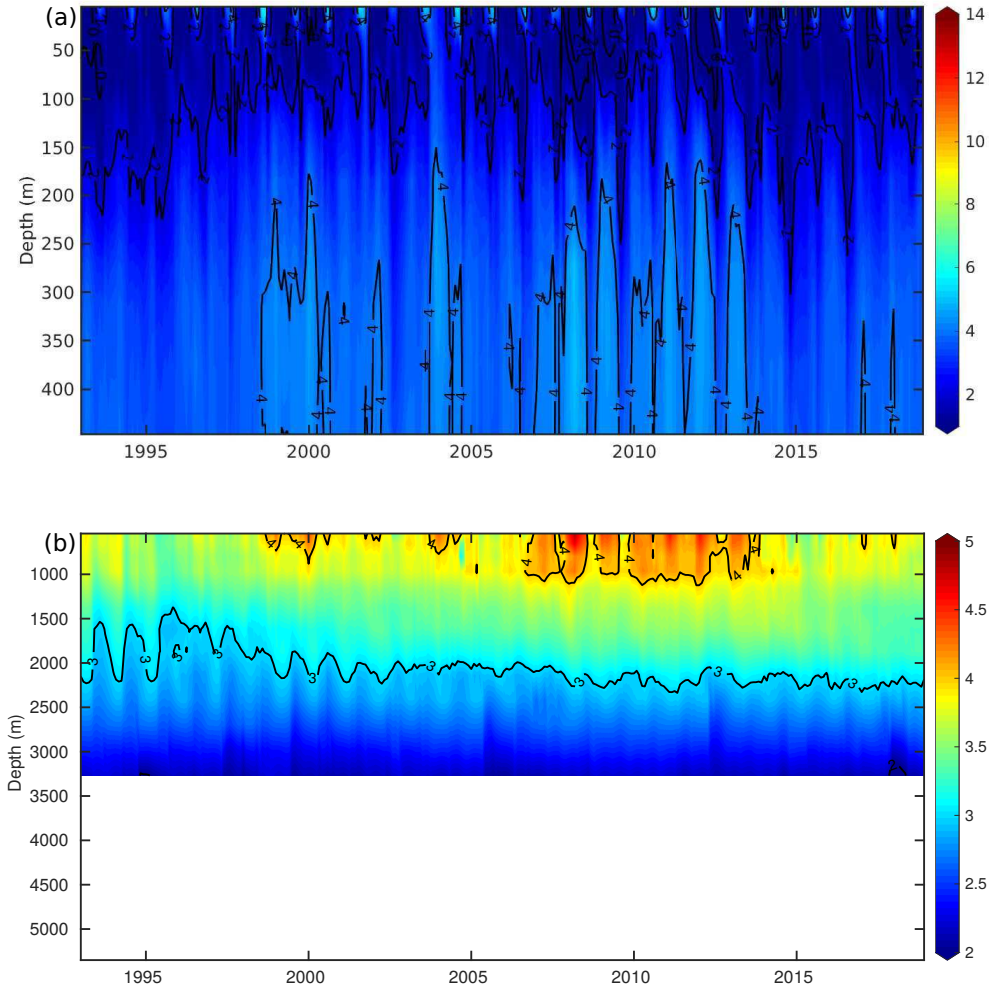

Figure 2.3: Time progression of Potential temperature (^oC) from (a) surface to 500 m and (b) 500 m to bottom in the Northwest Labrador Sea for the period 1993-2018.

2.1.4 Eastern Labrador Sea

The subregion 4 in the Eastern Labrador Sea is the region of inflow from the Irminger Sea into shallow, cyclonic, boundary circulation of the Labrador Sea, that flows southward above the Newfoundland shelf and upper slope. There is a seasonal variation in flow in this region that flows along Western Greenland Current along Greenland

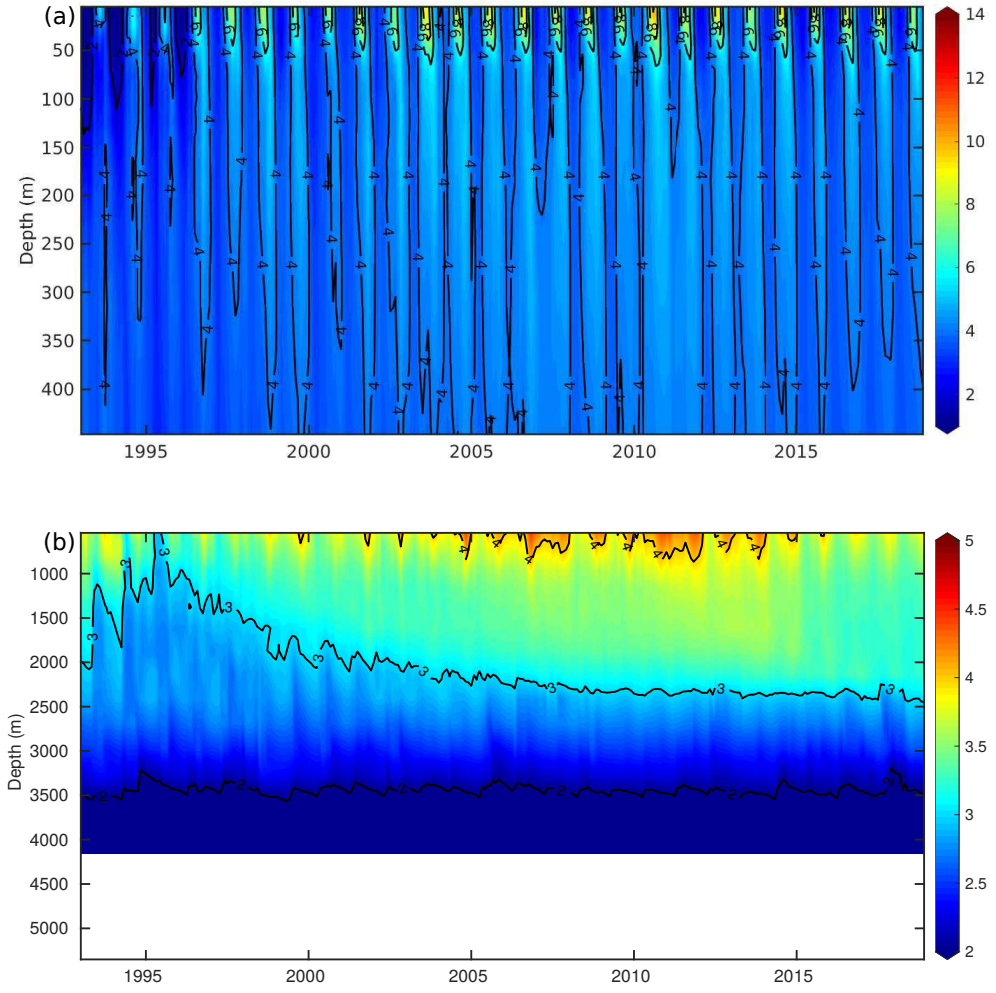

Figure 2.4: Time progression of Potential temperature (^oC) from (a) surface to 500 m and (b) 500 m to bottom in the East Labrador Sea for the period 1993-2018.

shelf with maximum transport in October and minimum in MarchApril owing to the variations in freshwater influx from Baffin Bay (Lazier and Wright, 1993). The modified Irminger Water travels around the basin below the surface cold water along the upper Labrador slope. Offshore of the main boundary currents, a series of cyclonic recirculation cells form a weak anticyclonic flow in the interior (Lavender et al. 2000). The deep circulation that consists of the deep western boundary current along the 3000 m isobath carries NADW, NEADW and the denser DSOW through the cyclonic flow in the basin.

A much stronger seasonal cycle is seen (Figure 2.4) in the whole of upper 500 m. The transports in the subpolar gyre are stronger in January-February and weaker in July (Greatbach and Goulding, 1989) that brings warm ISW as the heat source and keeps the Labrador Sea ice-free in the winter (Lilly et al. 1999; Lazier 1973). As a result, we do not see cold temperature in the surface layer in the winter when compared to subregions one, two and three. We observe a warming trend from 1996 to 2010 in the intermediate layer that stabilized in the following years. No interannual trend is observed in the deeper layer below 2000 m.

2.1.5 Southern Labrador Sea

The Labrador Current transports the cold and relatively fresh waters in the surface layer and modified warmer and saline Irminger Water at intermediate depths. The current, when it approaches Newfoundland shelf, appears as two branches, the inshore Labrador Current and a stronger offshore branch. Newfoundland shelf is dominated by the inshore Labrador Current that flows near the coast, which eventually merges

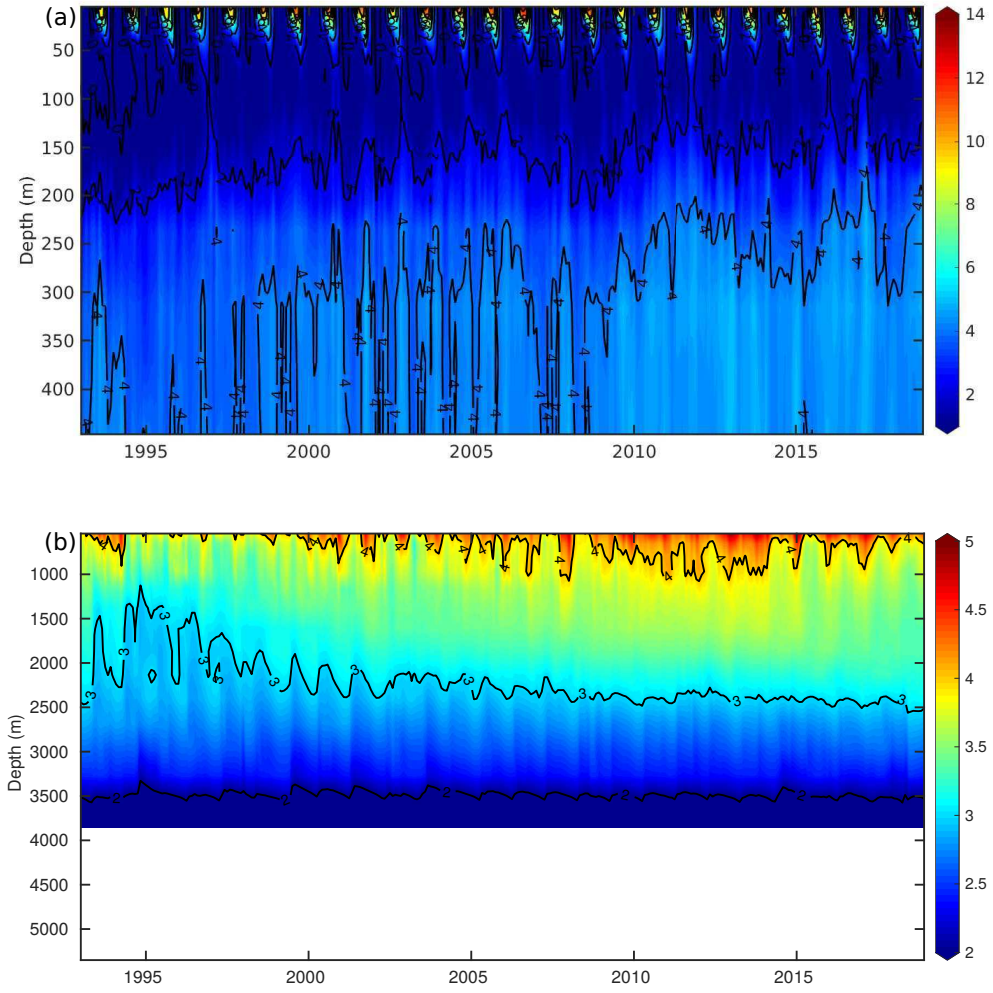

Figure 2.5: Time progression of Potential temperature (^oC) from (a) surface to 500 m and (b) 500 m to bottom in the South Labrador Sea for the period 1993-2018.

with offshore Labrador Current to the south of 48 ^oN. The current undergoes significant changes due to a deep-rugged section in the north and shallower Newfoundland Shelf around Grand Banks.

The surface layer of the Southern Labrador Sea (Figure 2.5) shows strong seasonality with variation as much as 12 ^oC. Warm temperatures are observed during

summer, and the coldest temperature is observed during winter and spring because of the presence of seasonal sea ice. This shows that atmospheric conditions and surface fluxes could have a strong role.

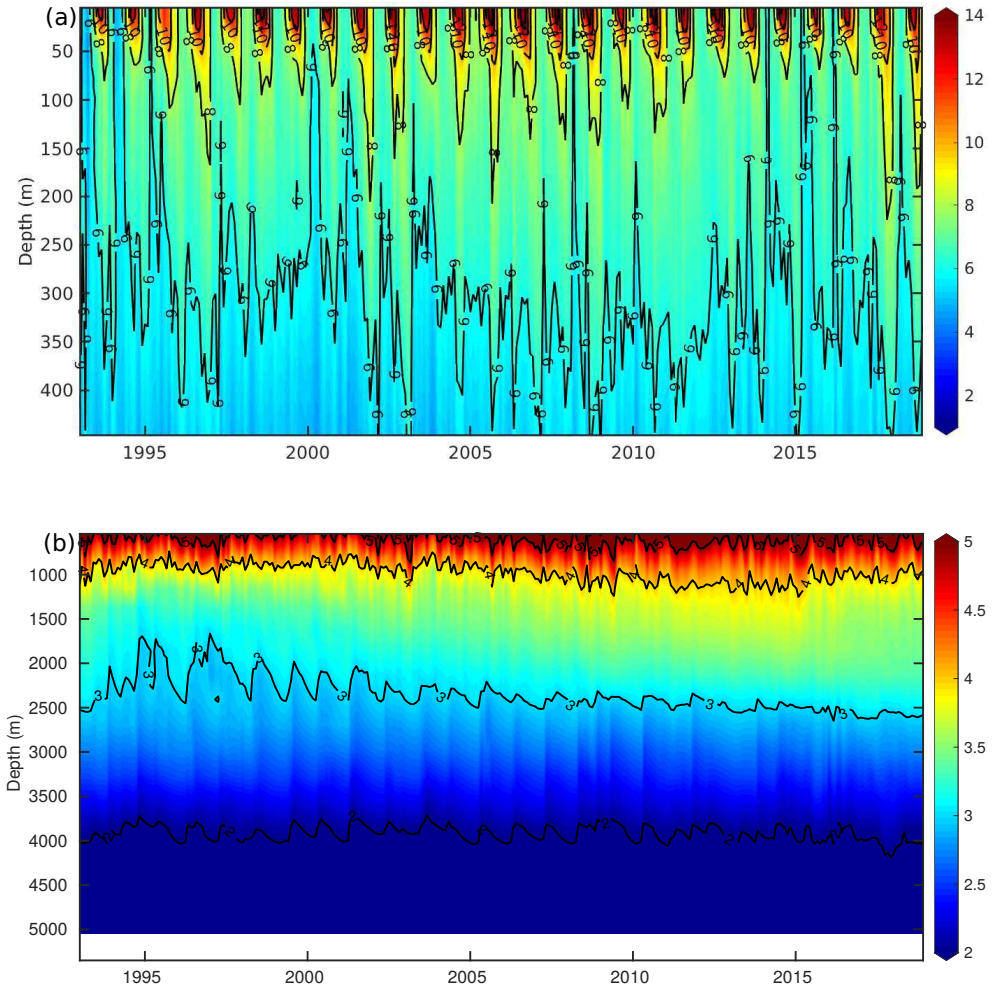

Figure 2.6: Time progression of Potential temperature (^oC) from (a) surface to 500 m and (b) 500 m to bottom in the North Atlantic Current region for the period 1993-2018.

2.1.6 The North Atlantic Current

Subregion six is the region where the North Atlantic Current (NAC) enters the Subpolar North Atlantic. The NAC is an extension of the Gulf stream which brings warm and salty subtropical waters. The NAC forms three distinct branches at Grand Banks (see in Figure 1.1) which play essential role for the transport of these waters into the subarctic and Arctic. The subregion six (Figure 2.6) exhibits strong seasonality in the surface layer. Most of the seasonal changes take place in the top 400 m or so with surface temperature varying from 14 ^oC to 7-8 ^oC. The seasonal cycle is relatively in intermediate and deep layers.

2.2 The Data

2.2.1 MetOffice EN4 Argo Data

EN4 is a quality controlled database of global subsurface ocean temperature and salinity profiles, objective analyzed and gridded onto a regular grid. The methodology of EN4 is developed by two European Union projects: ENACT (Enhanced Ocean Data Assimilation and Climate Prediction) and ENSEMBLES. It is based on a collection of observations for ocean temperature and salinity profiles (see Figure 2.7) over the period 1900 to the present. A series of quality control checks are applied to these observations. A method for objective analysis is used to obtained grided data of temperature and salinity profiles and estimate the data uncertainty.

EN4 is available in NetCDF format from the Met Office Hadley Centre observations website, http://www.metoffice.gov.uk/hadobs.

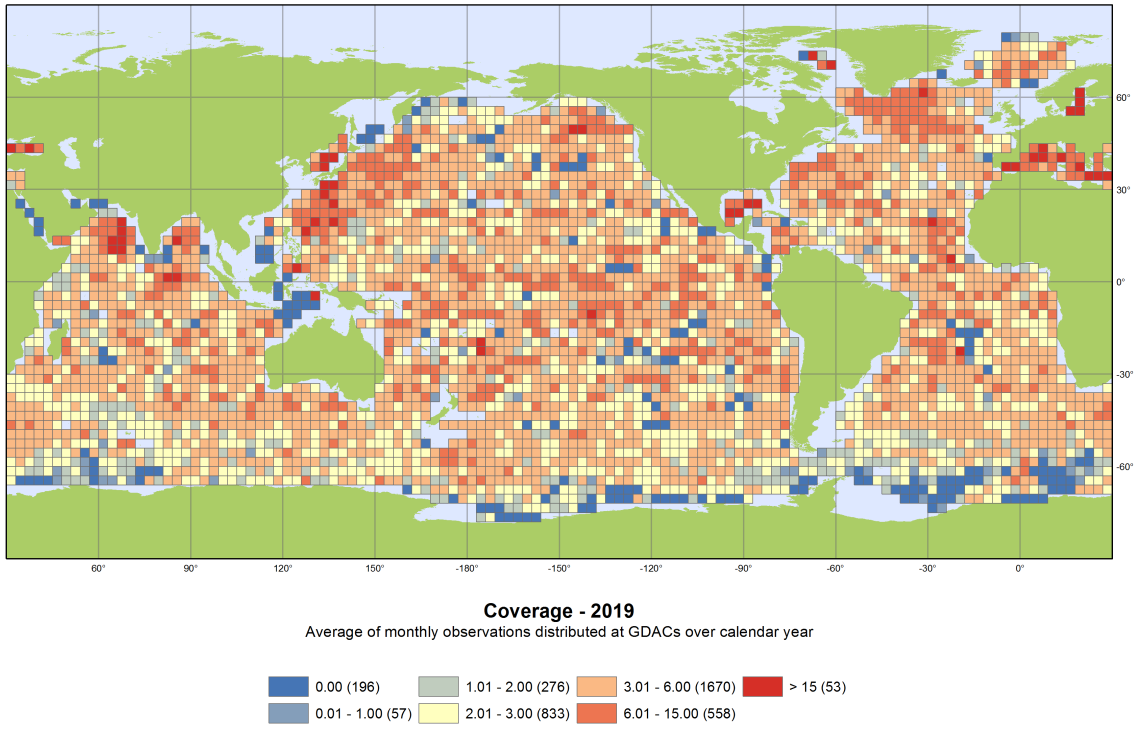

Figure 2.7: Average monthly Argo float observations available in each grid cell globally for the year 2019. There are 22,530 Argo floats deployed as of January 2020 used for monthly analysis (by https://www.metoffice.gov.uk/hadobs/en4/).

The method of objective analysis undergoes continuous validation, adjustment and improvements (e.g., Wijffels et al., 2008; Ishii and Kimoto, 2009; Levitus et al., 2009; Gouretski and Reseghetti, 2010; Good, 2011; Gouretski, 2012; Hamon et al., 2012). One of the most recent developments focused on adjustment for time-varying biases in expendable bathythermograph (XBT) and mechanical bathythermograph (MBT) profiles. Temperature and salinity profile information from many data sources is embedded into the EN4. One of the main data sets used in EN4 is the WOD09. Three other data sets added to EN4 are Arctic Synoptic Basin Wide Oceanography (ASBO) data, Global Temperature and Salinity Profile Program (GTSPP) [U.S. National

Oceanographic Data Center, 2006] from 1990 onward and Argo data for 2000 onwards (GDACs). The data processing of all data sets includes (see Figure 2.8) data control, removal of duplicate observations, quality control and objective analysis.

The data output from this procedure is then processed and stored in a monthly NetCDF format. The gridded data files containing the profiles and quality information from two quality control checks.

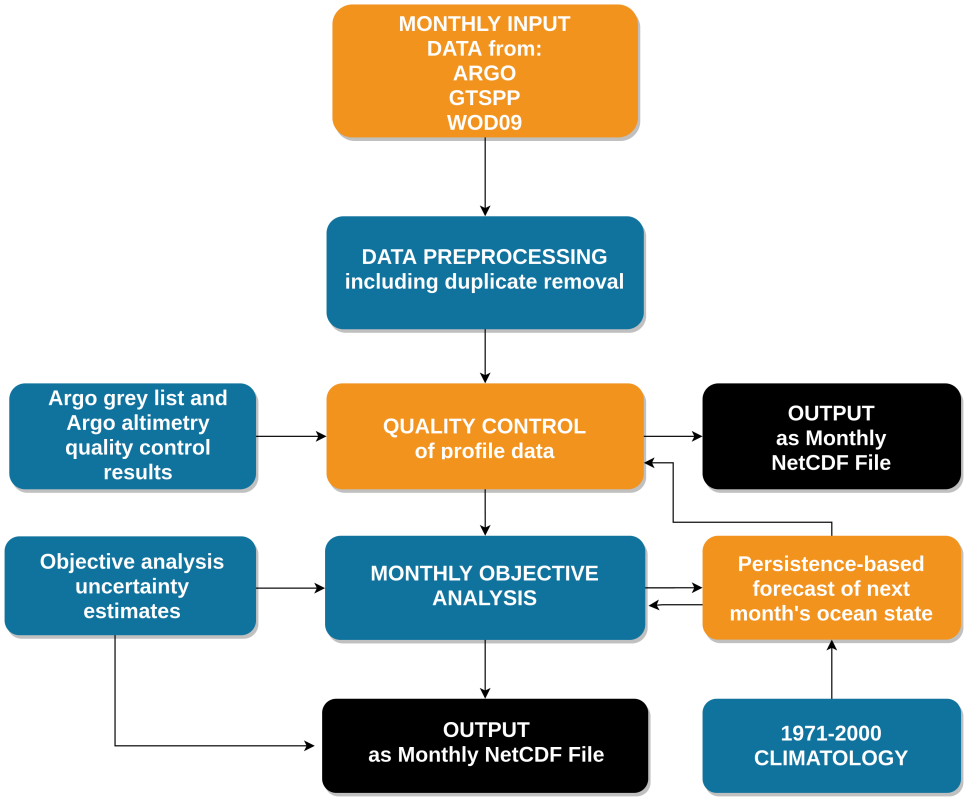

Figure 2.8: Flow of processing performed on the Metoffice EN4 data (Good, et. al., 2013).

Figure 2.9 shows the $\theta - S$ curve of the water masses in the six regions of the studied area calculated from the Argo derived Metoffice EN4 gridded data sets. The

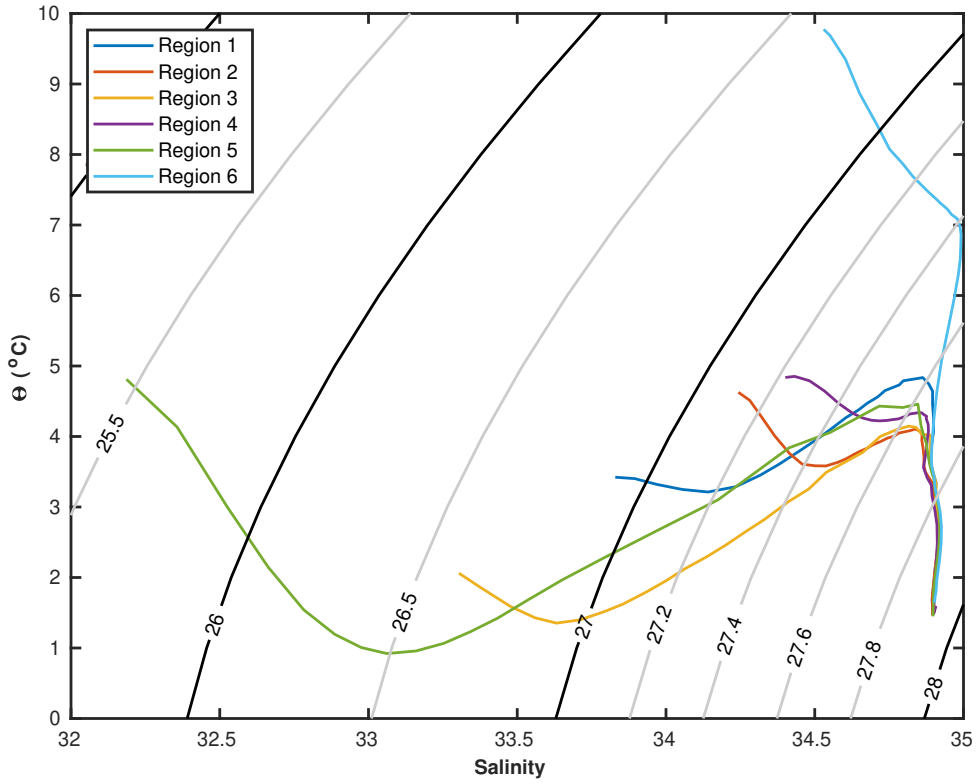

Figure 2.9: The mean $\theta - S$ (potential temperature and salinity) curve for all the subregions for the period 1993-2018.

North Atlantic Deepwater ($\sigma > 27.7$) has relatively homogeneous temperatures and salinities in the six subregions. The intermediate waters ($\sigma > 27.7$) in the subregion 6 (the NAC) is much warmer than the intermediate waters in the other five regions. The $\theta - S$ curves in the intermediate waters of regions 1 to 5 have similar vertical structures with a relatively warm and salty core at $\sigma = 27.6$, which is the Irminger Water (IW) in the Labrador Sea. The salinity rapidly decreases about the IW. This change of salinity is related to the deep vertical mixing of intermediate waters with the fresh waters at the ocean surface.

The surface waters ($\sigma < 27$) in the subregion 6 (the NAC) and subregion 5 (South Labrador Sea, including the Newfoundland Basin) have remarkably different characteristics. The waters in region 6 are the warm and salty waters of the North Atlantic Current. The vertical structure of surface water in the subregion 5 includes a fresh and warm surface layer and cold intermediate layer at about $\sigma \sim 26.5$. The low salinity in the surface is a result of the freshwater terrestrial input and the sea-ice, which is advected into this area and melts there during the spring and summer. The intermediate cold layer forms during the winter and exists throughout the year. The vicinity of regions five and six and the large differences in the water characteristics raises the question about if and how the heat and freshwater transports in these two regions interact and what is the role of the convergence of heat transport (including transport due to the mean current and eddies) for the dynamics of these two regions.

2.2.2 ERA5 Reanalysis of the European Center for Medium-Range Weather Forecasts

This study uses ERA5 reanalysis of the European Center for Medium-Range Weather Forecasts (ECMWF) for surface radiative and turbulent fluxes, sea ice concentration and sea surface temperature. The spatial data resolution is 0.36 degrees in longitude and latitude. The reanalysis is calculated based on ten member-ensembles with 12-hours 4D-Var data assimilation. The output of the atmospheric model is saved hourly on 137 levels. The ECMWF ERA5 reanalysis developed under Copernicus Climate Change Services (C3S) covers the period from 1979 to 2019 and provides data for the global atmosphere, land and ocean surfaces and ocean waves.

ERA5 sea surface temperature and sea ice concentration are computed by using the input of several available data products: MetOffice Hadley Centre HadISST2 for SST and sea ice, the EUMETSAT OSI-SAF for sea ice, MetOffice OSTIA product for SST and sea ice cover. These data sets include uncertainties estimates that depend on flow-dependent uncertainties in the short-range forecasts dependent on observation coverage. Ensemble standard deviation is referred to as the ensemble spread and is calculated as the standard deviation of the 10-members in the ensemble, which is called the uncertainty estimate. However, these uncertainty estimates mostly account for random errors only. The exceptions are the applied perturbations for sea surface temperature (SST) that do incorporate estimates of systematic error.

2.3 Method of the study

This study focuses on the interannual variability of the heat content and the convergence of heat transport. The data used in these calculations include surface net heat flux and gridded in-situ ocean temperature. Both data sets have strong seasonal variations with amplitudes that exceed the interannual changes in many parts of the studied area. A low-pass Butterworth filter with a frequency cutoff of $f_{cut} = 1 year^{-1}$ is applied to remove the seasonal cycle. As discussed in section 1.5, the filter also removes the seasonal variations in the ice enthalpy, which is, in general, difficult to estimate from observational data sets.

The heat flux content of a layer between depths D1 and D2 is calculated as

$$H_{D_1-D_2} = \int_{D_1}^{D_2} \rho_w c_p T \, dz \tag{2.1}$$

where ρ_w is the ocean density, and c_p is the ocean heat capacity. In this study, the heat flux convergence is estimated in four cases:

(i) **The total ocean column**: In this case, the convergence of heat flux is (see Roberts et al. 2017)

$$C_{total} = -\rho_w c_p \left[\nabla \cdot \int_{-D}^{0} (\mathbf{u_h} T - \nu_h \nabla T) dz \right] - \rho c [\nabla \cdot \mathbf{u_i} H_i - q_i] \tag{2.2}$$

C_{total} is a sum of the convergence of horizontal advective and diffusive heat fluxes in the ocean and convergence of sea-ice enthalpy. In this case, $D_1 = -D$ is the depth of the ocean bottom, and $D_2 = 0$ is the ocean surface. The convergence of heat flux is estimated as

$$C_{total} = \frac{\partial H_{total}}{\partial t} - Q_s \tag{2.3}$$

, and

$$H_{total} = \int_{-D}^{0} \rho_w c_p T dz \tag{2.4}$$

(ii) **The surface layer** of depth $D_1 = -150m$. The convergence of ocean heat transport in the surface 150m layer

$$C_{150} = -\rho_w c_p \left[\nabla \cdot \int_{-150}^{0} (\mathbf{u_h} T - \nu_h \nabla T) dz \right] - \rho_w c_p \left[wT - \nu_v \frac{\partial T}{\partial z} \right]_{-150} - \rho c [\nabla \cdot \mathbf{u_i} H_i - q_i] \tag{2.5}$$

C_{150} is a sum of the convergence of horizontal advective and diffusive heat fluxes in the ocean, vertical advective and turbulent heat fluxes at $z = -150m$ and convergence of sea-ice enthalpy. The convergence of heat flux is estimated as

$$C_{150} = \frac{\partial H_{150}}{\partial t} - Q_s \tag{2.6}$$

, and

$$H_{150} = \int_{-150}^{0} \rho_w c_p T dz \tag{2.7}$$

(iii) **The intermediate layer** $D_1 = -2000m$ and $D_2 = -150m$. The convergence of ocean heat transport in the intermediate 150-2000 m layer

$$C_{int} = -\rho_w c_p \left[\nabla \cdot \int_{-2000}^{-150} (\mathbf{u_h} T - \nu_h \nabla T) dz \right] - \rho_w c_p \left[wT - \nu_v \frac{\partial T}{\partial z} \right]_{-2000}^{-150} \tag{2.8}$$

C_{int} is a sum of the convergence of horizontal advective and diffusive heat fluxes in the ocean and the convergence of vertical advective and turbulent heat fluxes in the layer between -2000 m and -150 m depth. The convergence of heat flux is estimated as

$$C_{int} = \frac{\partial H_{int}}{\partial t} \tag{2.9}$$

, and

$$H_{int} = \int_{-2000}^{-150} \rho_w c_p T dz \tag{2.10}$$

(iv) **The Deep layer** between the bottom and the convergence of ocean heat transport in the surface 150m layer

$$C_{bot} = -\rho_w c_p \left[\nabla \cdot \int_{-D}^{-2000} (\mathbf{u_h} T - \nu_h \nabla T) dz \right] - \rho_w c_p \left[wT - \nu_v \frac{\partial T}{\partial z} \right]_{-D}^{-2000} \tag{2.11}$$

C_{bot} is a sum of the convergence of horizontal advective and diffusive heat fluxes in the ocean, the convergence of vertical advective and turbulent heat fluxes between z=-2000m and bottom of the ocean. The convergence of heat flux is estimated as

$$C_{bot} = \frac{\partial H_{bot}}{\partial t} \tag{2.12}$$

, and

$$H_{bot} = \int_{-D}^{-2000} \rho_w c_p T dz \tag{2.13}$$

The computation of the heat flux separately for the surface (ii), intermediate (iii), and deep (iv) layers aims to identify the heat flux convergence in these three layers, which play an important role in the surface air-sea exchange, LSW formation, and transport of deep waters. Within the approach used in this study, we need to consider that hear flux convergence includes the contributions of the vertical component of heat transport to the convergence of heat transport. This transport may be significant, especially in subregion 2 of deep convection. The heat budget for the total water column in (i) includes only the horizontal convergence of heat transport.

Met Office Gridded Argo data, following rigorous data controls, quality checks and objective analysis (Figure 2.8), also releases uncertainty estimates for potential temperature and salinity for each depth. The associated uncertainties for heat content are quantified using equation 2.1.

Chapter 3

Surface Heat Fluxes and Sea Ice

Interaction between the ocean and the overlying atmosphere is a key dynamical process that influences the global climate and its variability. Oceans have a large heat capacity and display an inherently longer time scale for variations (interannual to decadal and interdecadal). The heat fluxes at the ocean-atmosphere interface, which have shorter dominant time scales from intraseasonal to seasonal, are believed to generate large-scale and long-lasting anomalies in sea surface temperature (SST) anomalies and Ocean Heat Content. In the North Atlantic, most of the heat gained in tropical regions is transported northward through Gulf Stream and impacts the SST, atmospheric heat gain, precipitation, fresh water influx, river runoff, and melting of sea ice in subarctic and Arctic.

Air-sea heat exchange in the North Atlantic Ocean, which depends on local near-surface characteristics of the atmosphere and ocean, influences both the atmosphere and ocean. Short-term variations of air-sea fluxes affect the SST and ocean heat content, which are additionally modified by longer-term variations in ocean dynamics.

Previous studies indicated that the surface mixed layer in subpolar North Atlantic and the atmosphere can be considered as a fast dynamical system driven by short-term variations in the air-sea heat flux regulated by long-term variations in the meridional heat transport (Cayan, 1992).

3.1 The Sea Surface Temperature

The variations in the SST are associated with variability in the near-surface air temperature, humidity, and winds, the sea-ice extent, and advection by the main current systems. The ECMWF Reanalysis (ERA5) of the climatological annual mean sea surface temperature (SST) in the Western Subpolar North Atlantic is shown in Figure 3.1. This dataset is averaged over the period from 1993 to 2018 from 10 ensemble members of ERA5 data. In the part of the ocean north of 50 ^oN, which is covered with sea-ice during much of winter, the annual mean temperature estimate is close to 0 ^oC. The lowest SST is observed in the Baffin Bay and off the coasts of Greenland, Labrador and Newfoundland. An area of high SST gradients separates the area of low temperature to the north from the waters of Gulf Stream. Another area of high SST gradient is observed between the waters of Eastern Greenland Current (EGC) and waters of the Irminger Sea.

Figure 3.2 shows monthly mean sea surface temperature averaged over each of the six regions from 1993 to 2018. The surface temperature in the regions one, two, three, four, and six show a meridional variability with the highest temperatures in the Gulf Stream region (six) and lowest in northern region three. The amplitude of the seasonal cycle in these regions is close and varies between 6 and 7 ^oC. The

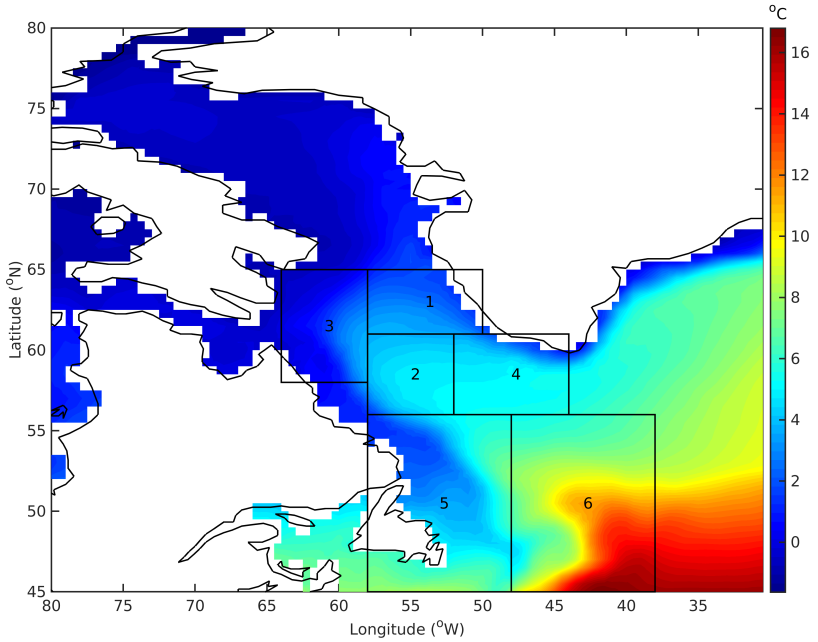

Figure 3.1: Mean Sea Surface Temperature for the period 1993-2018.

amplitude of the seasonal cycle of SST in region five is almost twice higher than in the other five regions and is about 11.5 ^oC. A major contribution to this high seasonal variability has the low SST in this region during the winter and early spring. During this period, region five is partly covered by ice. In the spring, sea-ice is also advected into this region from the northern Labrador Sea. The ice melt in spring produces low surface temperatures in March-April. Region one, three and four are also completely or partly covered in the sea ice during winter and experience the melt during spring; however, the anomalies in SST are not intense as that sea ice is formed there, unlike region five, where the sea-ice is advected from the north.

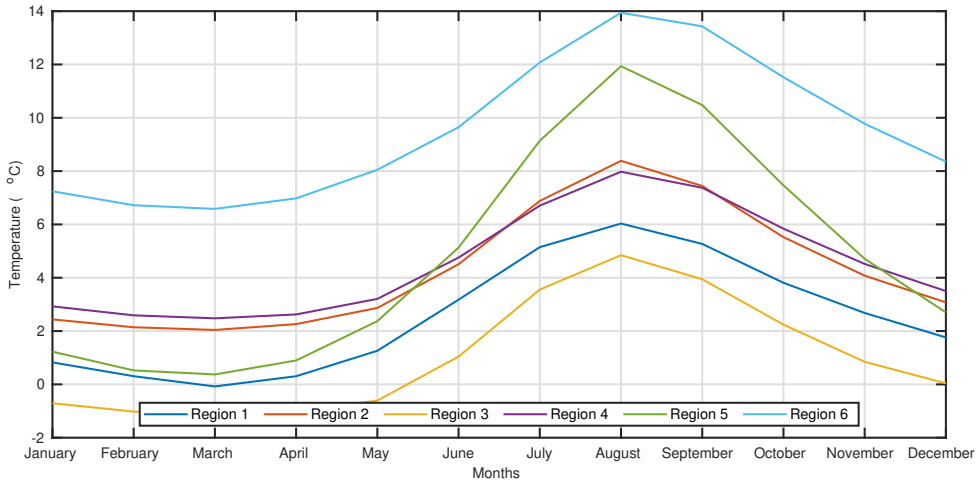

Figure 3.2: Mean Seasonal Cycle of Sea Surface Temperature for all the subregions 1-6 calculated for the period 1993-2018.

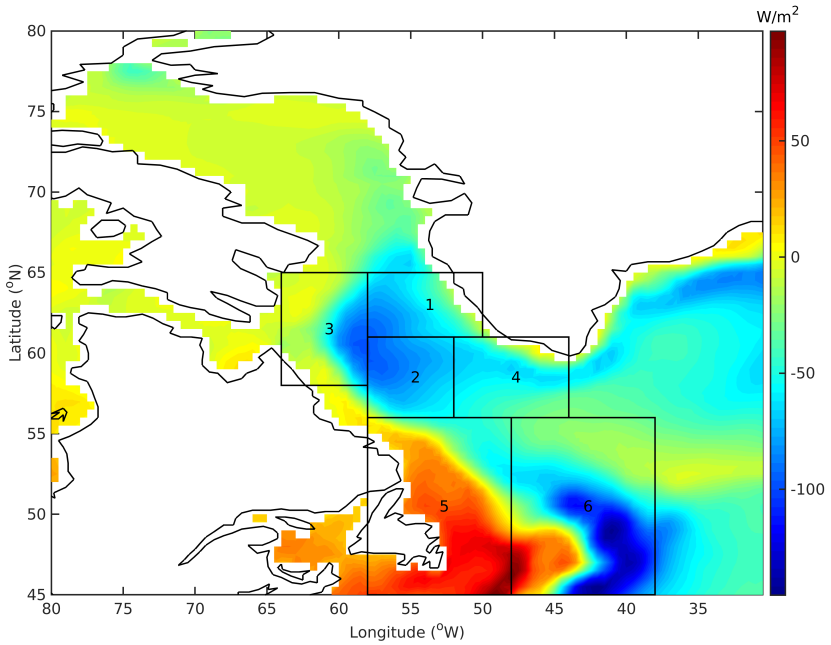

Figure 3.3: Mean Net Surface Heat Flux for the period 1993-2018.

3.2 Surface Heat Flux

Air-sea heat flux plays a fundamental role in the dynamics of the North Atlantic Ocean. This study focuses on the variations in ocean heat content, which are driven by the dynamics of ocean currents and transport, and air-sea fluxes. In order to quantify the heat content variations forced by the atmospheric heat flux and ocean circulation, it is important to investigate the surface heat flux, its components, their seasonality and their interannual trend.

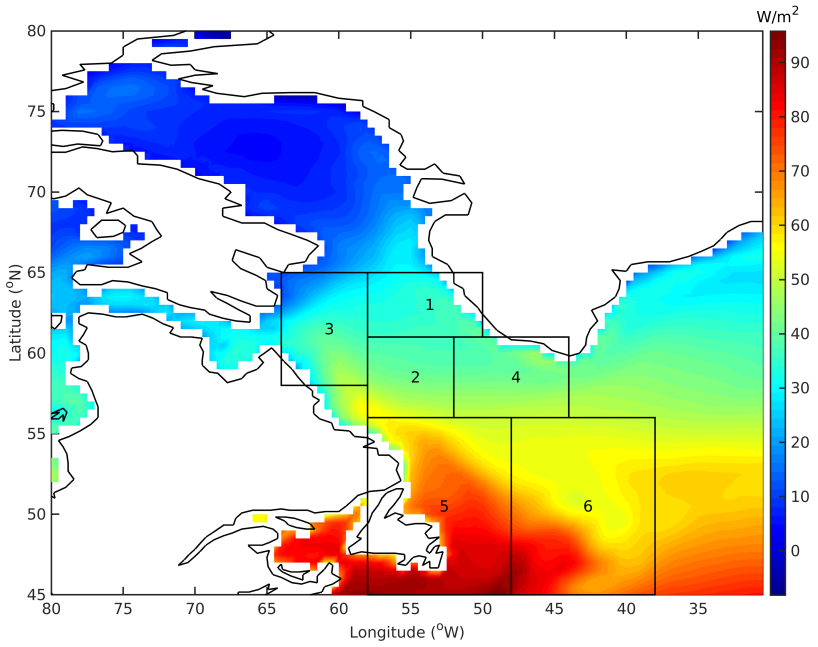

Figure 3.4: Mean Radiative Heat Flux for the period 1993-2018.

Figure 3.3 shows the spatial distribution of mean net surface heat flux, which calculated as a sum of its radiative and turbulent components.

$$Q_{net} = Q_{radiative} + Q_{turbulent}$$

3.2.1 Radiative Heat Flux

The Earths radiative budget is between absorbed solar radiation and the emission of the terrestrial radiation back to space. At the surface of the plane, the radiation balance is comprised of two components —net shortwave and net longwave heat flux. Each of these two components is separated into a part that is emitted up from the ocean surface and a second downward part into the ocean.

$$Q_{radiative} = (SW)_{down} - (SW)_{up} + (LW)_{down} - (LW)_{up}$$

The SW is the shortwave(wavelength 0.3-4.0 μm), and LW is the longwave (wavelength 4.0-100.0 μm) components of the radiative heat flux $Q_{radiative}$. There are uncertainties in the estimates from reanalysis models of the radiative fluxes due to limitations in the cloud-resolving schemes, which still underrepresent the temporal and spatial resolutions of governing physical processes. Figure 3.4 shows the surface mean net radiative flux averaged from 1993 to 2018. The mean radiative heat fluxes vary zonally and decrease from about 90 W/m^2 in the south to about 10 W/m^2 in the northwest. The incoming radiative heat fluxes depend on the incident solar energy and sea surface temperatures. These two factors cause radiative heat fluxes to decrease with an increase in latitude as higher latitudes.

The area mean radiative fluxes (Figure 3.5) vary seasonally with a minimum in January, which in most of the regions is between -50 - 60 W/m^2 and maximum in

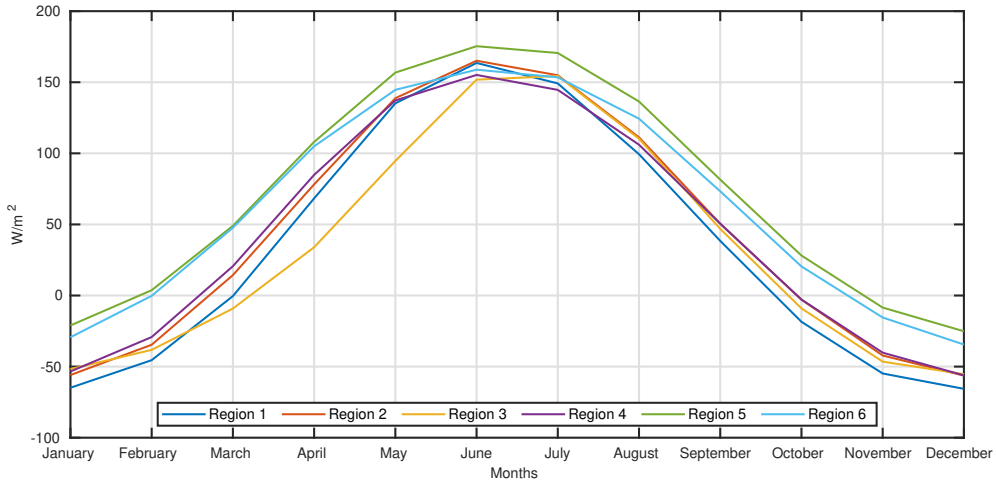

Figure 3.5: Mean Seasonal Cycle of Radiative Flux for all the subregions 1-6 for the period 1993-2018.

June of about 150 W/m^2. The major differences occur in region three, which is partly covered by sea-ice in the spring. The southern regions of Gulf Stream (region six) and Newfoundland basin (region five) get more radiative heat than the other regions. While the magnitude of radiative heat is different for all regions for the magnitude of seasonal variations is very similar in the whole area of the study.

3.2.2 Turbulent Heat Flux

Turbulent heat flux($Q_{turbulent}$) comprises of two components - sensible (SH) and latent heat flux (LH). They are commonly estimated using bulk transfer relations

$$LH = -L\rho C_E W_{10}(Q_{a10} - Q_s)$$

$$SH = -C_p\rho C_H W_{10}(T_{a10} - T_s)$$

$$Q_{turbulent} = LS + SH$$

where W_{10}, Q_{a10} and T_{a10} are the surface winds, specific humidity and air temperature at 10 m height, Qs is saturation specific humidity at sea surface temperature Ts. L is the latent heat of evaporation ($2.45X10^{-6}J/Kg$), and $C_p = 1005J/Kg$ is the specific heat of the air, and ρ is the air density. The bulk transfer coefficients for latent heat (C_E) and sensible heat flux (C_H).

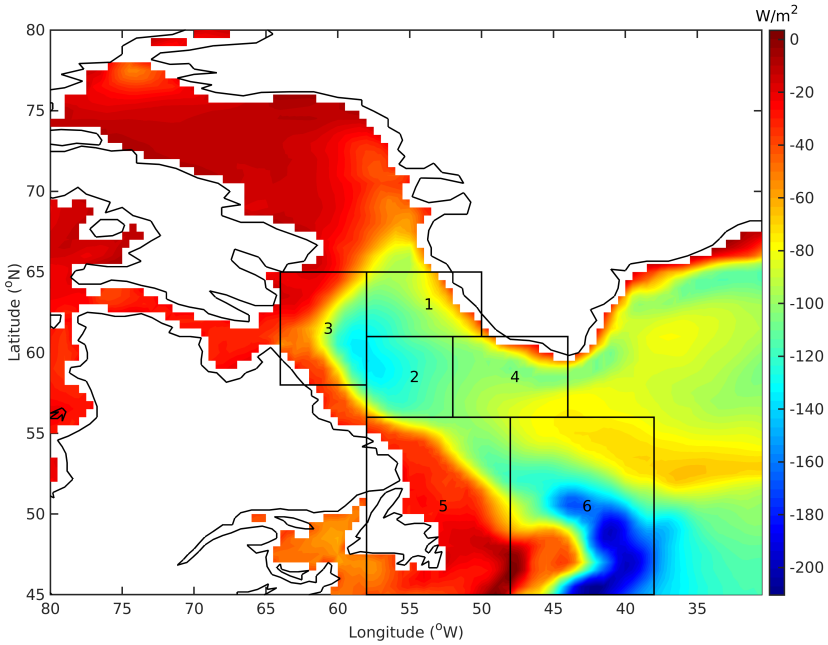

Figure 3.6: Mean Turbulent Heat Flux for the period 1993-2018.

Figure 3.6 shows the mean net turbulent heat flux components averaged from 1993 to 2018. The annual mean turbulent heat fluxes increases from about -200 W/m^2 to about -20 W/m^2 from Southeast to Northwest of subpolar North Atlantic. The highest heat loss is over the Gulf Stream. Due to the warm SST, the winter

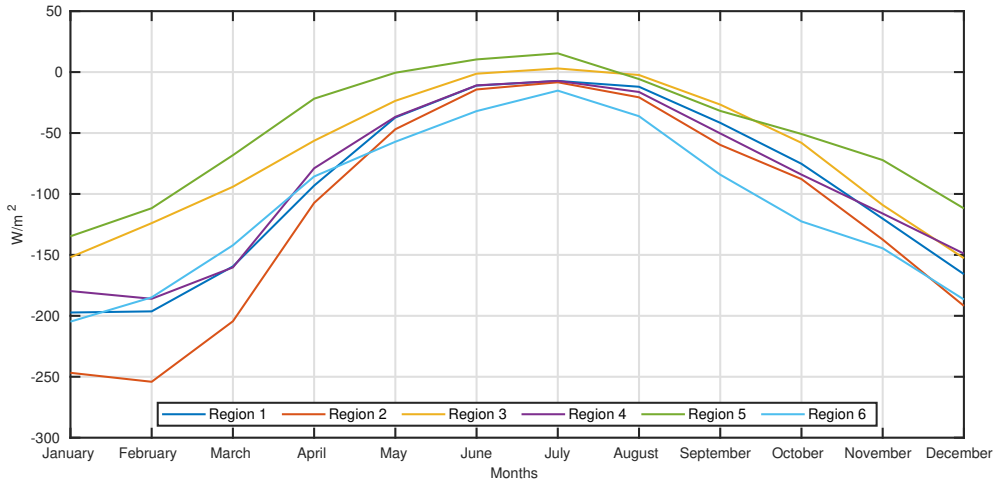

Figure 3.7: Mean Seasonal Turbulent Heat Flux for all the subregions in the period 1993-2018.

air-sea temperature contrast, there is significantly higher. Intense air-sea turbulent heat flux is present also over the areas of deep convection in Labrador and Irminger Seas. The intense vertical turbulent exchange in the water column in these two regions during the winter season mixes the surface water masses with intermediate waters, maintaining in this way a high air-sea temperature contrast. Due to the small depths, the water columns in the shallow coastal areas of Greenland and Labrador have smaller heat capacity. They cool relatively fast in the winter and get partly covered by sea-ice. This reduces the surface heat exchange, and the ocean turbulent heat loss is low in these areas.

The seasonal variations (see Figure 3.7) in regions one, six and four have very similar seasonal variations with a minimum of -200 W/m^2 in winter and about -50 W/m^2 in summer. The winter heat lass in the coastal regions three and five is relatively small. The highest turbulent heat loss in winter is found in the deep

convection region two which is about 250 W/m^2

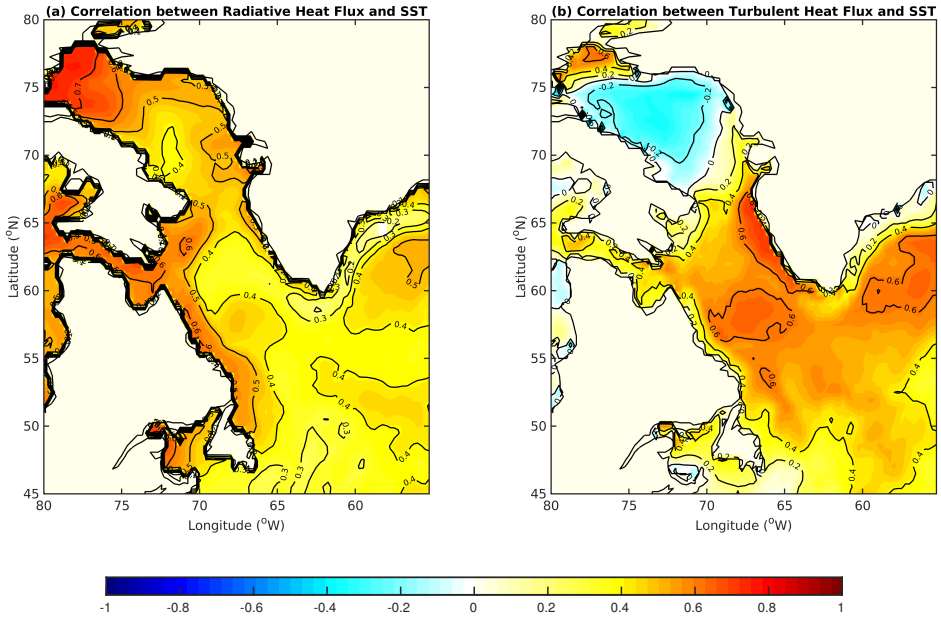

Figure 3.8: Correlation between Sea Surface Temperature and (a) Radiative Heat and (b) Turbulent Heat Flux respectively for the period 1993-2018.

3.3 Sea Ice Concentration

Sea-ice forms at the surface when the ocean waters reach freezing temperatures. The freezing sea water in winter forms ice crystals of pure water and ejects salt. This process called brine rejection increases salinity and density of subsurface waters. The brine rejection can initiate downward convection and promotes vertical ocean mixing. The sea-ice modifies the ocean albedo and near-surface ocean characteristics and effects the radiative and turbulent heat fluxes. It directly impacts the surface air-sea fluxes by capping the upper layer of the ocean and preventing the exchange of heat

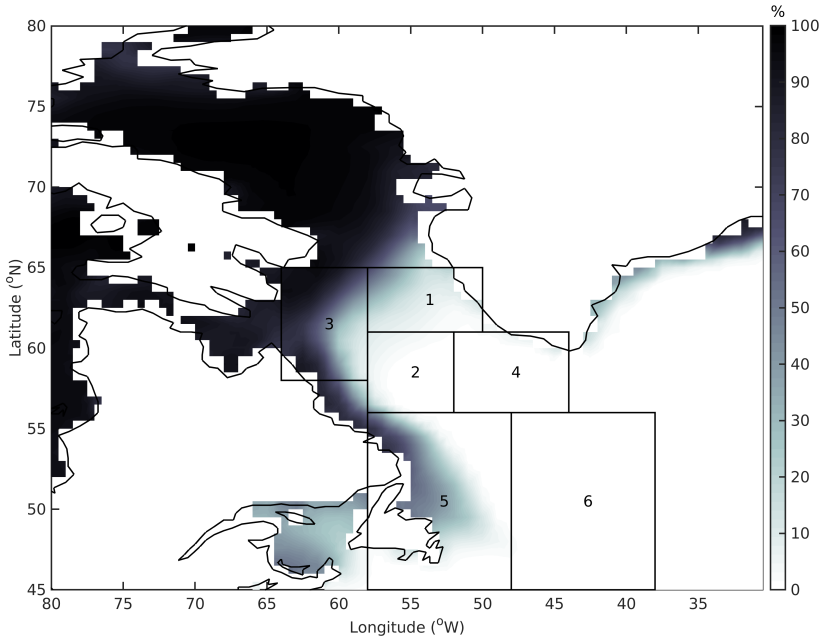

Figure 3.9: Mean sea ice concentration for March 1993-2018

and moisture between the ocean and the atmosphere. Therefore, the formation and melting of sea-ice have a significant impact on surface heat flux.

The sea ice concentration is a characteristic that determines the percentage of the surface ocean area covered by ice. The monthly map of sea ice concentration using data from ERA5 for March is shown in Figure 3.8. The climatological ice concentration is close to 100% in the northern part of the Labrador Sea, Hudson Strait and off the coast of Labrador. In the spring, this ice melts and is transported downstream of the Labrador Current. Large parts of subregion one, three and five remain covered in sea ice through the winter. Sea-ice forms only in the western part of subregion two (central Labrador Sea) while its central part remains ice-free throughout the year.

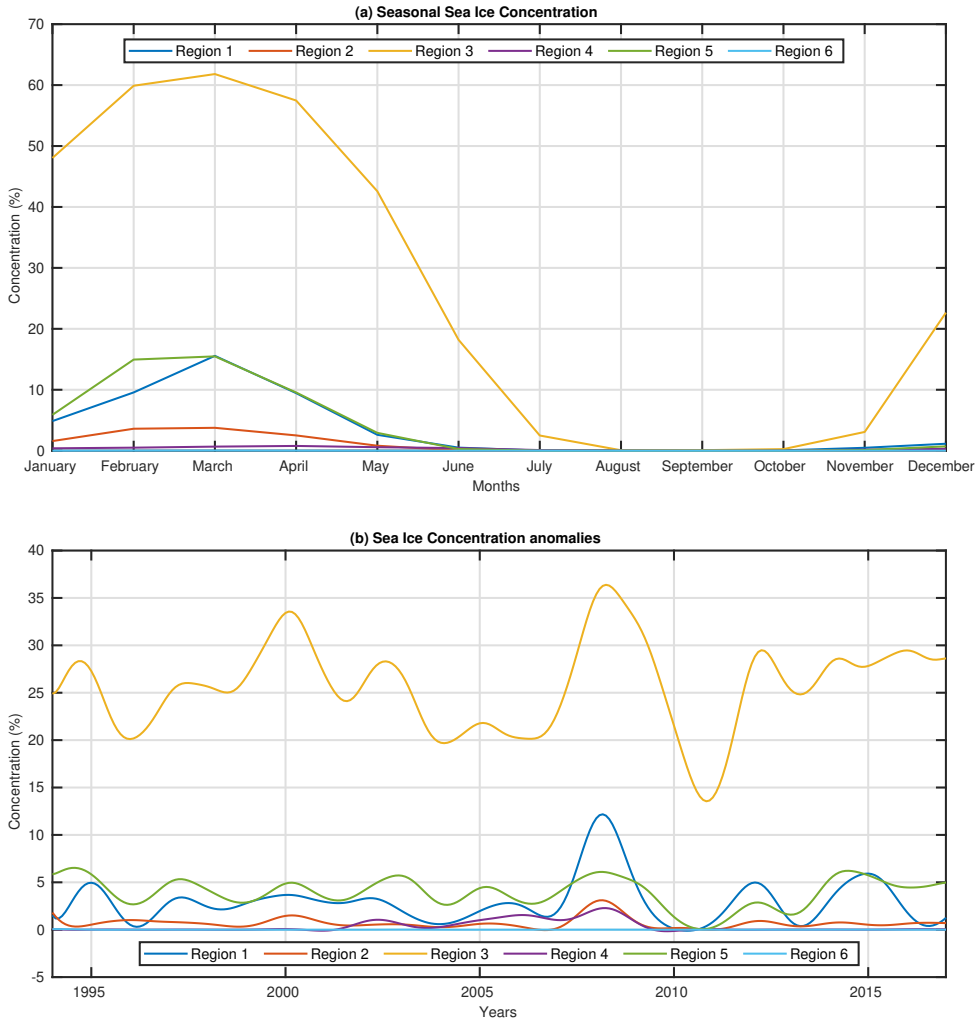

Figure 3.10: (a) Mean Seasonal Sea Ice Concentration, and its (b) Interannual variability for all the subregions 1-6 for the period 1993-2018.

The seasonal time series of sea ice concentration is shown in Figure 3.10a for the six subregions, and the interannual time series is shown in Figure 3.10(b). Ice forms in the winter months December-March in mostly subregions one, three and five melts in April-July. All regions are ice-free in summer from August to October, where sea ice concentration is at minima. The interannual variations (Figure 3.10b), after

removing seasonal cycle using low-pass butterworth filter (with a frequency cutoff of $f_c = 1year^{-1}$), show a maximum in sea ice concentration for all subregions in 2008-2009, following a steady decline in the period 2000-2007 in the subregion 3. All the subregions exhibit a sharp decline in the warm year 2010-2011, followed by another cooling period since 2012.

Chapter 4

Ocean Heat Content

The ocean heat content variability in the six regions shown in Figure 1.2 is calculated for (i) the surface 150 m layer, (ii) the intermediate layer from 150 m to the depth of 2000 m, (iii) the bottom layer that extends from 2000 m to the bottom of the ocean, and (iv) for the whole water column. The surface layer directly communicates with the atmosphere, and the variations in its heat content are influenced by surface net heat flux. The tendency ($\partial H/\partial t$) of the heat content in the intermediate and bottom layers equals to the convergence of ocean heat transport. This transport includes two components — one due to the advection by ocean currents and a second due to the turbulent mixing.

The area of this study includes the regions of (1) of formation of Irminger rings, (2) of formation of the Labrador Sea Water (LSW) (Lazier et al. 2002), (3) of inflow from the Buffin Bay and Hudson Strait, (4) of entrance of the Irminger waters in the Labrador Sea, (5) export of the LSW from the area of deep water formation, (6) of the North Atlantic Current. All six regions have unique and important roles in the

formation of the heat budget of the Labrador Sea. Our goal is to estimate what is the contribution to the heat budget of the advective and eddy-induced heat transport in these regions.

Figure 4.1 shows the annual mean ocean heat content for (a) surface layer, (b) intermediate, (c) bottom layer and (d) total ocean column. The surface 150 m layer in the subpolar ocean is well-mixed for most of the time of the year, and the heat content (Figure 4.1a) resembles the main pattern of SST distribution. The Gulf Stream area (region 6) has the highest heat content in the top layer of about $1.8 \times 10^8 KJ/m^2$. The heat content decreases in the northern part of the studied region following the decrease of the temperature. The shallow regions off the coasts of Greenland, Labrador, Newfoundland, and Gulf of St. Lawrence have low values of heat content because of their small depth which is less than 150m. The dependence of heat content on the bottom depth is well seen also in the distribution of the heat content in the intermediate (Figure 4.1b) and deep (Figure 4.1c) layers.

The warm subtropical Atlantic waters enter the studied areas along the North Atlantic Current in the subregion six. These waters, which have high content (Figure 4.1d), progress northward towards the eastern subpolar North Atlantic. Part of this heat is released in the subregion six (see Figure 4.1) due to the type of processes — surface heat flux and convergence of advective and eddy-driven heat transport. As the North Atlantic Current (NAC) extends northeastward, its waters are gradually cooled and mixed. The multiple branches of the NAC bring these waters in the Eastern Subpolar North Atlantic, Nordic Seas, and around the Irminger Sea.

The Irminger Water (IW), which is a remnant of the highly modified North Atlantic Current waters enter the Labrador Sea in its eastern part in the subregion four

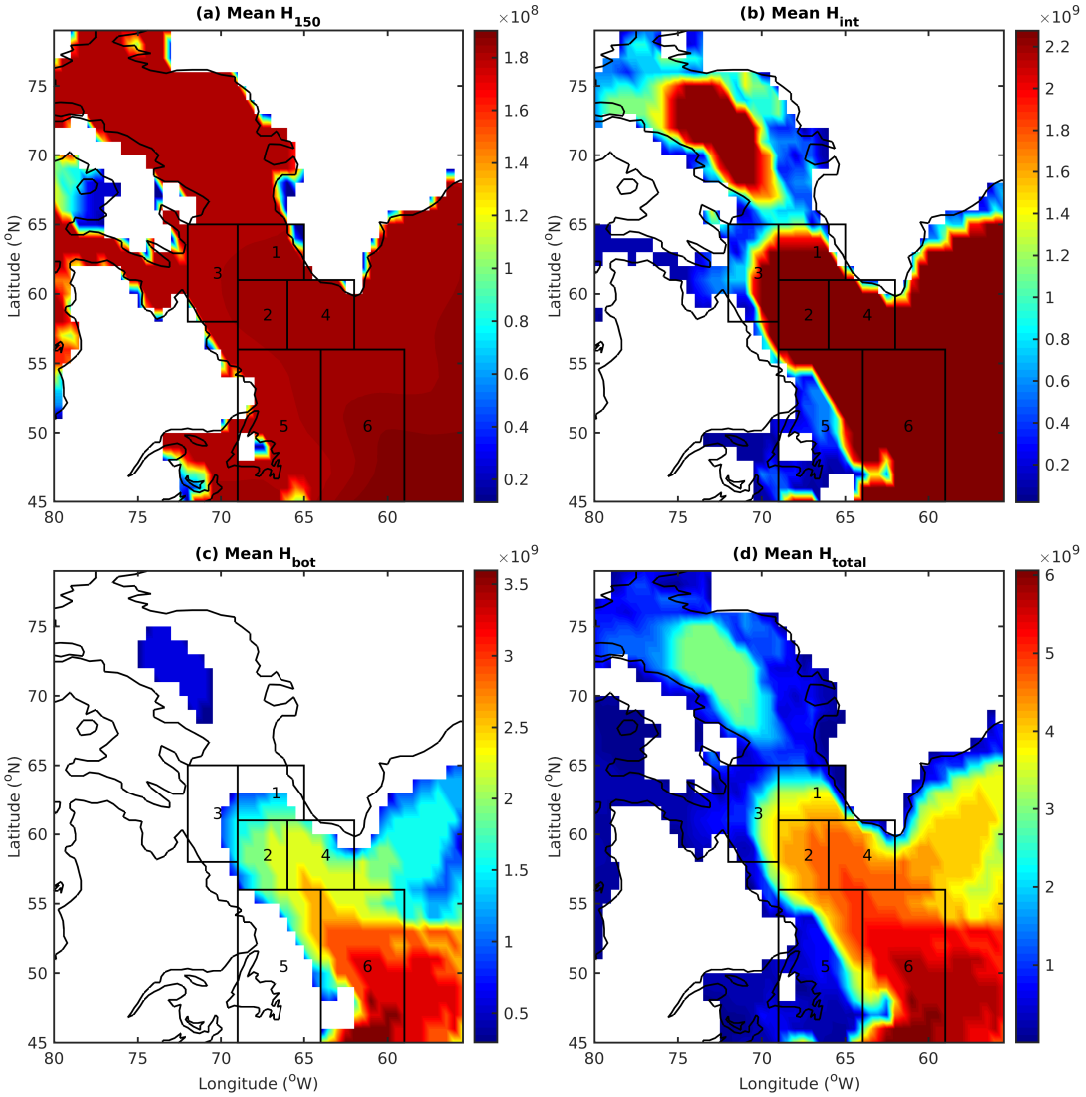

Figure 4.1: Annual Mean Ocean Heat Content in (a) surface, (b) intermediate, (c) bottom, and (d) total ocean column in the Western Subpolar North Atlantic Ocean from the year 1993-2018 (KJ/m^2).

(Figure 4.1). The IW, which is relatively warm and salty, is transported mostly in the intermediate layer by the narrow boundary current. The export of heat from these waters towards the subregion two in the central part of the Labrador Sea is

predominantly due to eddy-induced transport. Relatively large eddies form by the instability of the boundary currents and move predominantly towards the central part of the Labrador Sea, bringing cores of warm and salty IW offshore. The most intense eddy-induced transport occurs in the area of the formation of Iminger Rings in the subregion one. The Irminger Rings are large eddies with spatial scales of the order of 50 to 100 km, which shedding from the boundary current mostly in the subregion one and moving towards the central Labrador Sea.

The subregion three is near the mouths of Hudson and Davis Straits. The heat content in this region is influenced by the waters of the Baffin Bay and Hudson Strait. This is also the region of formation of the Labrador Current, which brings cold and fresh waters along the coast of Labrador. The subregion two in the central Labrador Sea is the key region for understanding the heat budget of the whole Labrador Sea. This is the region of deep convection and formation of intermediate Labrador Sea Water (LSW). The lateral eddy-driven heat exchange with subregions one, three and four are essential for the heat budget of this region and restratification of the Labrador Sea in the spring and summer. The export of LSW from the subregion two feeds the lower limb of the Atlantic Meridional Overturning Circulation (AMOC) and spreads into the subregions four, five and six.

The subregion five, where the Deep Western Boundary Current exports a major portion of the LSW equatorward, is also a region of intense surface air-sea interaction (see Figure 3.6). Understanding the physical processes governing the variability of heat content (Figure 4.1) is important for the understanding of the dynamics of the Labrador Sea and AMOC. Some of the elements of these processes, like narrow boundary currents, deep convection, mesoscale eddy-driven heat transport, are un-

resolved in the data set used in this study. This study focuses on their integrated contribution to the heat budget of the six regions based on observations.

The heat flux content (H) in Figure 4.1 is an important characteristic for understanding the heat budget of the Labrador Sea. As a vertical integral over certain depths range, H depend not only on the temperature but also in the bottom depth. In Figure 4.1, the large heat content is observed in areas with great bottom depths. Our approach is to use these characteristics to calculate the heat content tendency together with surface net heat flux to provide information about the heat flux convergence, which determines the rate of local heat gain and loss due to ocean heat transport in the water column.

4.1 Heat flux convergence in the Surface Layer

Figures 4.2-4.7 show the heat content H, its tendency, surface heat flux and convergence of heat advection for the six regions. The upper panels (Figures 4.2a-4.7a) in these figures shows the heat content H_{150} in the surface 150 m layer and its tendency $\partial H_{150}/\partial t$. The second panels (Figures 4.2b-4.7b) show the net surface heat flux. The third panel (Figures 4.2c-4.7c) presents the heat flux convergence in the surface layer, and the bottom panels (Figures 4.2d-4.7d) show the heat flux convergence in the intermediate and deep layers.

The types of temporal variabilities of the heat content, surface heat flux and heat flux convergence fall into two groups when considering the magnitudes of these characteristics. The magnitudes of these characteristics in the first group, including the subregions one, two, three and four, are between two and three times smaller than

in the second group, including the subregions five and six. Notice that in order to represent this difference, the axes on figures 4.2-4.5 were chosen to have a different range than the ones in Figures 4.6-4.7. The patterns of the variability of the main components of the heat budget are also different in these two groups of regions.

The anomalies of heat content in the first group of regions (Figures 4.2a-4.5a) are low and negative at the beginning of the period of the study. They all have high positive values in the winters of 2003-2004 and 2010-2011 and low and negative values in the winter of 2008-2009. The heat content anomaly in this group of regions was also negative since 2012. This pattern of variability is seen with different magnitude in all of the regions. In between these years, the heat content variability in these regions is different depending on the local ocean dynamics. This variability of heat content is related to the tendency shown with the red line in Figures 4.2a-4.5a. The tendency in all of the regions in group one shows the presence of oscillations with a period of two-to-three years.

There are major differences between the heat budgets in the surface layers in the subregions five and six from the other four regions. Firstly, the heat content variations in these two regions are significantly higher than in the subregions one, two, three and four. The interval of variation of the heat tendency (orange line in the upper panels of Figures 4.6 and 4.7) is between -10 TW to 10 TW. For comparison, the tendency of heat content in the other four regions (Figure 4.2-4.5) changes approximately from -5 TW to 5 TW. Both sources of heat, the surface net heat flux (second panels in Figures 4.2-4.7) and heat flux convergence (third panel in Figures 4.2-4.7), equally contribute to the high variability of heat tendency in the subregions five and six. Secondly, the long-term positive trend in 1993-2004 and heat content decay between

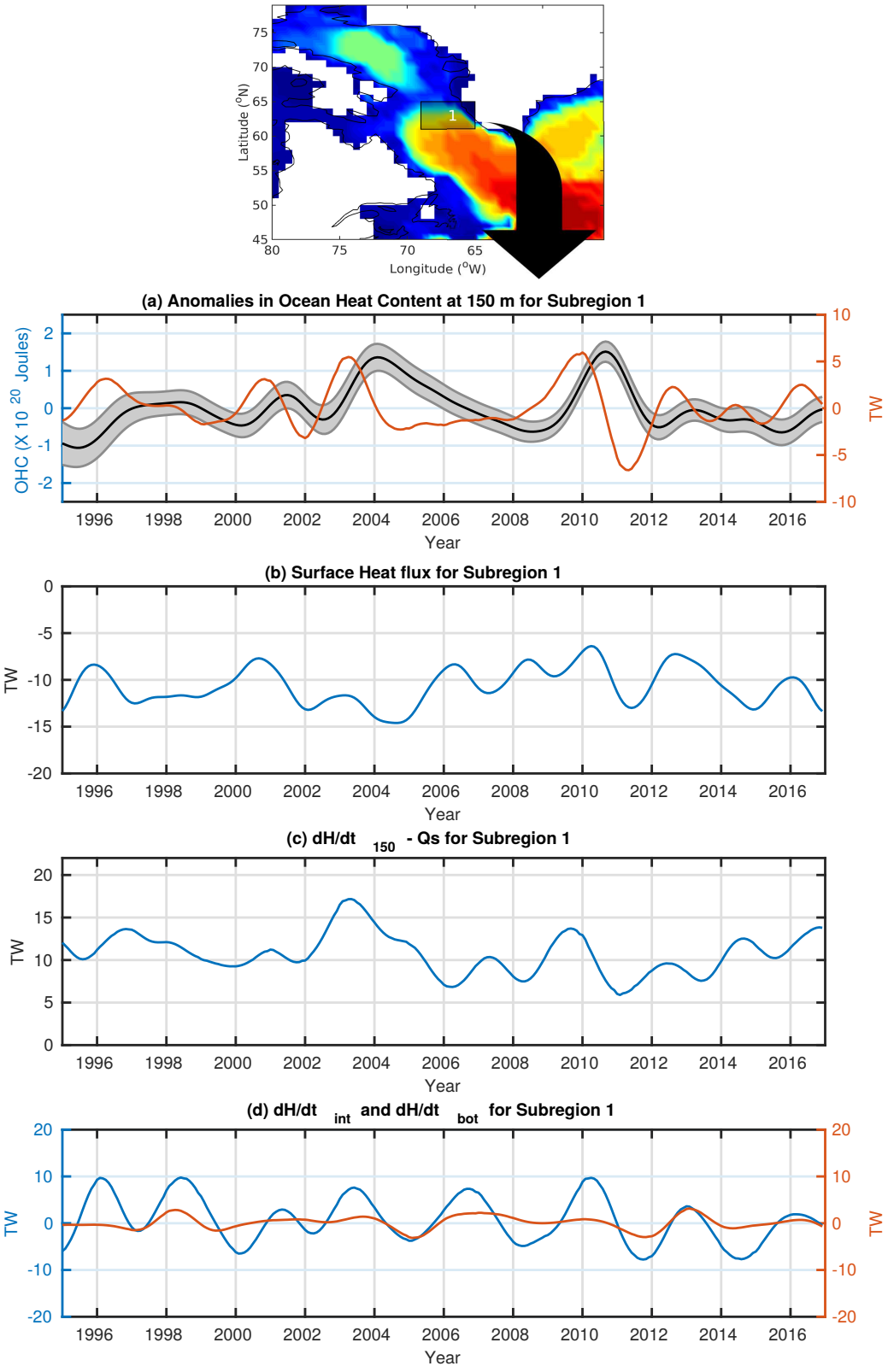
Latitude (°N)
Longitude (°W)
1
(a) Anomalies in Ocean Heat Content at 150 m for Subregion 1
OHC (X 10 20 Joules)
TW
Year
(b) Surface Heat flux for Subregion 1
TW
Year
(c) dH/dt 150 - Qs for Subregion 1
TW
Year
(d) dH/dt int and dH/dt bot for Subregion 1
TW
Year

Figure 4.2 *(previous page)*: The components of the heat budget in the subregion one. (a) Interannual anomalies of the heat content (H_{150}) (black) and rate of heat storage ($\partial H_{tot}/\partial t$) (orange) for the surface layer, (b) interannual net surface heat flux (Q_s), (c) estimated convergence of ocean heat transport (C_{150}) for the surface layer, and (d) the convergence of heat transport in intermediate (150-2000 m) in blue and bottom layers (below 2000 m) in orange. The map above, which shows the mean total heat content for the period 1993-2018, highlights the region of interest.

2004 and 2009 observed in the heat content of surface layers in the subregions one, two, three and four are much weaker and almost not present in the subregions five and six.

4.2 The convergence of heat transport in the intermediate, deep layers, and whole water column.

The heat flux convergence in the intermediate (150-2000m) and deep layers (2000m-bottom) are shown in the bottom panels of Figures 4.2-4.7. The heat flux convergence in the intermediate layers in all six regions exceeds the convergence of heat transport in the bottom layer. The temperature gradients and velocity magnitudes in the deep layers are significantly smaller than at intermediate depths, which reduces the heat flux convergence. The magnitude of variation of heat flux convergence in the intermediate layers (blue curves in Figures 4.2d-4.7d) is, in general, higher than the same characteristics for the surface layer (Figures 4.2c-4.7c).

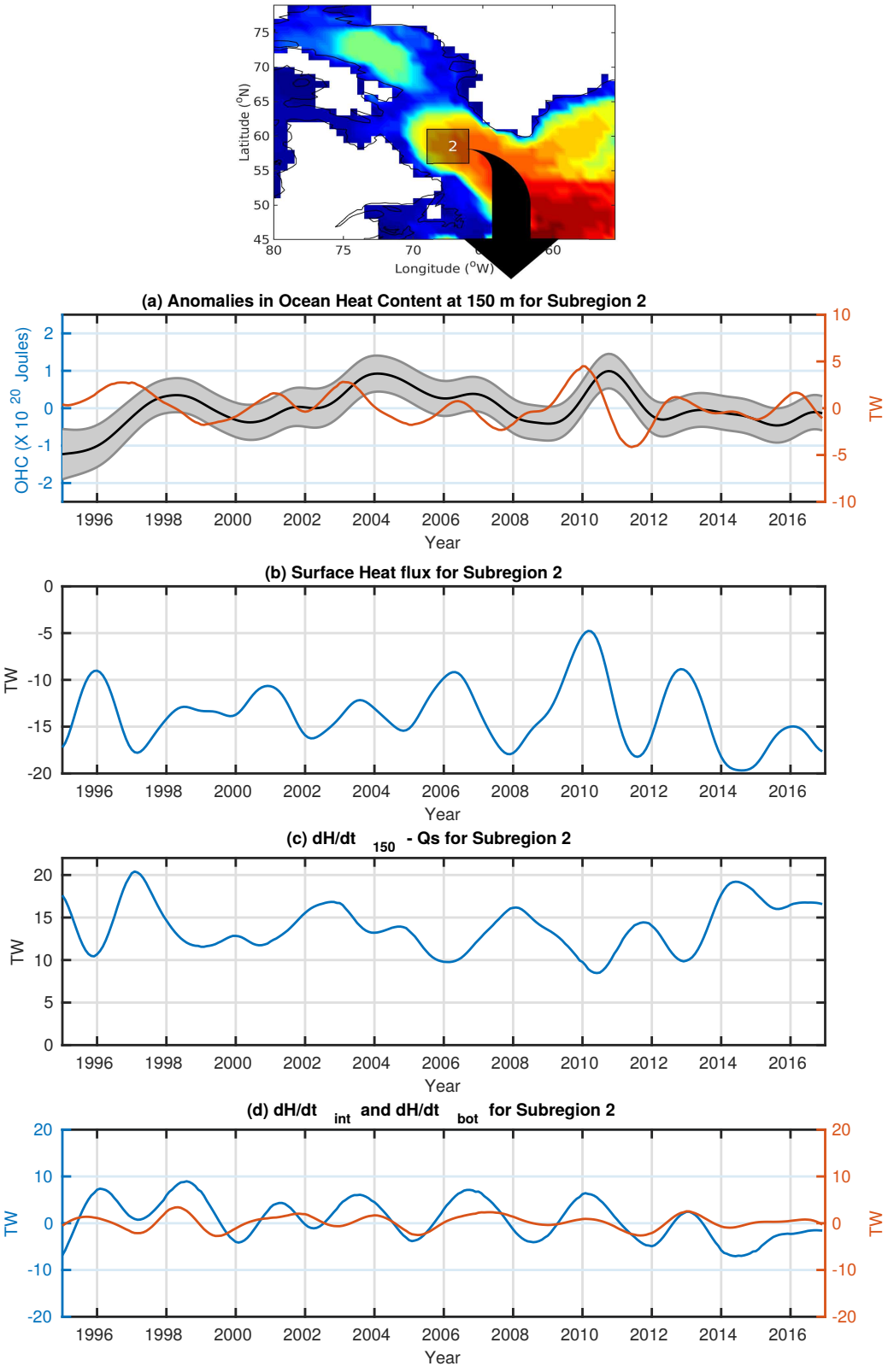

Figure 4.3: Same as Figure 4.2, but for the subregion two.

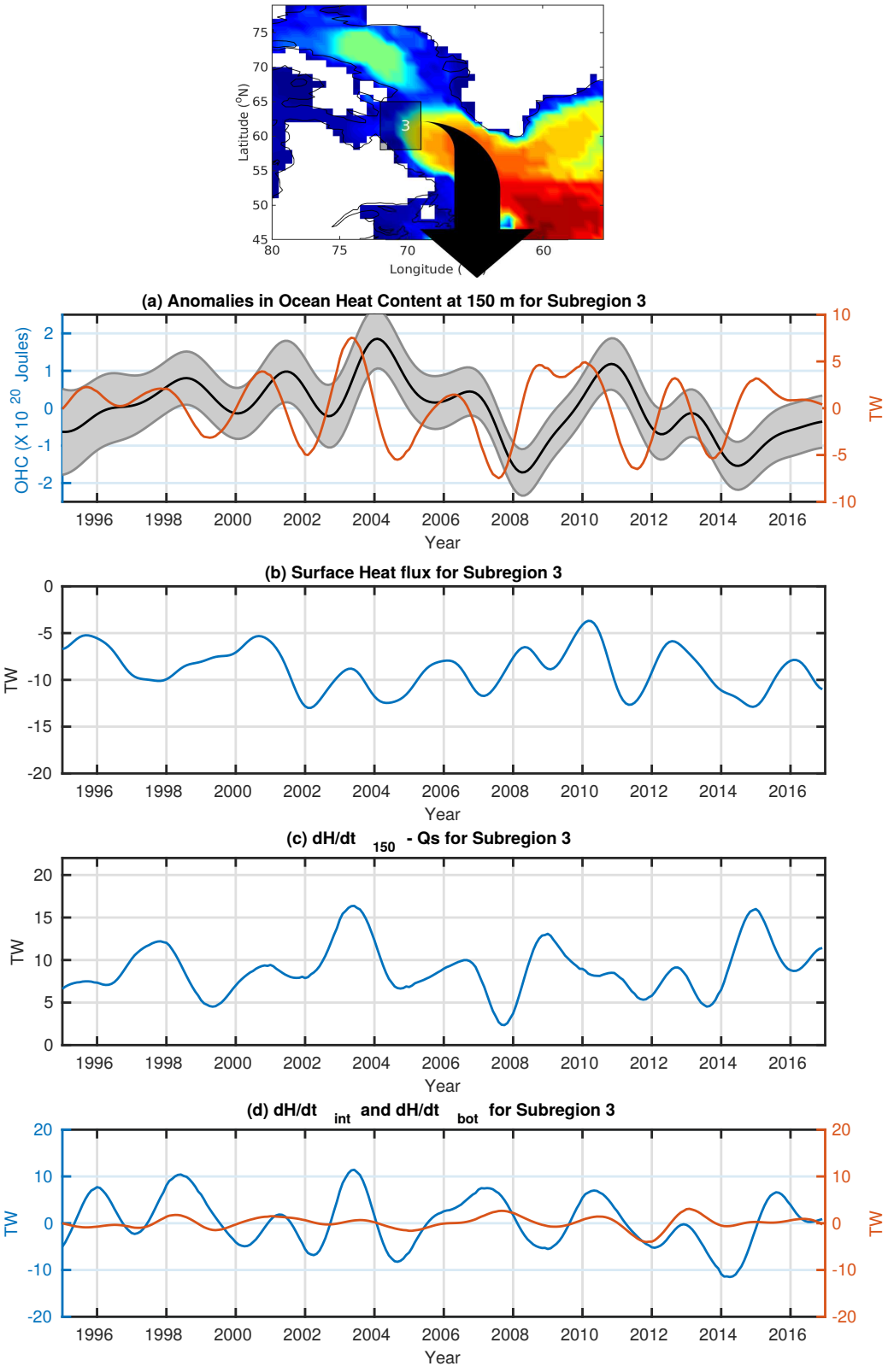

Figure 4.4: Same as Figure 4.2, but for the subregion three.

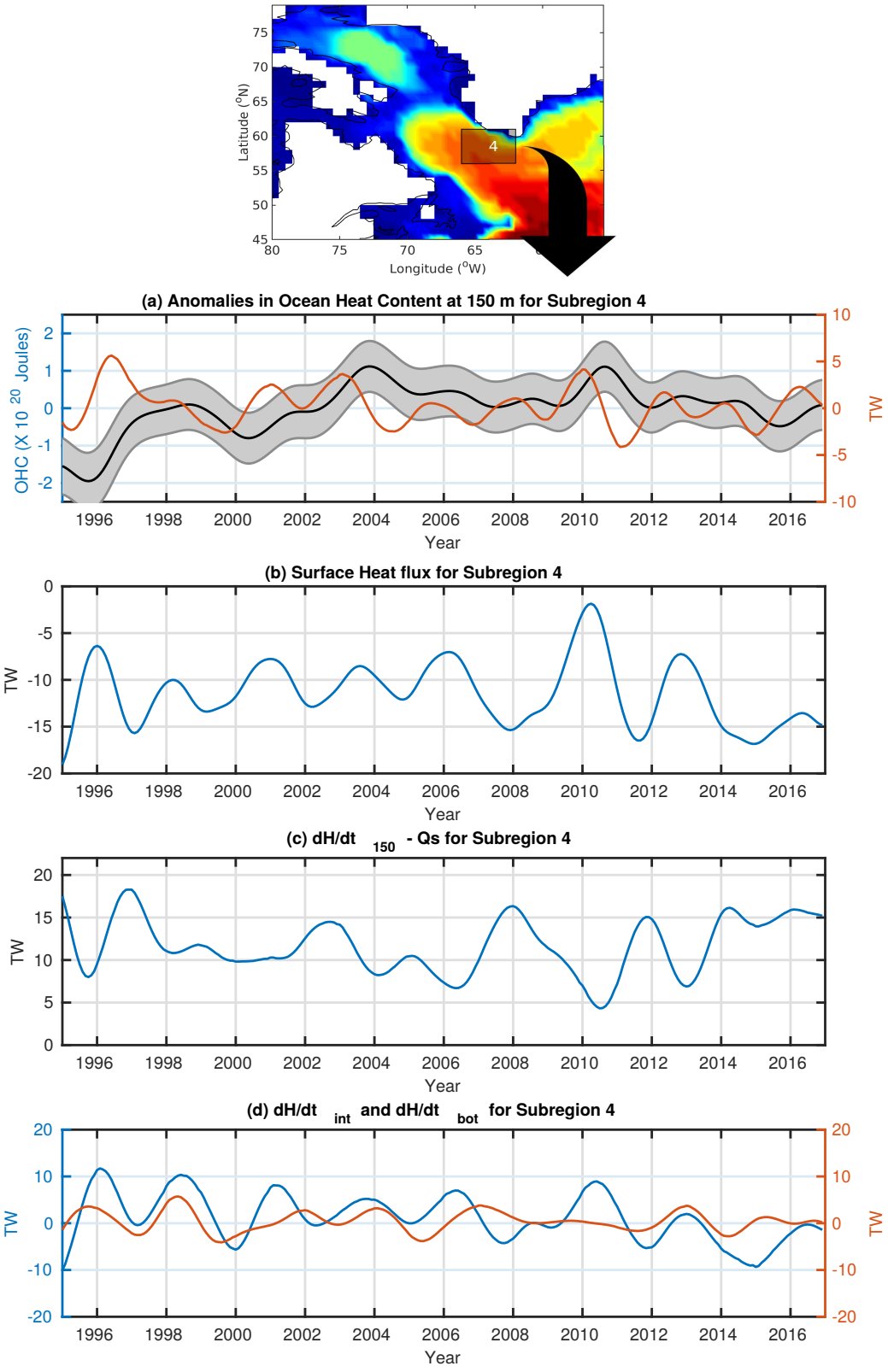

Figure 4.5: Same as Figure 4.2, but for the subregion four.

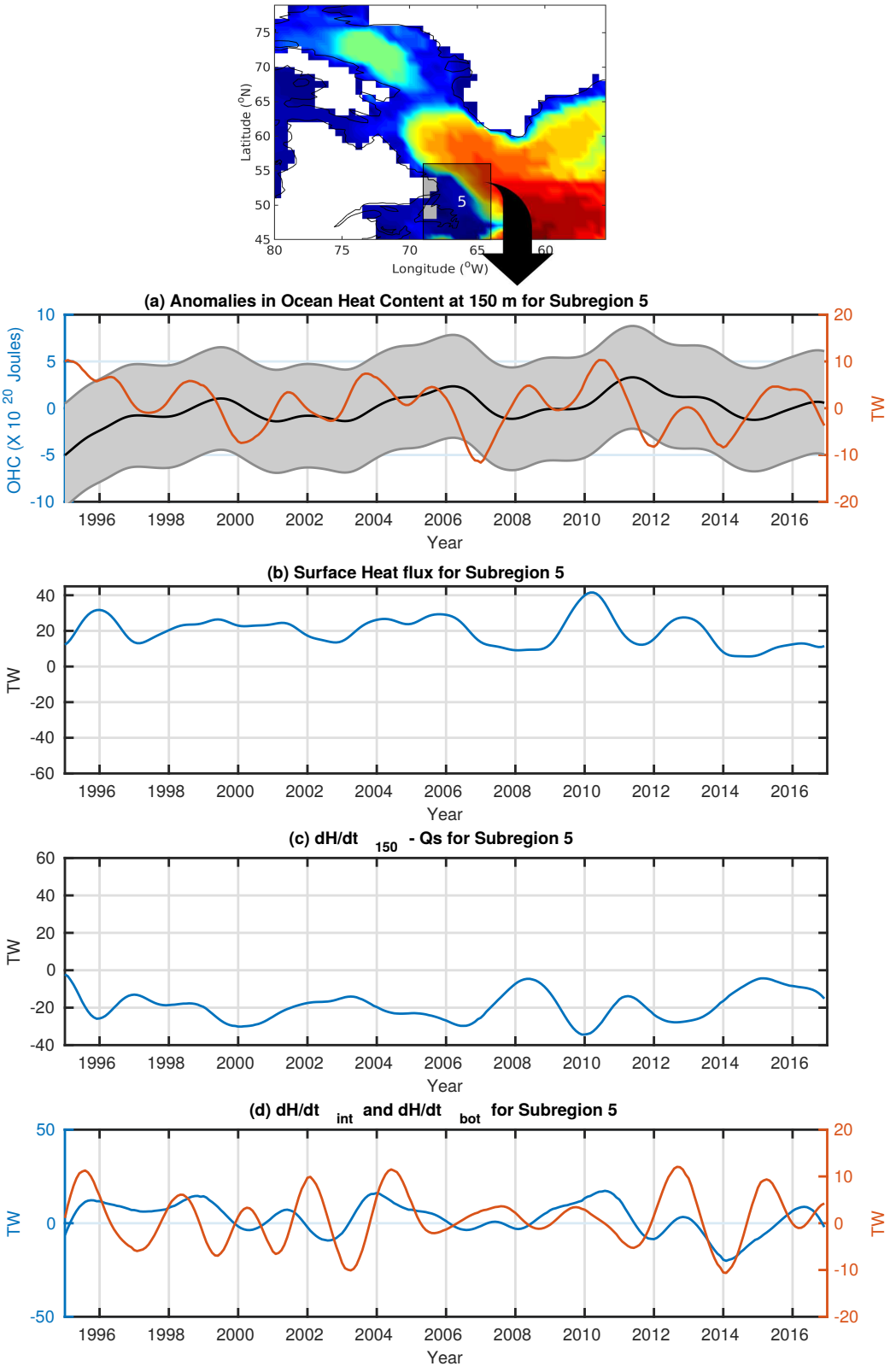

Figure 4.6: Same as Figure 4.2, but for the subregion five.

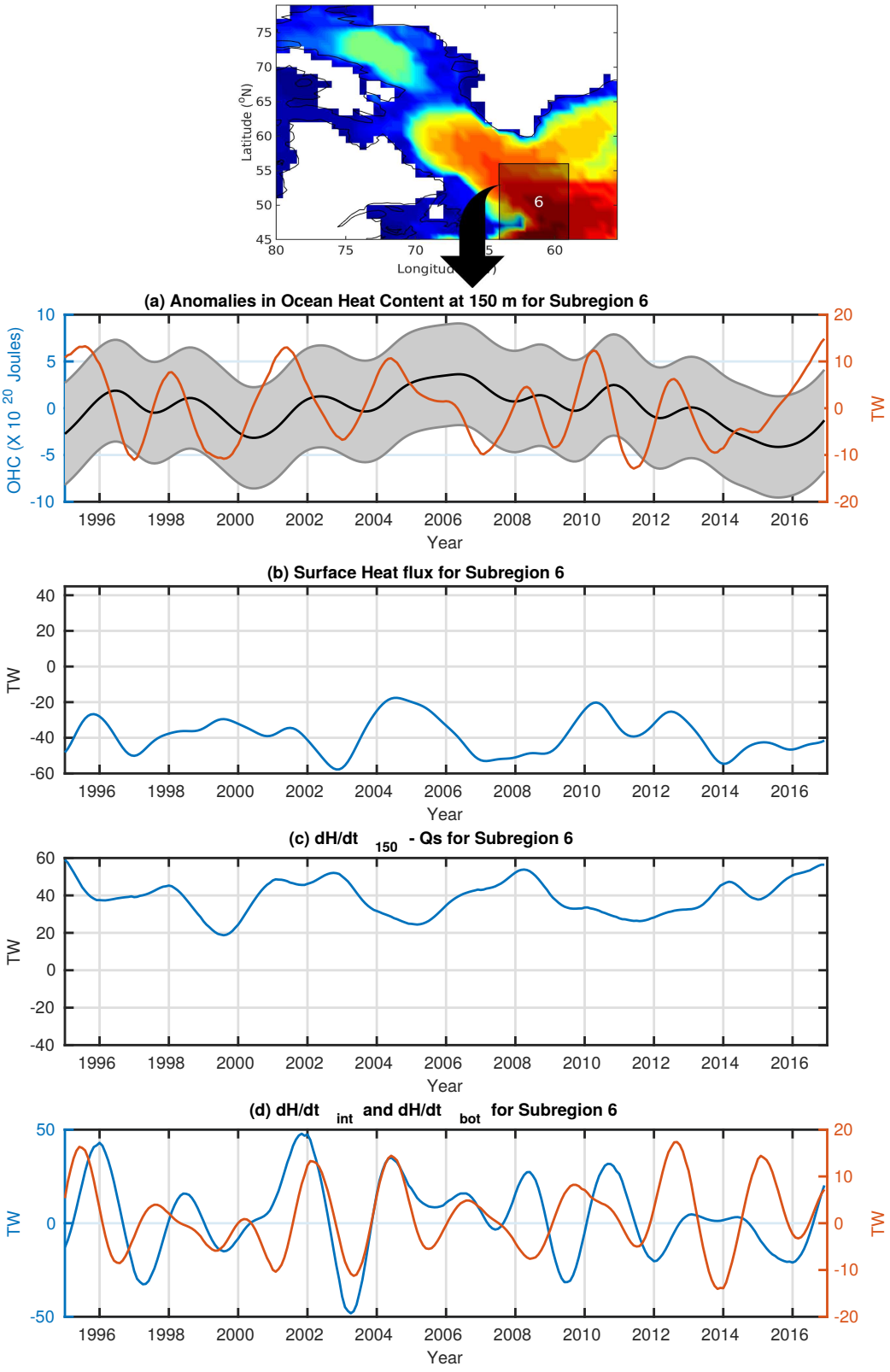

Figure 4.7: Same as Figure 4.2, but for the subregion six.

The heat flux convergence in the intermediate layer does not show significant trends in all six regions. The variability of heat flux convergence in these regions shows oscillations instead of periods of about three years. In the subregions one, two and three, these oscillations are sustained and persistent during the whole period of study (Figures 4.2d-4.4d). In the other three regions, four, five and six, these oscillations have variable amplitude and amplify during some of the periods while decaying in others.

Figure 4.8 shows the total ocean heat content anomalies and its tendency calculated using equations 2.4 for all the six regions. All the six regions show an overall increasing trend from the year 1995 to 2011, followed by cooling from 2011 to 2017. On the other hand, total heat content tendency exhibit frequency of 2-3 years varying between -10 TW to 10 TW for subregion 1-4, -26 TW to 26 TW for the subregion five and -65 TW to 65 TW for the subregion six. Please note, just like figures 4.2-4.7, the limits of the axes on Figure 4.8 were chosen to have a different range for the subregion 1-4 than 5-6.

The total ocean heat transport convergence for the entire ocean column (surface to bottom) is calculated using equation 2.3. Vertical advection terms cancel out when heat transport convergence is integrated for the whole water column. Thus, C_{tot} provides estimates of net contribution of only horizontal advection. The values of C_{tot} is a sum of the heat flux convergence in the surface (Figures 4.2c-4.7c), intermediate (blue curves on Figures 4.2d-4.7d), and bottom (orange curves in Figures 4.2d-4.7d) layers. As mentioned in the previous section, the values of heat flux convergence in the bottom layer are normally an order of magnitude smaller than the heat flux convergence in the other two layers. Therefore, the variability of total heat flux

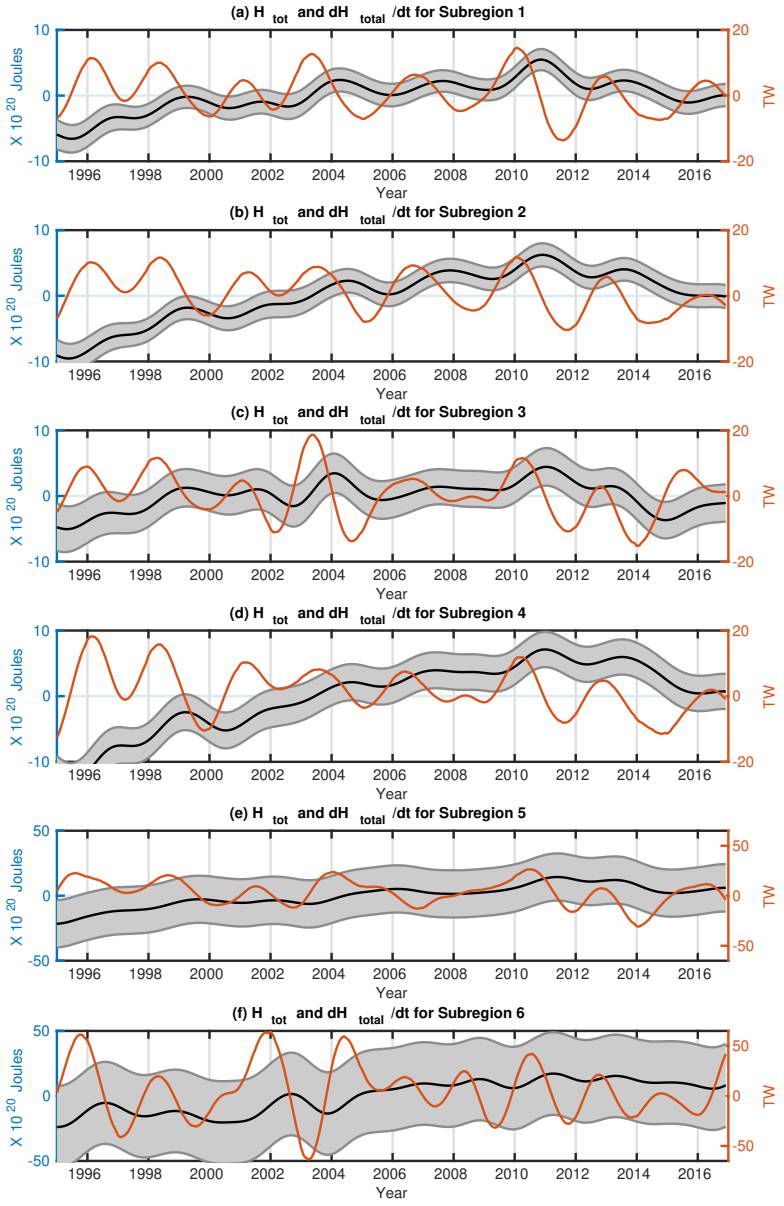

Figure 4.8: Interannual anomalies of Total Ocean Heat Content (H_{tot}) (black) and heat content tendency ($\partial H_{tot}/\partial t$) (orange) for the total ocean column for subregion 1-6 in (a)-(f) respectively for the period 1995-2017.

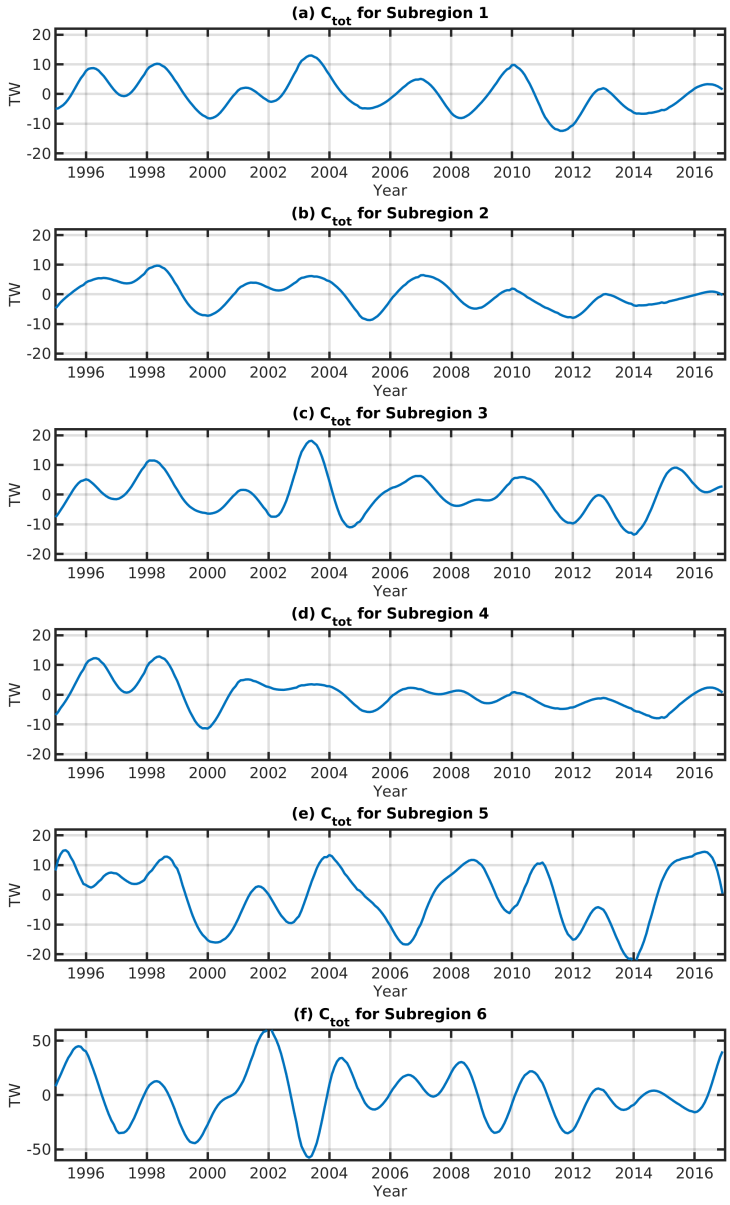

Figure 4.9: Estimated heat transport convergence (C_{tot}) for the total ocean column for subregion 1-6 in (a)-(f) respectively for the period 1995-2017.

convergence in Figure 4.9 represents mostly the impact of heat transport in the surface and intermediate layers on the heat budget of all the six subregions. For Central Labrador Sea illustrated in the panel (b), similar to the surface layer, it shows an increasing trend of heat advection from the year 1995 to 1998 and minima observed in 2000, 2005, and 2012 with a frequency of every 5-6 years. Similar patterns are observed in subregion one illustrated in panel (a), where instabilities of Western Greenland Current and Irminger rings feed the Central Labrador Sea.

The subregions three, four and five show a decreasing trend from 2009 to 2014, which is consistent with the observed weakening of Atlantic Ocean Overturning Circulation by Caeser et al. (2018). North Atlantic Current in the subregion six shown in panel (f) show decreasing trend from 1995 to 2000, which increases for the next two years, but then oscillating negative anomalies are seen all the way to 2012 when it recovers and shows an increased heat transport again which is consistent with findings of Caeser et al. (2018).

4.3 Interannual variability of Heat Budget Component

The magnitude of the interannual variability of the heat budget components for the surface layer is calculated as the variance of low-pass Butterworth filtered monthly estimates of the surface heat flux (Q_s) with a frequency cutoff of $f_c = 1year^{-1}$, heat content tendencies ($\frac{\partial H}{\partial t}$) and heat transport convergence (C_{150}). The strongest heat flux is normally observed in the winter seasons when the temperature difference

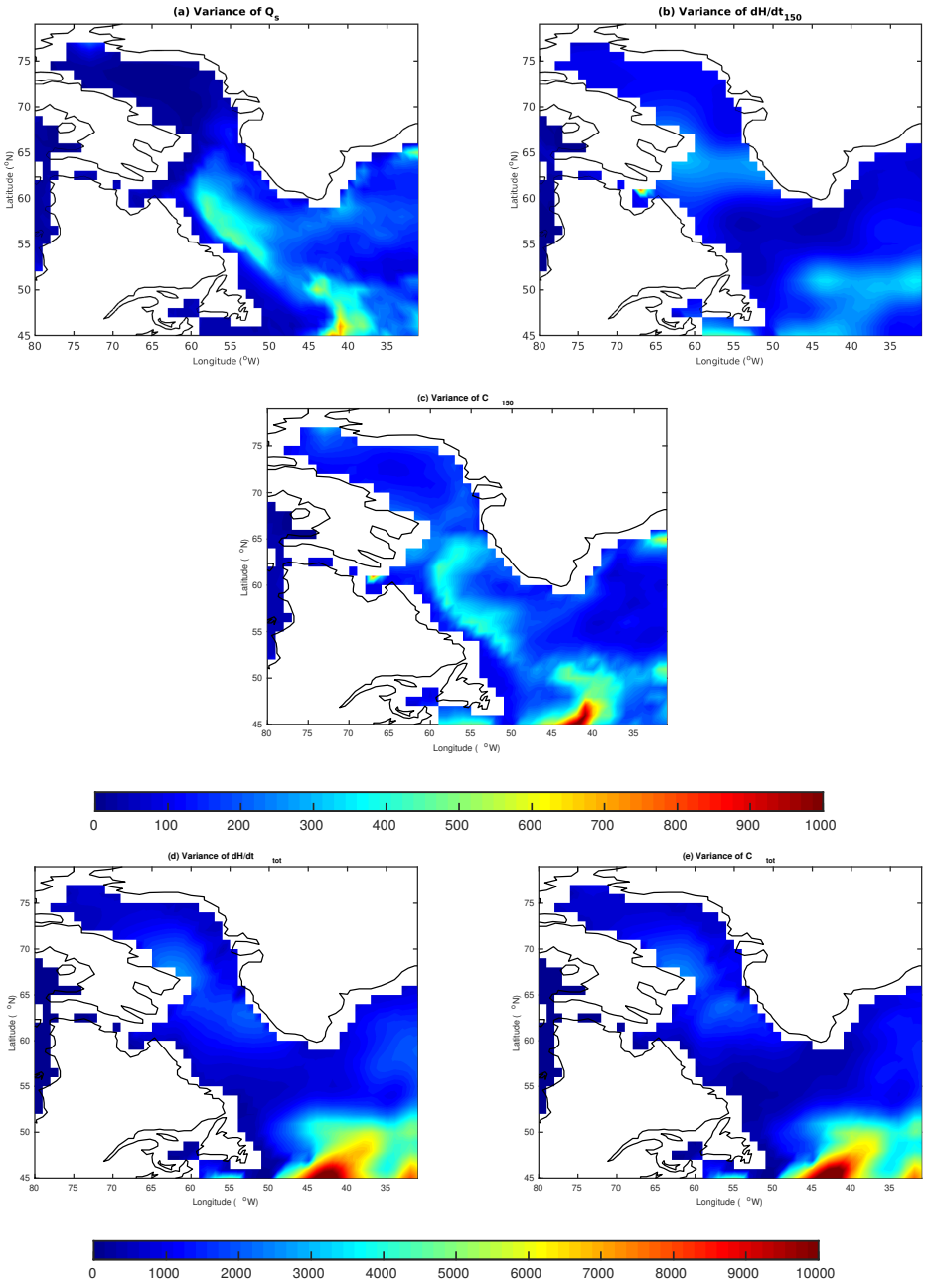

Figure 4.10: Variance of each component of the interannual heat budget in (a) Net surface heat flux, (b) heat content tendencies for surface layer, (c) heat transport convergence in the surface layer, (d) heat content tendencies for total ocean column and (e) heat transport convergence in total ocean column for the period 1993-2018 (W^2/m^4).

and wind speed at the ocean surface have high magnitudes. The variations in the surface heat flux are related mainly to the year-to-year changes in the near-surface atmospheric characteristics in the winter season. These changes occur due to the variability in the frequency, strength, and path of the major storms. The largest magnitude of variations in net surface flux occurs in the central Labrador Sea region (two) with values of 400 W^2/m^4 and in the Gulf Stream region (six) with values of 700 W^2/m^4 (See figure 4.10a). Large quantities of heat are exchanged in both the regions, through deep convection of the Labrador Sea and the warm nature of Gulfstream. Comparison with Figure 3.3 demonstrates that the largest variability in strong surface loss of heat occurs during the winter in the central Labrador Sea. The related buoyancy flux drives the processes of deep convection and the formation of the LSW. Therefore, one part of the heat flux at the surface is converted into the mechanical energy of turbulence mixing, which drives the deep convection. The second part of the surface heat loss in the central Labrador Sea contributes to the tendency of heat content in the surface and intermediate layers. We observe that the variance of surface air-sea heat flux has relatively low variance in the South Labrador Sea (subregion five).

The contribution of the variance of the heat flux convergence (Figure 4.10c) accounts for the interannual variability of the advective heat transport. The combined effect of contributions of surface fluxes and heat transport convergence affects the variability of heat content tendencies. The variance of the tendency of the heat content in the Davis Strait and Gulfstream region is about 300 W^2/m^4. The variance of surface layer heat content tendency in the rest of the Labrador Sea is below 200 W^2/m^4. The magnitudes and the spatial patterns of the variance of surface net heat

flux (Q_s) and convergence of heat transport (C_{150}) (see Figure 4.10) is similar. This similarity suggests that the interannual variability of ocean transport approximately balances the year-to-year changes in the surface heat flux.

4.4 Drivers of Interannual Heat Content Variability

The correlations between the components of the heat budget are shown in Figure 4.11. The heat flux correlates well ($r \geq 0.5$) in the central Labrador Sea and Irminger Sea (Figure 4.11a). These are areas of intense surface heat exchange and deep convection. Significantly higher is the correlation between the heat flux convergence and the tendency of heat content in the Labrador Current. The intensified heat flux convergence in this region has a dominant contribution to the variations of the heat tendency (Figure 4b). The low and negative heat flux convergence causes a strong cooling in these waters. The heat flux convergence in the central Labrador basin is poorly correlated with the tendency of heat content.

Figures 4.11b,d show the correlation between heat content tendency in the total ocean column with net surface fluxes and heat transport convergence in the total ocean column. Other than the Central Labrador Sea, heat content tendency is strongly correlated with heat transport convergence for the entire western subpolar North Atlantic region. The convergence of heat transport is a dominant factor in the total ocean heat content budget for most of the region. The heat budget in the areas of intense convection in the central Labrador Sea and Irminger Sea depends

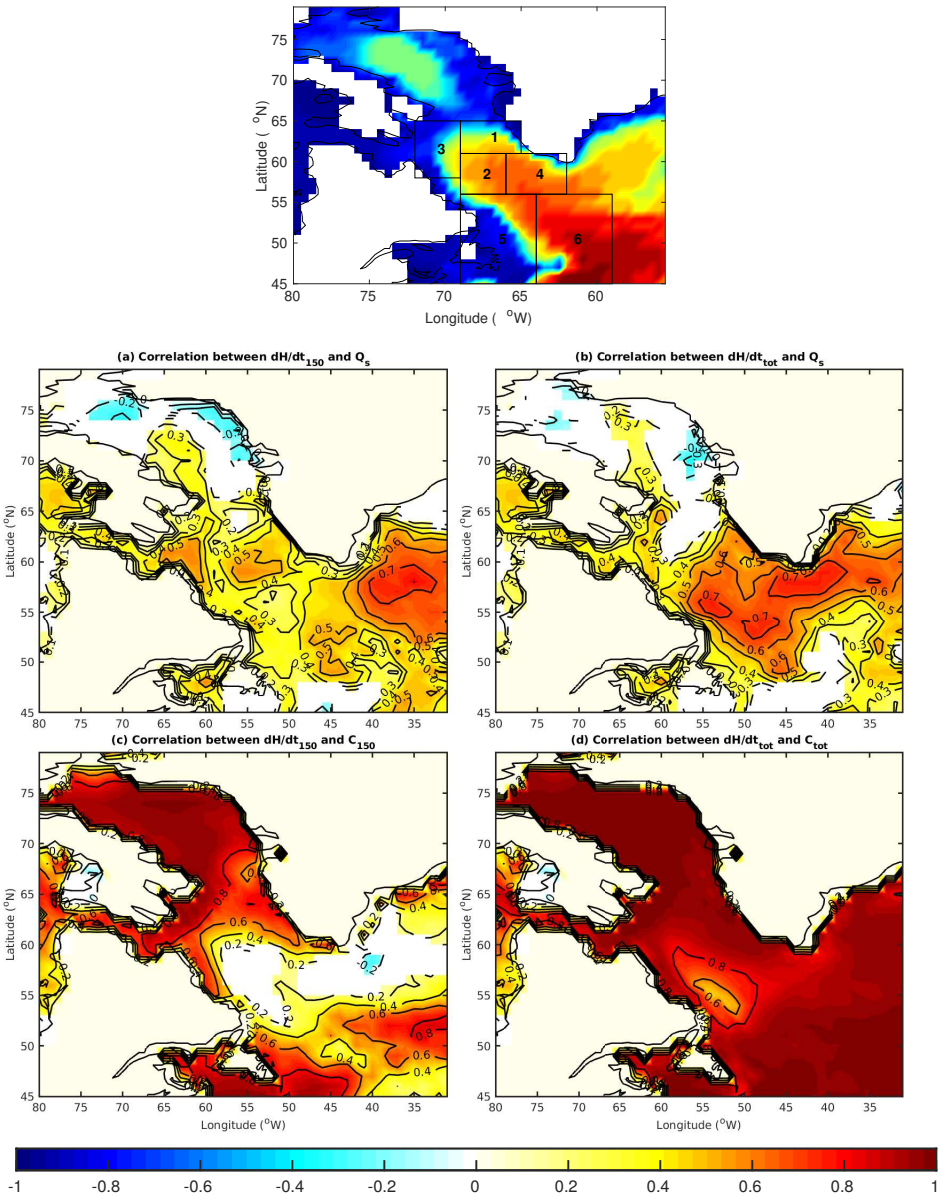

Figure 4.11: Correlations between different components of the interannual heat budget (a) surface heat content tendency and net surface heat flux, (b) heat content tendency for total ocean column and net surface heat flux, (c) surface heat content tendency and heat transport convergence in the surface layer, and (d) heat content tendency for total ocean column and total heat transport convergence for the period of 1993-2018. The map above, which shows the mean total heat content for the period 1993-2018, highlights the regions of interest.

r	Region 1	Region 2	Region 3	Region 4	Region 5	Region 6
Region 1	1	0.438	0.583	0.225	0.148	0.248
Region 2	0.438	1	0.317	0.828	0.710	0.600
Region 3	0.583	0.317	1	-0.014	0.272	0.258
Region 4	0.225	0.828	-0.014	1	0.694	0.614
Region 5	0.148	0.710	0.272	0.694	1	0.649
Region 6	0.248	0.600	0.258	0.614	0.649	1

Table 4.1: Pairwise cross-correlation for ocean heat transport convergence between all the regions for the Surface Layer for the period 1993-2018.

significantly on surface heat flux. When separating the factors contributing to the heat budget into surface flux and horizontal heat convergence, we need to consider that the horizontal transport is not completely independent of the surface forcing. In fact, the ocean currents and transport are partly driven by surface winds (Ekman transport) and density gradients generated by the vertical mixing and convection in Irminger and central Labrador Seas.

To investigate how the heat transport convergence in different regions are interrelated, the cross-correlations between respective heat transport convergence values were calculated and have been presented pairwise in Table 4.1 for the Surface Layer and Table 4.2 for Total Ocean Column. On close examination, heat transport convergence in the surface layer for the Central Labrador Sea (subregion 2) has good positive correlations with the other subregions, viz., subregions 4, 5 and 6. It is highly correlated with the subregion 4, with a correlation coefficient of 0.828 at 95%

r	Region 1	Region 2	Region 3	Region 4	Region 5	Region 6
Region 1	1	0.811	0.760	0.713	0.272	0.020
Region 2	0.811	1	0.676	0.876	0.440	0.234
Region 3	0.760	0.676	1	0.559	0.372	-0.050
Region 4	0.713	0.876	0.559	1	0.517	0.363
Region 5	0.272	0.440	0.372	0.517	1	0.262
Region 6	0.020	0.234	-0.050	0.363	0.262	1

Table 4.2: Pairwise cross-correlation for ocean heat transport convergence between all the regions for the Total Ocean Column for the period 1993-2018.

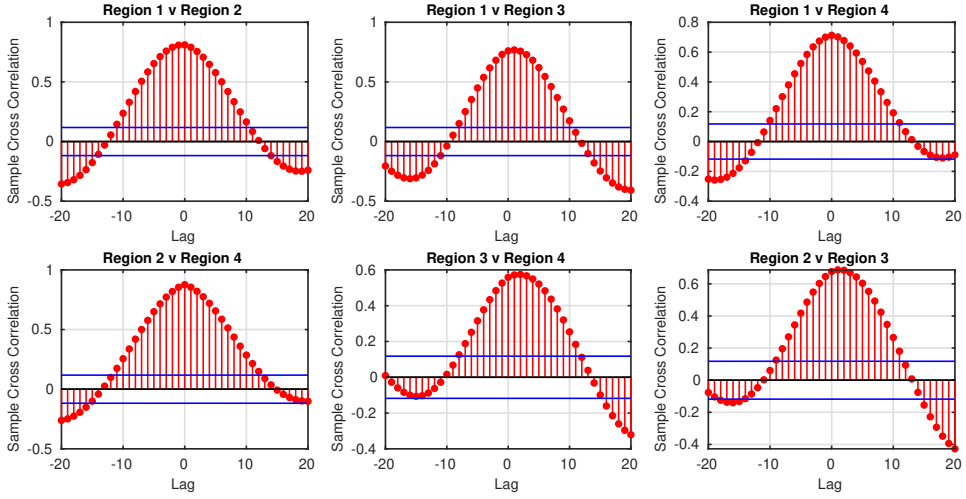

Figure 4.12: Cross-correlation of total ocean column heat transport convergence term between the regions with ($r > 0.7$) with 95% confidence. The lags are in months.

confidence, as seen in Table 4.1.

For the total ocean column, while heat transport in subregion one is strongly correlated with subregion 2,3 and 4 with correlation coefficient in excess of 0.7, subregion five does not have a good correlation with other subregions signifying the dominance of regional ocean dynamics. Since subregion 4 and 5 both receive water from spreading of LSW, a correlation of 0.51 among them signify the importance of regional dynamics.

Figure 4.12 shows the correlation coefficient changes with time lag for highly correlated regions. There is a lag of two months between subregion 1-3 and subregion 2-3, and lag of up to three months between subregion 3 and 4. No lag is observed in subregion 1-4 and 2-4

To understand the origin of the interannual variability, we look at the drivers of ocean heat content in both surface layer and total ocean column by identifying the regions where correlations are significant. Figure 4.13 (a) and (b) show the correlation between surface ocean content and net surface heat flux and just turbulent flux, respectively. The radiative flux has little impact on the Ocean Heat Content variability. The most significant correlations between the surface heat flux and heat flux convergence in the surface layer is observed over the Grand banks region off the Newfoundland coast and Southwest of Greenland. These are the two regions where turbulent fluxes play an essential role in driving the heat content variability.

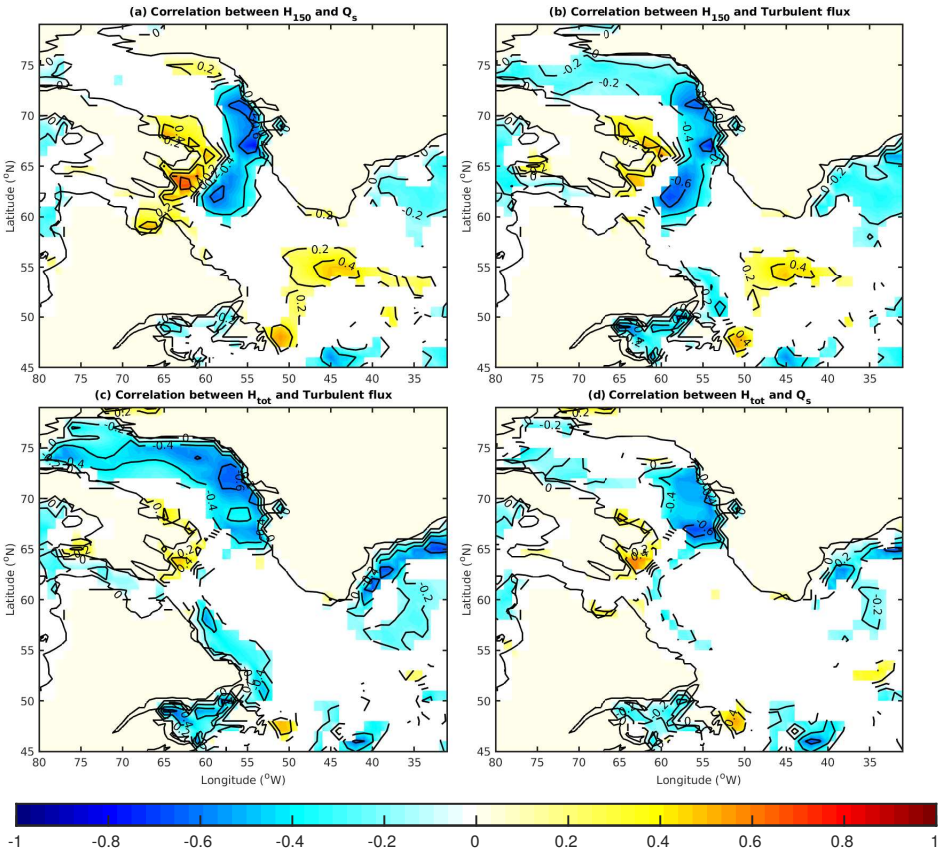

Figure 4.13: Correlations between estimates of deseasonalized and 12-month low-pass filter smoothed Heat Content in the surface layer and total ocean column with the deseasonalized and smoothed net surface heat flux and turbulent flux components (latent heat flux and sensible heat flux) for the period of 1993-2018.

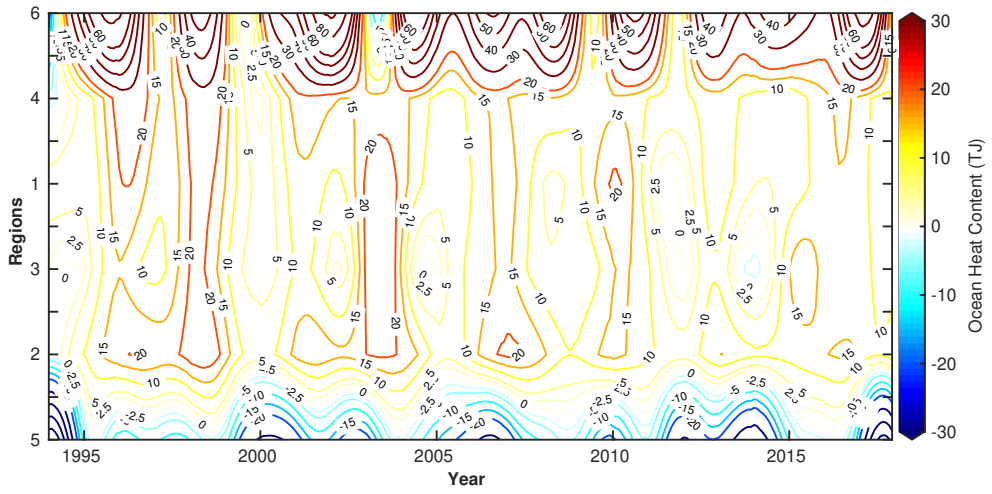

Figure 4.14: Region-time (Hovmöller) diagram of monthly heat flux convergence anomalies for total ocean column for the period 1994-2017. A wavelike pattern is observed for the total ocean heat content tendency from subregion 6 to 5.

4.5 Ocean Heat Transport Convergence as a driver

Figure 4.14 shows the time variations (Hovmöller diagram) of total heat flux convergence in the six regions. The regions are sorted along axis y of these figures in a way that approximately follows the direction of the flow in the sub-polar gyre. On the top of this axis is (i) region six over the North Atlantic Current, then (ii) region four over the East Labrador Sea, (iii) region one over the Northeast Labrador Sea, (iv) region three over the northwest Labrador Sea, (v) region two over the central Labrador Sea and (vi) region five over the Newfoundland basin. The time variations of monthly net surface heat flux and heat content tendency for total ocean column for all the six regions are shown in figure 4.15 (a) and (b), respectively. The heat flux convergence in the South Labrador Sea subregion five is negative during most of the time (see

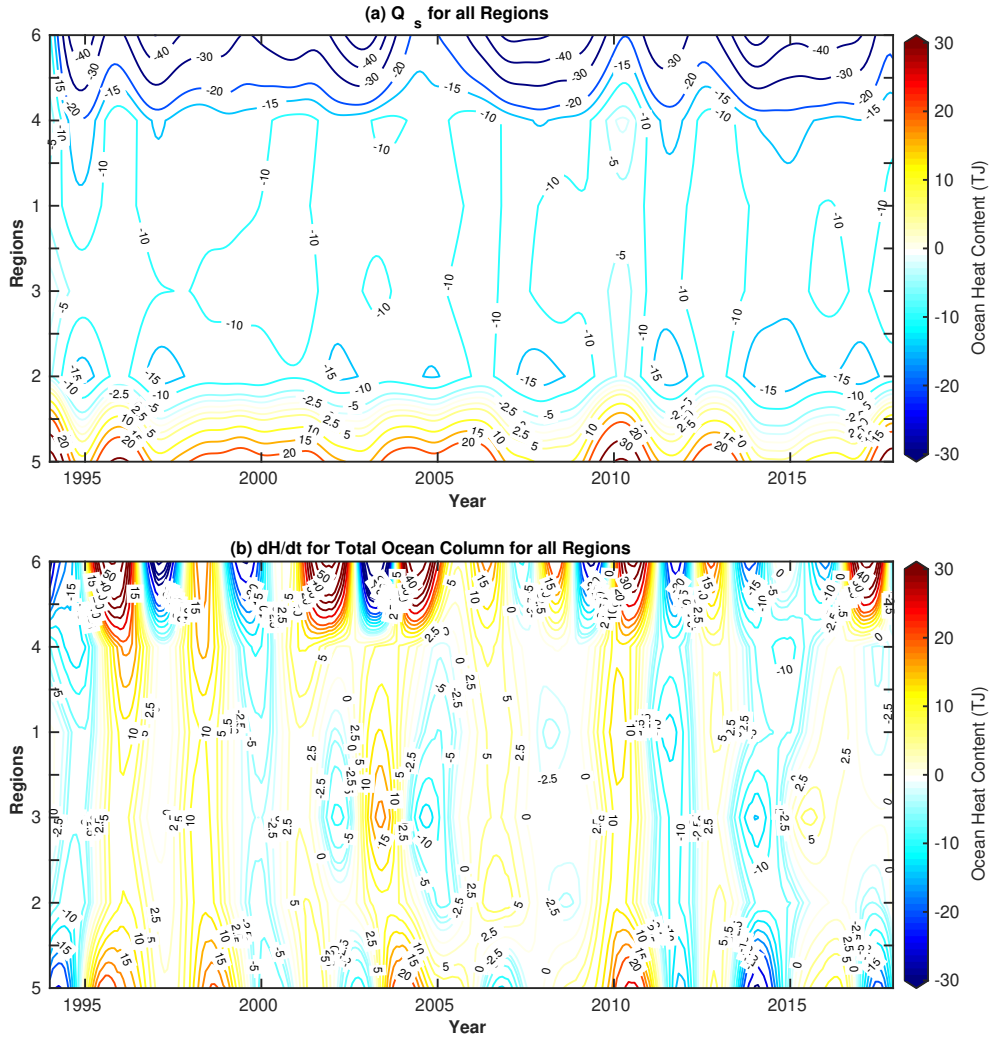

Figure 4.15: Region-time (Hovmöller) diagram of monthly (a) net surface heat flux anomalies and (b) heat content tendency for total ocean column for the period 1994-2017. A wavelike pattern is observed for the total ocean heat content tendency from subregion 6 to 5.

figure 4.14); however, it is influenced in the years with very high positive anomalies as seen for the years 1996-1998, 2004 and 2008. While net surface heat fluxes do not show such wavelike patterns in Figure 4.15 (a), panel (b) clearly indicates this

horizontal advection is the driving force of positive heat content tendencies.

To investigate how heat transport convergence in all the subregions appears at different layers, we look at figure 4.16 that shows monthly heat transport convergence anomalies for (a) surface, (b) intermediate and (c) bottom layers for all regions using a Hovmöller diagram. The intermediate layer, i.e., between 150 and 2000 m, shows dominantly the same pattern as seen in Figure 4.15 (b), which indicates these similar heat tendencies in all subregions could be a result of advection between the regions that leads to heat content anomalies through interacting water masses of North Atlantic Circulation. However, the high negative values for the heat advection in the subregion five (Figure 4.14) are largely seem to be derived from the surface layer. It must be noted that the Newfoundland shelf, which forms the most of subregion five, is only 180-500 m deep. The grid points included in the selection for this region, in the deeper layers, reflect north of Newfoundland shelf that is deep as 3500 m. We cant discount the contribution of surface fluxes and air-sea exchange in this region.

Furthermore, we observe a distinct difference in frequency in heat advection between the regions for all the layers. The intermediate layer has a higher frequency of such concurrent heat tendencies among all regions, which further increases for the deep layer. The magnitude, however, is highest for the surface layer, and reduces by an order of magnitude for deeper layers.

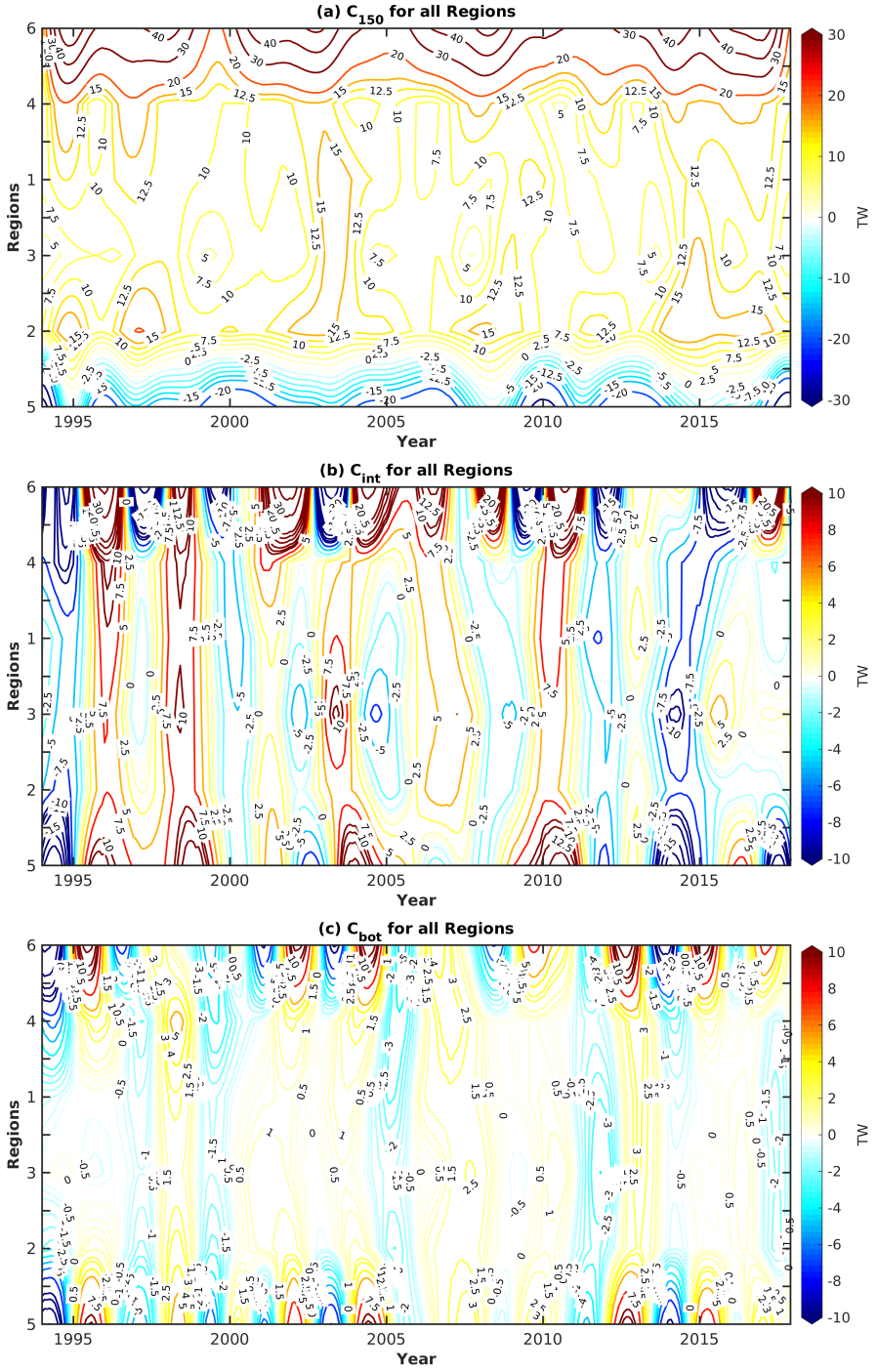

Figure 4.16: Region-time (Hovmöller) diagram of monthly heat transport convergence anomalies for (a) surface, (b) intermediate and (c) bottom layers for the total ocean for the year 1994-2017.

Chapter 5

Conclusions and Discussions

The main goal of this thesis is to understand the dominant patterns of interannual variability of the ocean heat content in the Labrador Sea and the contribution of the ocean transport of heat to the variability. This chapter summarizes the main results of this dissertation and presents recommendations for future work.

5.1 Conclusions

The thesis presents results from an observation-based analysis of interannual and decadal variability of the heat budget in the Labrador Sea. The data used in the study include monthly mean gridded ARGO observations of the vertical temperature profiles in the Labrador Sea. The surface fluxes of heat at the air-sea surface are derived from the ERA5 ECMWF reanalysis. We studied the driving mechanism of the interannual variations in ocean heat content, which include surface flux and ocean advection of heat. The net surface heat fluxes are calculated as a sum of radiative heat fluxes (net shortwave and net longwave heat flux) and turbulent heat fluxes

(sensible heat flux and latent heat flux). The seasonal cycle was removed from the temperature and surface heat flux data by using a low-pass Butterworth filter with a cutoff frequency of $f_{cutoff} = \frac{1}{year}$. We apply the method of Roberts et al., 2017 for estimation of heat content tendency and convergence of heat transport in six subregions of the Western Subpolar North Atlantic.

Interannual variations in ocean heat content are explained by the contributions of net surface heat flux and the advection of heat through ocean transport. The ocean heat transport is a crucial component of the total ocean heat budget. The heat flux convergence in the surface layer of all regions is positive, partly balancing the annual mean surface heat flux. Negative heat advection was observed over the South Labrador Sea region, which is largely over Newfoundland shelf partly balanced by the high positive values for surface heat fluxes. During early spring, sea ice drifts along the coast of Labrador and Newfoundland. This sea ice melts during the spring and renders negative temperature anomalies and negative heat advection in the surface layer.

The magnitude of heat flux convergence in the subregion five and also six (North Atlantic Current region), was estimated to be about twice as high as the heat flux convergence in the all of the regions. While total heat flux convergence in all the four subregions, viz., one, two, three and four, were observed to be strongly correlated, subregions five and six were not correlated with other regions or among each other despite being on same latitudes.

The dynamics of the surface layer strongly influence the variability in the total heat convergence. The heat advection in the Labrador Sea and its interannual variability strongly depend on the dynamics of the boundary currents, which is responsible for

heat redistribution in the entire subpolar North Atlantic region. Other than the Central Labrador Sea, where deep convection dominates, the contribution of heat transport convergence significantly dominates interannual variations in the ocean heat content tendencies, which is largely controlled by the transport of heat within the ocean rather than the loss or addition of heat at the surface.

The region of North Atlantic Current (subregion six) and South Labrador Sea over Newfoundland shelf (subregion five) exhibit strong spatial and temporal variability. This causes high uncertainty in the estimates of the area mean heat content and demands the need for more observations to understand the heat budget.

Based on these results, we conclude that surface heat balance alone can not explain the ocean heat content anomalies in both the surface layer and the total ocean column. Ocean dynamics play a critical role in the generation of ocean heat content anomalies through the transport by main currents and eddies.

5.2 Future Work

Our results highlight the importance of surface heat fluxes and regional ocean dynamics, leading to heat transport convergence in the predictability of the state of ocean heat content and its tendency on interannual time scales in the surface layer and total ocean column. The observations by the ocean profiling moorings, Argo floats, ships and CTD profilers, etc. are still limited to the upper 2000 m. They do not provide sufficient information for the abyssal ocean. The limited observations available along Newfoundland shelf and North Atlantic Current region using Argo floats were other fundamental limitations we encountered. The gridded Met Office temperature data

have high uncertainties in these regions. The results from this study demonstrate that further improvement of the ocean observing system in these regions is of high priority for a better understanding of the Labrador Sea climate.

In the context of this study, additional knowledge is needed about the atmosphere-ocean-ice interaction in the presence of seasonal sea ice that melts in spring and renders negative anomalies in surface heat and salt content of the ocean. The sea-ice drifted along Labrador interacts with regional ocean dynamics, and these processes happen at a much finer scale. Combining in-situ data with remote observations like sea surface height altimetry, surface winds, sea-surface temperature, and ocean colour is essential for understanding the underlying processes at meso- or submeso- spatial scale. High resolution regional coupled ocean-atmosphere models can extend further our knowledge about the heat transport in the Labrador Sea.

Bibliography

Bryden, H.L., Longworth, H.R., Cunningham, S.A.,(2005): *Slowing of the Atlantic meridional overturning circulation at 25°N*. Nature, 438:655657.

Caesar, L., Rahmstorf, S., Robinson, A. et al.,(2018): *Observed fingerprint of a weakening Atlantic Ocean overturning circulation.* Nature 556, 191196. https://doi.org/10.1038/s4 018-0006-5

Cayan, D.R., (1992): *Latent and Sensible Heat Flux Anomalies over the Northern Oceans: Driving the Sea Surface Temperature.* J. Phys. Oceanogr., 22, 859881

Copernicus Climate Change Service (C3S) (2017): *ERA5: Fifth generation of ECMWF atmospheric reanalyses of the global climate.* Copernicus Climate Change Service Climate Data Store (CDS), Date of access: December 6, 2019. https://cds.climate.copernic

Costello, M.J.,Cheung, A. ,De Hauwere, N., (2010): *Topography statistics for the surface and seabed area, volume, depth and slope, of the worlds seas, oceans and countries*, Environ. Sci. Technol., 44, pp. 8821-8828

Cunningham, S.A. and Marsh, R. (2010): *Observing and modeling changes in the Atlantic MOC.* WIREs Clim Chg, 1: 180-191. doi:10.1002/wcc.22

Dickson R., Lazier J., Meincke J., Rhines P. (1996): *Long-Term Coordinated Changes in the Convective Activity of the North Atlantic.* In: Anderson D.L.T., Willebrand J. (eds) Decadal Climate Variability. NATO ASI Series (Series I: Global Environmental Change), vol 44. Springer, Berlin, Heidelberg

Drinkwater, K. F. (1988): *On the mean and tidal currents in Hudson Strait.* Atm.-Ocean 26: 252-266

Emery, W.J., Meincke, J., (1986): *Global water masses: summary and review.* Oceanologica Acta Vol 9, No. 4

Garca-Ibez, M. I., Prez, F. F., Lherminier, P., Zunino, P., Mercier, H., and Trguer, P., (2018): *Water mass distributions and transports for the 2014 GEOVIDE cruise in the North Atlantic.* Biogeosciences, 15, 20752090, https://doi.org/10.5194/bg-15-2075-2018.

Gascard, J.-C., Clarke, R.A., (1983): *The formation of Labrador Sea water. Part II: Mesoscale and smaller-scale processes.* Journal of Physical Oceanography 13 (10), P1780P1797.

Good, S. A., (2011): *Depth biases in XBT data diagnosed using bathymetry data.* J. Atmos. Oceanic Technol., 28, 287300.

Good, S. A., Martin, M. J., and Rayner, N. A., (2013): *EN4: Quality controlled ocean temperature and salinity profiles and monthly objective analyses with uncertainty estimates*, J. Geophys. Res. Oceans, 118, 6704 6716, doi:10.1002/2013JC009067.

Gouretski, V. (2012): *Using GEBCO digital bathymetry to infer depth biases in the*

XBT data. Deep Sea Res. 62, 4052. doi: 10.1016/j.dsr.2011.12.012

Gouretski, V., and Reseghetti, F. (2010): *On depth and temperature biases in bathythermograph data: Development of a new correction scheme based on analysis of a global ocean database.* Deep Sea Res. 57, 812833. doi: 10.1016/j.dsr.2010.03.011

Greatbatch, R.J., Goulding, A., (1989): *Seasonal variations in a linear barotropic model of the North Atlantic driven by the Hellerman and Rosenstein wind stress field.* J. Phys. Oceanogr., 19 , pp. 572-595

Hamon, Mathieu, Reverfdin, Gilles, Traon, Pierre-Yves. (2012): Empirical Correction of XBT Data. Journal of Atmospheric and Oceanic Technology. 29. 960-973. 10.1175/JTECH-D-11-00129.1.

Ishii, M., and M. Kimoto, (2009): *Reevaluation of historical ocean heat content variations with time-varying XBT and MBT depth bias corrections.* J. Oceanogr., 65, 287299, doi:10.1007/s10872-009-0027-7.

Johns, W.E., M.O. Baringer, L.M. Beal, S.A. Cunningham, T. Kanzow, H.L. Bryden, J.J. Hirschi, J. Marotzke, C.S. Meinen, B. Shaw, and R. Curry, (2011): *Continuous, Array-Based Estimates of Atlantic Ocean Heat Transport at 26.5N.* J. Climate, 24, 24292449, https://doi.org/10.1175/2010JCLI3997.1

Kanzow, T., and Coauthors. (2010): *Seasonal variability of the Atlantic meridional overturning circulation at 26.58N.* J. Climate, 23, 56785698, doi:10.1175/2010JCLI3389.1.

Kieke, D., Igor Yashayaev, (2015): *Studies of Labrador Sea Water formation and variability in the subpolar North Atlantic in the light of international partnership*

and collaboration. Progress in Oceanography, Volume 132, pp. 220-232

Kuhlbrodt, T., Griesel, A., Montoya, M., Levermann, A., Hofmann, M., and Rahmstorf, S., (2007): *On the driving processes of the Atlantic meridional overturning circulation*, Rev. Geophys., 45, RG2001, doi:10.1029/2004RG000166.

Lavender, K., Davis, R., Owens, W., (2000): *Mid-depth recirculation observed in the interior Labrador and Irminger seas by direct velocity measurements*. Nature 407, 6669. https://doi.org/10.1038/35024048

Lazier, J.R.N. (1980): *Oceanographic conditions at Ocean Weather Ship Bravo, 19641974*. Atmosphere-Ocean 18, P227-P238.

Lazier, J., Hendry, R., Clarke, A., Yashayaev, I., Rhines, P. (2002): *Convection and restratification in the Labrador Sea, 1990-2000*. DeepSea Research I 49 (10), P1819P1835.

Lazier,J.R.N., Wright, D.G., (1993): *Annual velocity variations in the Labrador Current*. J. Phys. Oceangr., 23 , pp. 659-678

LeBlond, P., Osborn, T.R., Hodgins, D., Goodman, R., Metge, M. (1981): *Surface circulation in the western Labrador Sea*. Deep Sea Res. 28A: 683-693

Lilly, J. M., P. B. Rhines, F. Schott, K. L. Lavender, J. Lazier, U. Send, and E. D'Asaro (2003): *Observations of the Labrador Sea eddy field*, Progr. Oceanogr., 59, 75176.

Lilly, J. M., P. B. Rhines, M. Visbeck, R. Davis, J. R. N. Lazier, F. Schott, and D. Farmer, (1999): *Observing deep convection in the Labrador Sea during winter*

1994/95. J. Phys. Oceanogr., 29, 20652098.

Loder, J. W., B. Petrie, and G. Gawarkiewicz, (1998): *The coastal ocean off northeastern North America: A largescale view*, in The Sea, vol. 11, edited by A. R. Robinson, and K. H. Brink, pp. 105133, John Wiley, New York.

Marsh, R. (2000): *Recent variability of the North Atlantic thermohaline circulation inferred from surface heat and freshwater fluxes*. J. Climate, 13 (2000), 3239-3260, doi:10.1175/1520-0442013,3239:RVOTNA.2.0.CO;2.

Marshall, J., and Coauthors, (1998): *The Labrador Sea deep convection experiment*. Bull. Amer. Meteor. Soc., 79, 20332058, doi:https://doi.org/10.1175/1520-0477(1998)079.

Marshall, J., Kushnir, Y., Battisti, D., Chang, P., Czaja, A., Dickson, R., Hurrell, J., McCartney, M., Saravanan, R. and Visbeck, M., (2001): *North Atlantic climate variability: phenomena, impacts and mechanisms*. Int. J. Climatol., 21: 1863-1898. doi:10.1002/joc.693

Marshall, J., and F. Schott. (1999): *Open-ocean convection: Observations, theory, and models*. Rev. Geophys., 37, 164, doi:10.1029/98RG02739.

McCartney, M.S., Talley, L.D., (1982): *The subpolar mode water of the North Atlantic Ocean*. Journal of Physical Oceanography 12 (11), P1169P1188.

Mertz G., Narayanan S., Helbig J. (1993): *The freshwater transport of the Labrador Current*. Atmos. Ocean, 31 (2), pp. 281-295

Prinsenberg, S.J., (1988): *Ice-cover and ice-ridge contributions to the freshwater contents of Hudson Bay and Foxe Basin.* Arctic 41 (1), 611.

Rhein, M., and coauthors. (2002): *Labrador Sea Water: Pathways, CFC inventory, and formation rates.* J. Phys. Oceanogr., 32, 648-665, doi:10.1175/1520-0485(2002)032,0648:LSWPCI.2.0.CO;2.

Rhein, M., and coauthors. (2011): *Deep water formation, the subpolar gyre, and the meridional overturning circulation in the sub-polar North Atlantic.* Deep-Sea Res. II, 58, 1819-1832, doi:10.1016/j.dsr2.2010.10.061.

Roberts, C. D., Palmer, M. D., Allan, R. P., Desbruyeres, D. G., Hyder, P., Liu, C., and Smith, D., (2017): *Surface flux and ocean heat transport convergence contributions to seasonal and interannual variations of ocean heat content*, J. Geophys. Res. Oceans,122, 726 744, doi:10.1002/2016JC012278.

Schott, F. A., J. Fischer, M. Dengler, and R. Zantopp. (2006): *Variability of the deep western boundary current east of the Grand Banks.* Geophys. Res. Lett. , 33, L21S07, doi:10.1029/ 2006GL026563.

Talley, L.D., McCartney, M.S. (1982): *Distribution and circulation of Labrador Sea Water.* Journal of Physical Oceanography 12 (11), P1189-P1205.

Trenberth, K., Caron, J., Stepaniak, D. (2001): *The atmospheric energy budget and implications for surface fluxes and ocean heat transports.* Climate Dynamics 17, 259-276. https://doi.org/10.1007/PL00007927

Wijffels, S. E., J. Willis, C. M. Domingues, P. Barker, N. J. White, A. Gronell, K.

Ridgway, and J. A. Church, (2008): *Changing expendable bathythermograph fall rates and their impact on estimates of thermosteric sea level rise.* J. Climate, 21, 56575672.

Yashayaev, I. (2007): *Hydrographic changes in the Labrador Sea*, 19602005. Prog. Oceanogr., 73, 242-276, doi:10.1016/j.pocean.2007.04.015.

Appendix A

Monthly Ocean Temperature Vertical Profiles

Appendix A shows the area averaged monthly vertical temperature profiles from Argo derived gridded Metoffice EN4 Data for the period 1993-2018 plotted in blue for all six respective regions. The black line shows the area averaged seasonal mean for vertical temperature profiles derived from the World Ocean Atlas 2018 (WOA18), which is the analyses of subsurface ocean variables at standard depths extending back to Climatological Atlas of the World Ocean (Levitus, 1982).

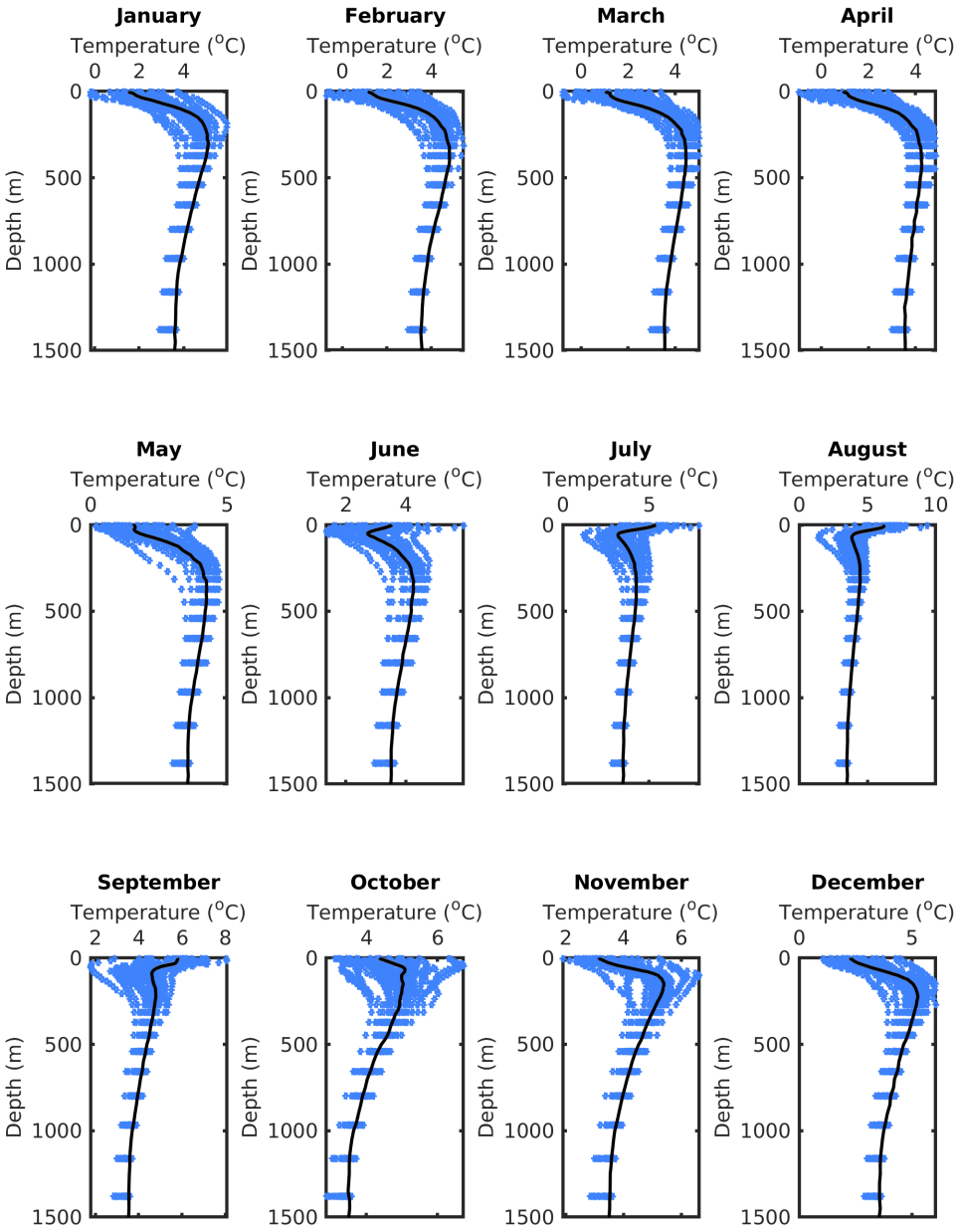

Figure A.1: Monthly Vertical Temperature Profile for Region 1

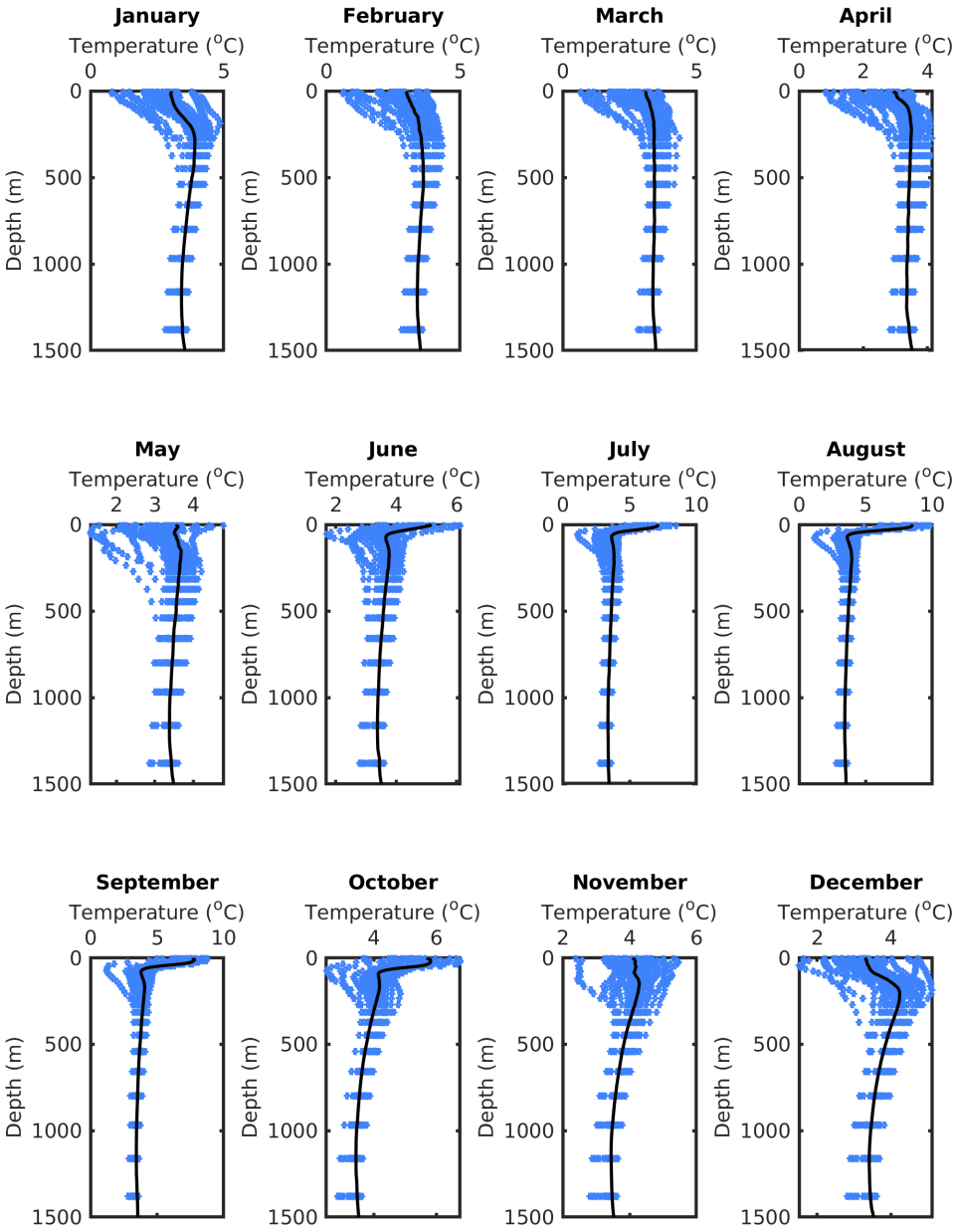

Figure A.2: Monthly Vertical Temperature Profile for Region 2

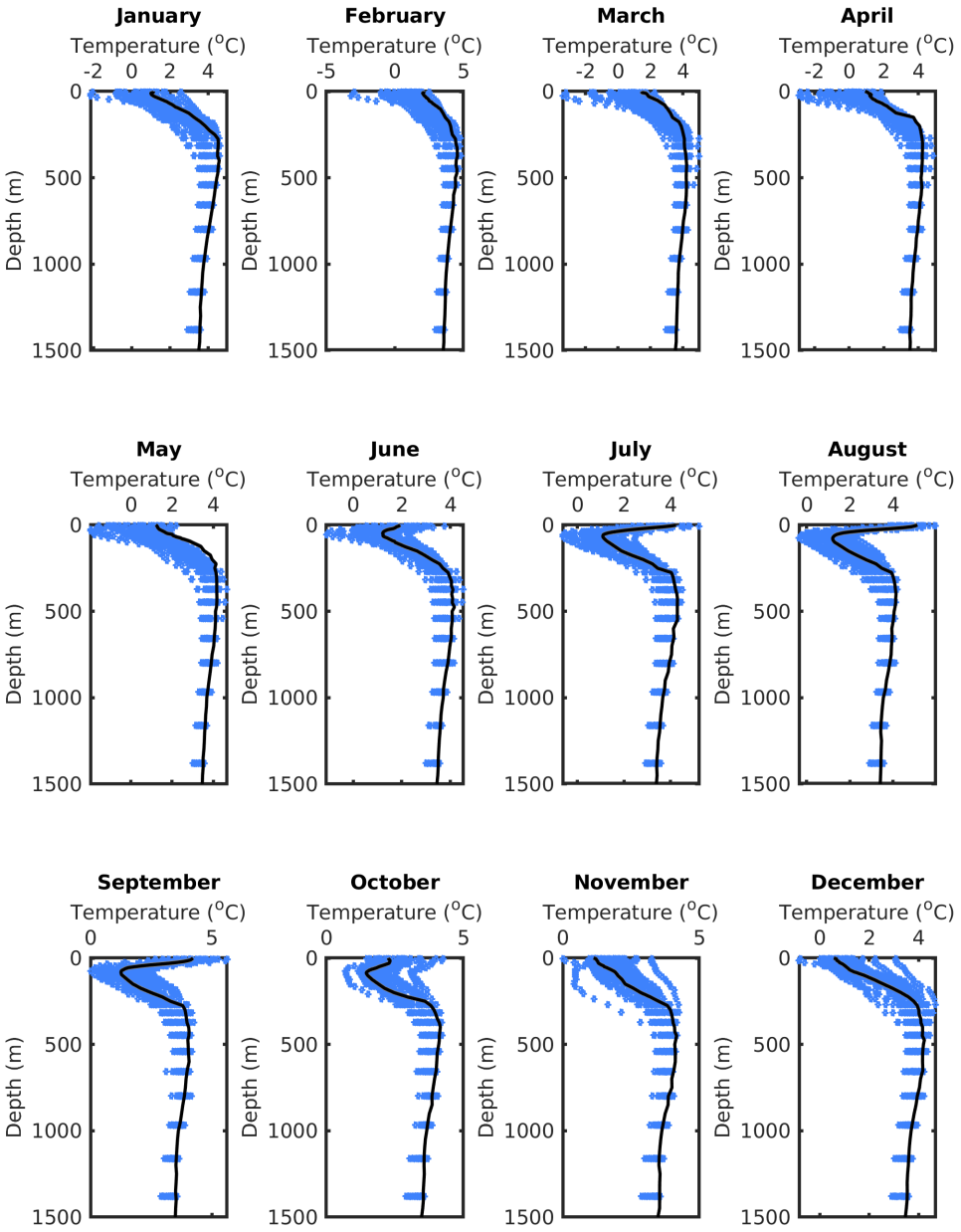

Figure A.3: Monthly Vertical Temperature Profile for Region 3

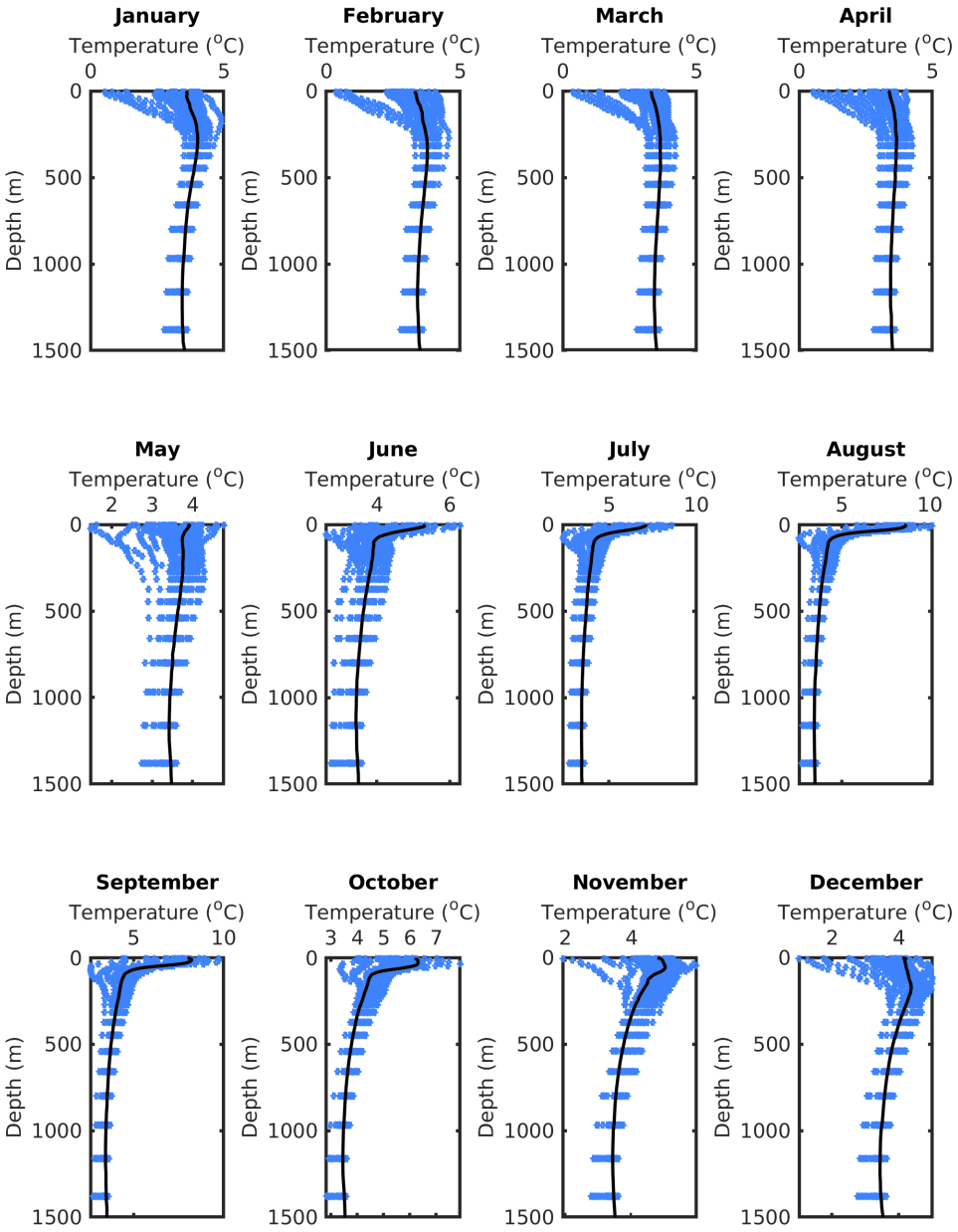

Figure A.4: Monthly Vertical Temperature Profile for Region 4

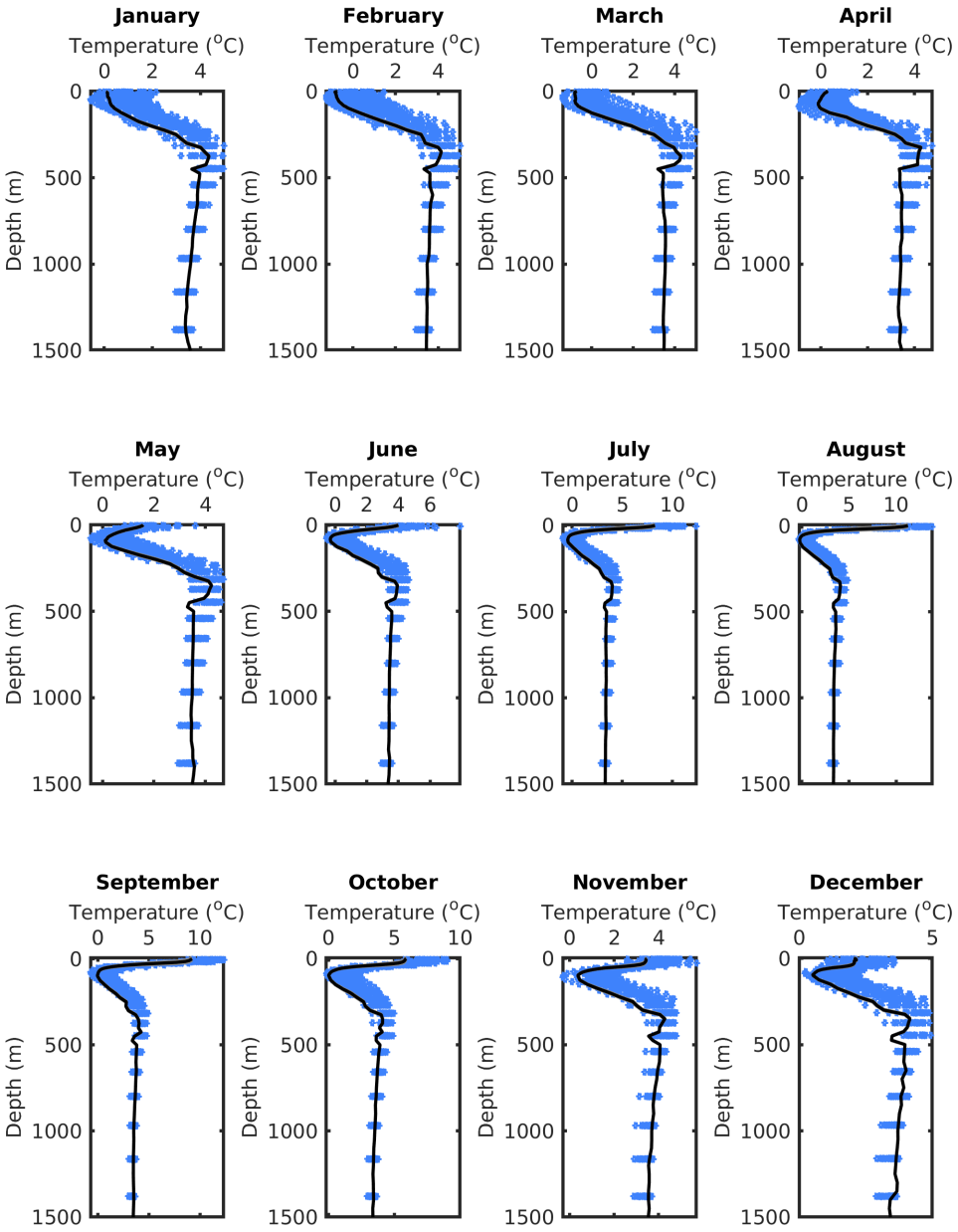

Figure A.5: Monthly Vertical Temperature Profile for Region 5

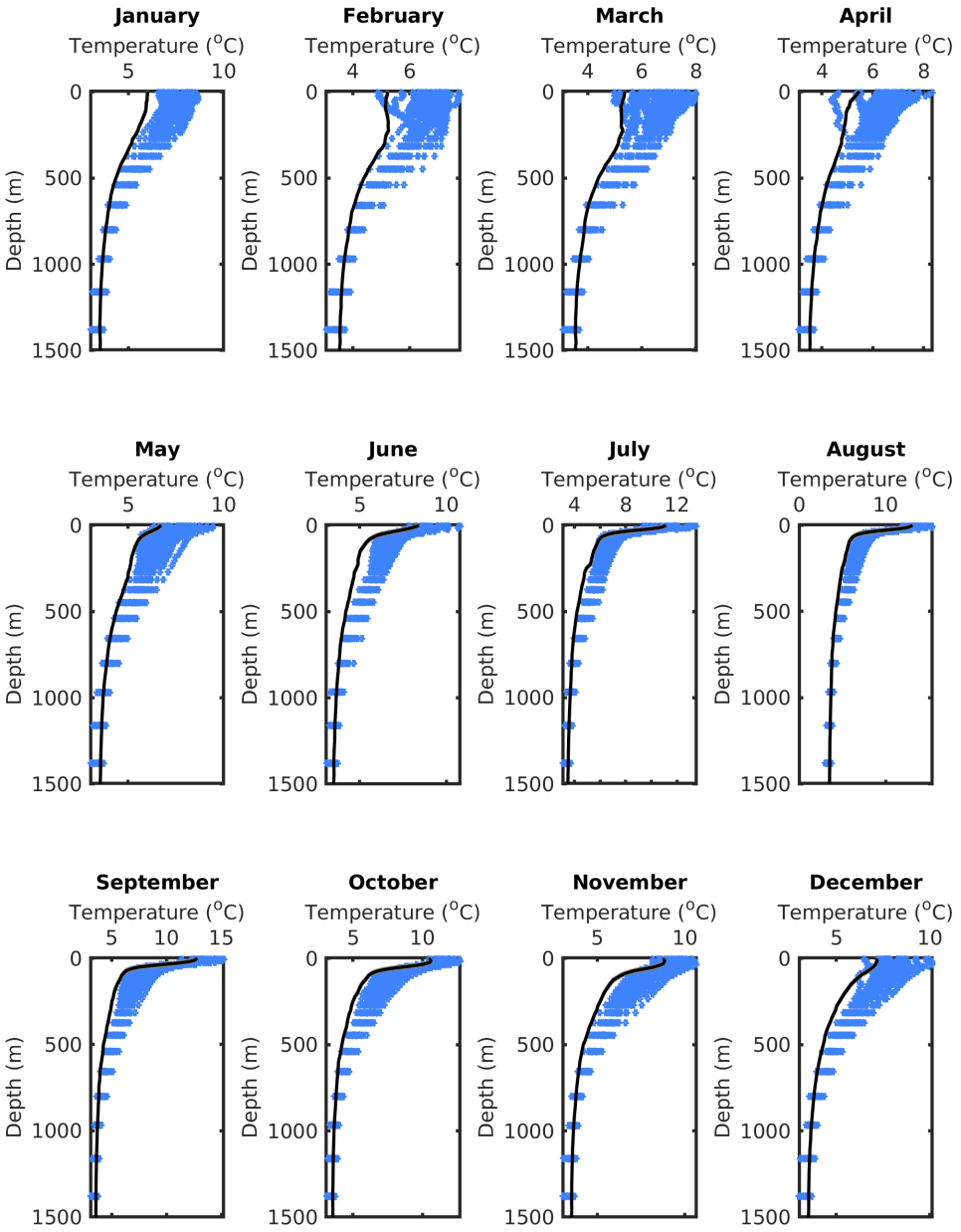

Figure A.6: Monthly Vertical Temperature Profile for Region 6

Appendix B

Cross-Correlations

B.1 Total Ocean Heat Transport Convergence

The monthly time-lag cross-correlation coefficients for ocean heat transport convergence between respective subregions for Total Ocean Column.

Figure B.1: Time-lag Total Ocean Heat Transport Convergence

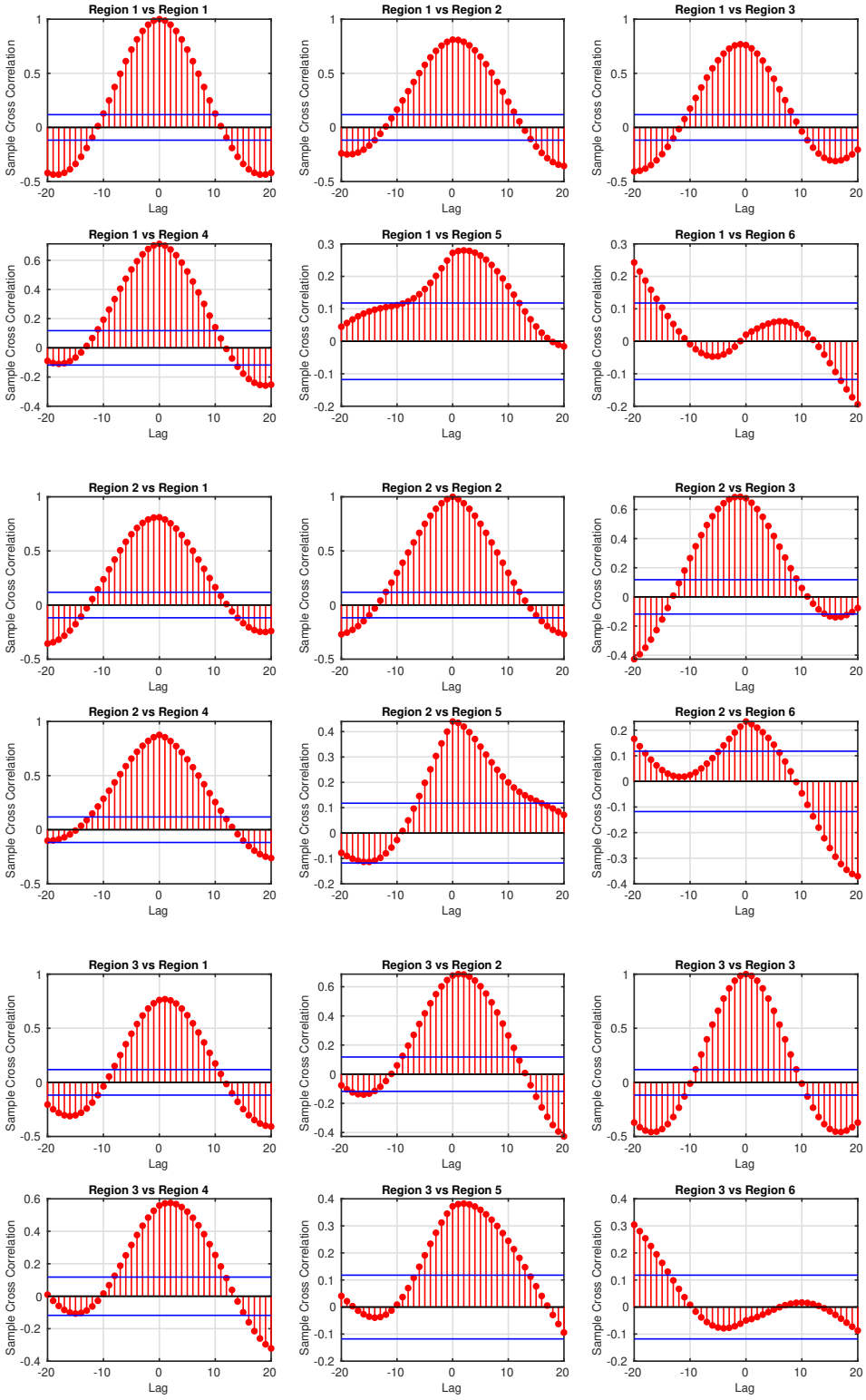

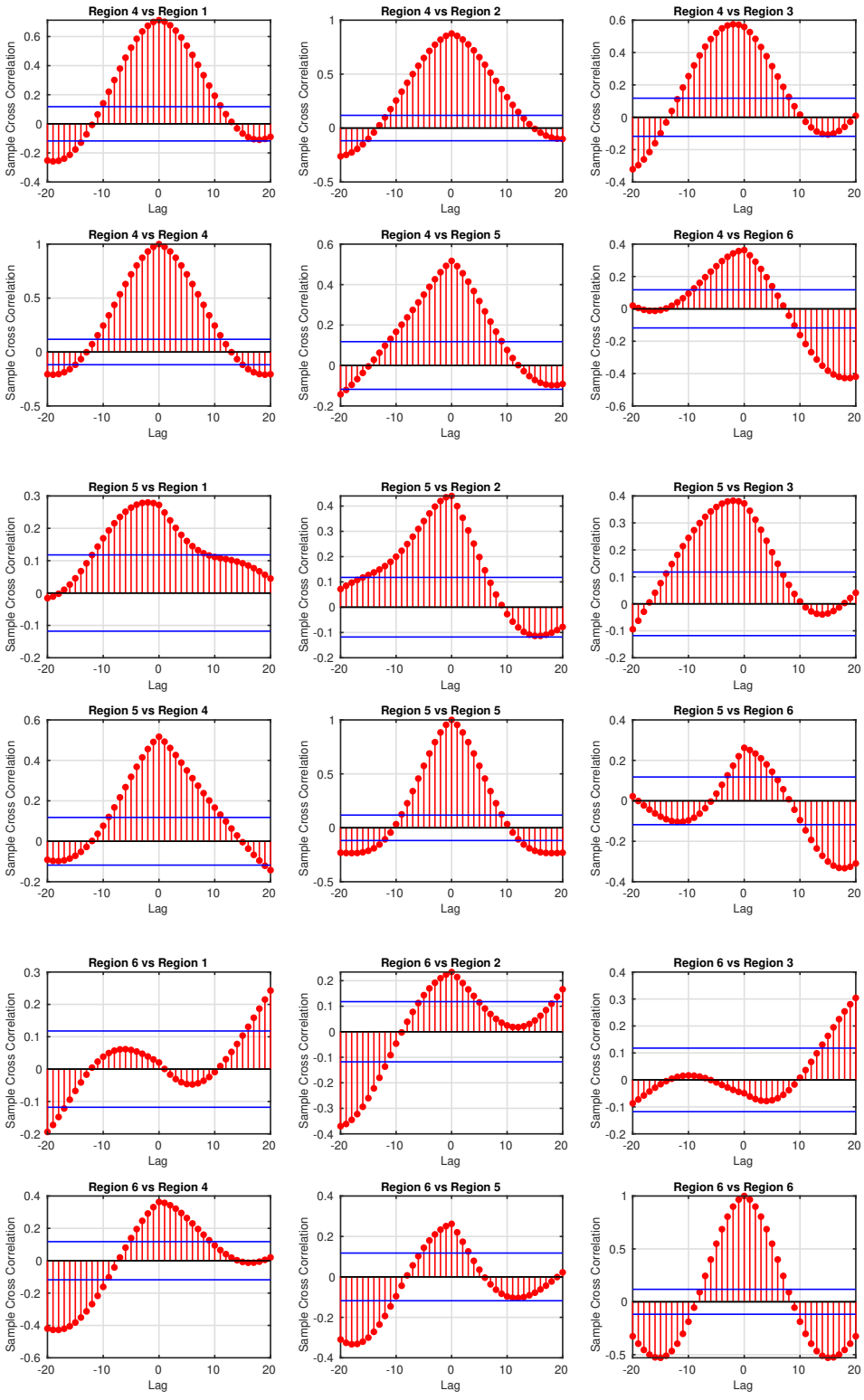
Region 4 vs Region 1
Region 4 vs Region 2
Region 4 vs Region 3
Region 4 vs Region 4
Region 4 vs Region 5
Region 4 vs Region 6
Region 5 vs Region 1
Region 5 vs Region 2
Region 5 vs Region 3
Region 5 vs Region 4
Region 5 vs Region 5
Region 5 vs Region 6
Region 6 vs Region 1
Region 6 vs Region 2
Region 6 vs Region 3
Region 6 vs Region 4
Region 6 vs Region 5
Region 6 vs Region 6
Sample Cross Correlation
Lag

B.2 Surface Ocean Heat Transport Convergence

The monthly time-lag cross-correlation coefficients for ocean heat transport convergence between respective subregions for the top 150 m surface layer.

Figure B.2: Time-lag Surface Ocean Heat Transport Convergence

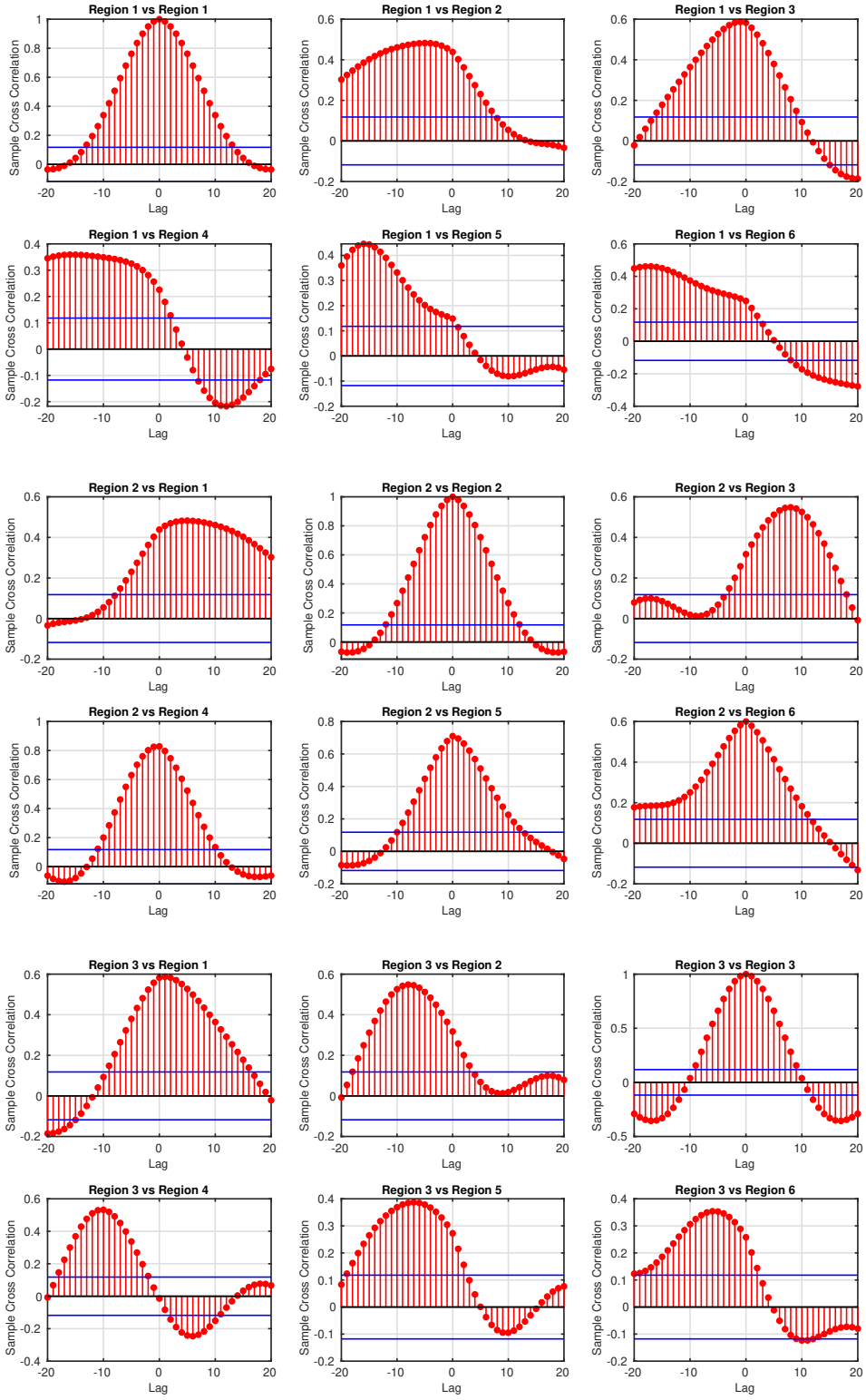

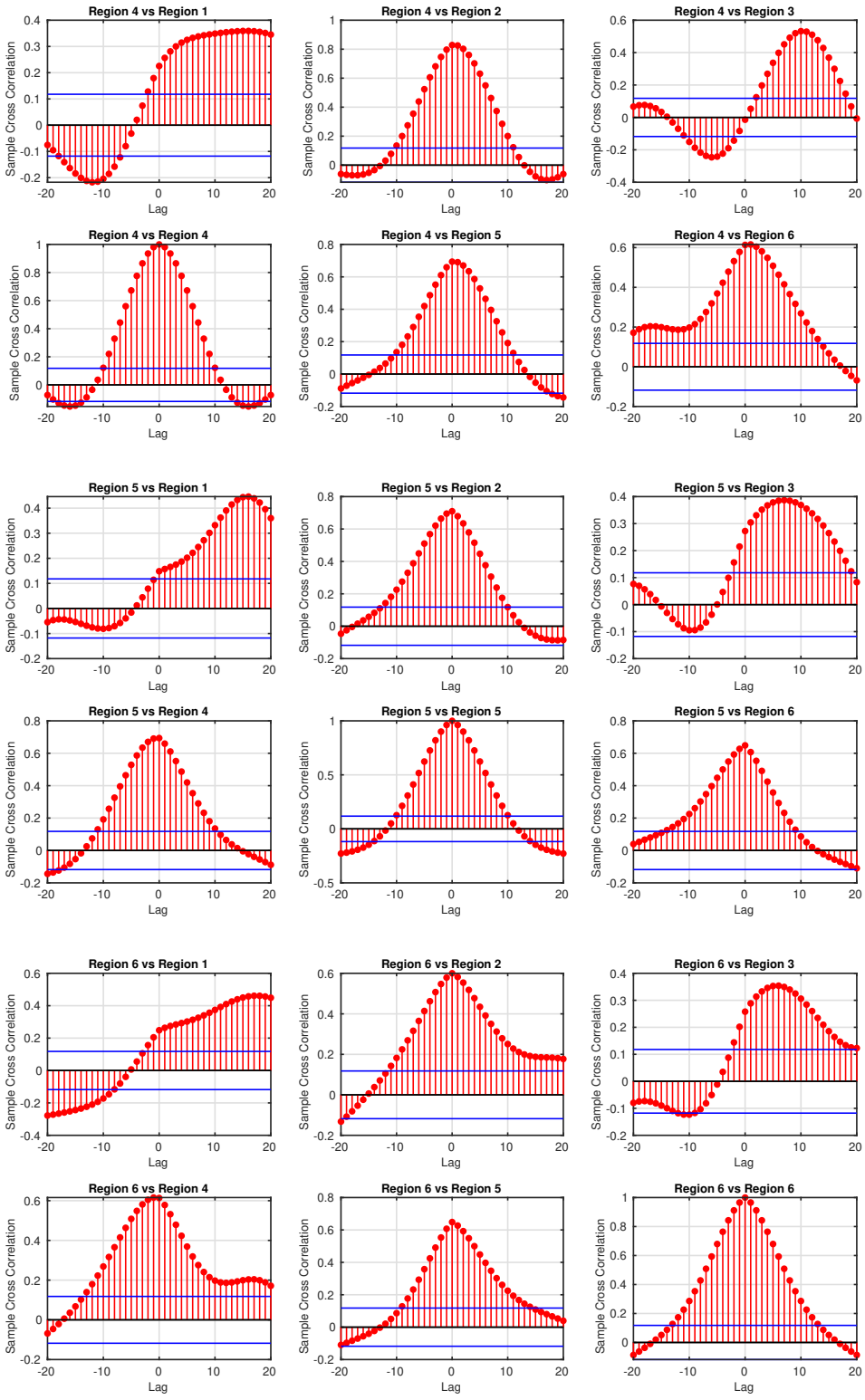
Region 4 vs Region 1
Region 4 vs Region 2
Region 4 vs Region 3
Region 4 vs Region 4
Region 4 vs Region 5
Region 4 vs Region 6
Region 5 vs Region 1
Region 5 vs Region 2
Region 5 vs Region 3
Region 5 vs Region 4
Region 5 vs Region 5
Region 5 vs Region 6
Region 6 vs Region 1
Region 6 vs Region 2
Region 6 vs Region 3
Region 6 vs Region 4
Region 6 vs Region 5
Region 6 vs Region 6
Sample Cross Correlation
Lag